

© 2016 by Bryan P. Dannowitz. All rights reserved.

NUCLEAR DEPENDENCE OF PROTON-INDUCED DRELL-YAN DIMUON  
PRODUCTION AT 120GEV AT SEAQUEST

BY

BRYAN P. DANNOWITZ

DISSERTATION

Submitted in partial fulfillment of the requirements  
for the degree of Doctor of Philosophy in Nuclear Physics  
in the Graduate College of the  
University of Illinois at Urbana-Champaign, 2016

Urbana, Illinois

Doctoral Committee:

Professor Jen-Chieh Peng, Chair  
Professor Naomi C. R. Makins, Director of Research  
Professor Michael Stone  
Professor Jim Eckstein

# Abstract

A measurement of the atomic mass dependence of Drell-Yan dimuons produced by 120GeV protons is presented here. Over 88,000 dimuon pairs with dimuon mass  $M \geq 4.2\text{ GeV}$  were recorded at SeaQuest from targets  $^1H$ ,  $^2H$ ,  $C$ ,  $Fe$ , and  $W$ . The ratio of dimuon yield per nucleon for heavy nuclei versus  $^2H$ ,  $R = Y_A/Y_{^2H}$ , is sensitive to modifications in the anti-quark sea in nuclei for the case of proton-induced Drell-Yan. No nuclear modifications are observed over the target quark momentum fraction range  $0.1 \leq x_t \leq 0.45$ . These results are compared to predictions of models of the EMC effect.

*Dedication here.*

# Acknowledgments

*Don't forget to acknowledge the NSF and mention the grant number!*

# Table of Contents

List of Tables . . . . .	viii
List of Figures . . . . .	ix
List of Abbreviations . . . . .	xi
List of Symbols . . . . .	xiii
Preface . . . . .	1
<b>Chapter 1 Theoretical Background . . . . .</b>	<b>2</b>
1.1 Introduction . . . . .	2
1.2 Di-lepton production in nucleon-nucleon collisions . . . . .	4
1.2.1 The Drell-Yan Process . . . . .	5
1.2.2 Drell-Yan Kinematics . . . . .	8
1.2.3 Cross-Section . . . . .	10
1.3 PDFs, Structure Functions, and the Quark Parton Model . . . . .	12
1.3.1 Drell-Yan Tests of the QPM . . . . .	16
1.4 QCD-Improved Drell-Yan . . . . .	17
1.5 Drell-Yan and Sea Quark Phenomenology . . . . .	17
1.5.1 $\bar{d}/\bar{u}$ Asymmetry . . . . .	17
1.5.2 The EMC Effect . . . . .	18
1.5.3 Models For the EMC Effect . . . . .	18
1.5.4 E-772 at Fermilab . . . . .	18
1.5.5 Nuclear Dependence of Drell-Yan at SeaQuest . . . . .	18
<b>Chapter 2 Apparatus . . . . .</b>	<b>21</b>
2.1 Apparatus Overview . . . . .	21
2.2 Main Injector Proton Beam . . . . .	22
2.3 Beam Intensity Monitor . . . . .	24
2.4 The SeaQuest Targets . . . . .	27
2.5 Focusing and Analyzing Magnets . . . . .	29
2.6 Beam Dump, Shields, and Absorbers . . . . .	31
2.7 Tracking Detectors . . . . .	31
2.7.1 Triggering Hodoscopes . . . . .	32
2.7.2 Drift Chambers . . . . .	33
2.7.3 Proportional Tubes . . . . .	36
2.7.4 Mass Resolution from Chamber Resolution . . . . .	37
2.8 Trigger . . . . .	39
2.8.1 Design Requirements . . . . .	39
2.8.2 Trigger Hardware . . . . .	40
2.8.3 Triggering Modes . . . . .	42

2.9	Data Acquisition Systems . . . . .	43
2.9.1	Main DAQ . . . . .	44
2.9.2	Scaler DAQ . . . . .	44
2.9.3	Beam DAQ . . . . .	45
2.9.4	Slow Control Readout . . . . .	45
<b>Chapter 3</b>	<b>Photomultiplier Tube Base Upgrade . . . . .</b>	<b>49</b>
3.1	PMT Basic Construction and Operation . . . . .	49
3.2	PMT Base Design Iterations . . . . .	51
3.2.1	Original Base . . . . .	54
3.2.2	Prototype Base v1 . . . . .	55
3.2.3	Prototype Base v2 . . . . .	57
3.2.4	Prototype Base v3 . . . . .	57
3.2.5	Prototype Base v4 . . . . .	57
3.3	PMT Base Comparisons . . . . .	58
3.3.1	Testing Apparatus, Measurements, and Procedure . . . . .	58
3.3.2	Original vs. Prototype v1 . . . . .	61
3.3.3	Original vs. Prototype v1 vs. Prototype v2 . . . . .	63
3.3.4	Prototype v1 vs. Prototype v3 . . . . .	64
3.3.5	Prototype v1 vs. Prototype v4 . . . . .	64
3.3.6	Base Comparison Conclusions . . . . .	65
3.4	Base Manufacturing and Installation . . . . .	65
<b>Chapter 4</b>	<b>Data Productions . . . . .</b>	<b>69</b>
4.1	Raw Data Processing . . . . .	69
4.1.1	CODA Event Format . . . . .	70
4.1.2	ROC Data Bank Formats . . . . .	71
4.1.3	Decoding Raw Data . . . . .	71
4.2	Online and Offline Processing . . . . .	73
4.3	RDBMS Data Structure . . . . .	74
4.3.1	Data Schemas . . . . .	75
4.3.2	Schema Table Organization . . . . .	75
4.3.3	Future Technologies . . . . .	75
4.4	Data Quality . . . . .	75
<b>Chapter 5</b>	<b>Analysis . . . . .</b>	<b>76</b>
5.1	Reconstruction and Tracking of SeaQuest Dimuons . . . . .	76
5.1.1	Hit Reduction . . . . .	76
5.1.2	Particle ID . . . . .	76
5.1.3	Muon Momentum Reconstruction . . . . .	76
5.1.4	Kalman Filter Track Fitting . . . . .	76
5.1.5	Vertex Fitting . . . . .	76
5.1.6	Monte Carlo Validation . . . . .	76
5.2	Data Selection . . . . .	76
5.3	Analysis Cuts . . . . .	76
5.3.1	Run Level Cuts . . . . .	76
5.3.2	Spill Level Cuts . . . . .	77
5.3.3	Event Level Cuts . . . . .	77
5.3.4	Dimuon Level Cuts . . . . .	77
5.3.5	Track Level Cuts . . . . .	77
5.4	Dimuon Yields . . . . .	77
5.4.1	Binning of Data . . . . .	77
5.4.2	Raw Yields . . . . .	78
5.4.3	Live Proton Calculation and Integration . . . . .	78

5.5	Dimuon Weights and Corrections . . . . .	78
5.5.1	“kEfficiency” Correction Using Messy/Clean Data . . . . .	79
5.5.2	The Naive Empty/None Correction . . . . .	84
5.5.3	The Empty/None vs. Intensity Curve . . . . .	85
5.5.4	Improved Background Correction . . . . .	85
5.6	Combinatorial Background Correction . . . . .	85
5.7	$ld_2$ Contamination Correction . . . . .	85
5.8	Isoscalar Corrections for $^{183}W$ and $^{56}Fe$ . . . . .	85
<b>Chapter 6</b>	<b>Results . . . . .</b>	<b>86</b>
6.1	Dimuon Yield Ratios . . . . .	86
<b>Chapter 7</b>	<b>Discussion . . . . .</b>	<b>87</b>
<b>Chapter 8</b>	<b>Conclusions . . . . .</b>	<b>88</b>
<b>Appendix A</b>	<b>Topic A . . . . .</b>	<b>89</b>
<b>Appendix B</b>	<b>Topic B . . . . .</b>	<b>90</b>
<b>References . . . . .</b>		<b>91</b>

# List of Tables

1.1	Kinematic variables relevant to the Drell-Yan process . . . . .	10
2.1	Characteristics of the seven SeaQuest target positions. The “Spills/Cycle” is only a typical configuration and can vary according to needs and running configurations. The non-zero interaction length of the empty flask is due to the $51\mu\text{m}$ -thick stainless steel end-caps of the flask and the $140\ \mu\text{m}$ -thick titanium windows of the vacuum vessel that contains it. . . . .	28
2.2	Parameters of all hodoscope planes. $z$ -positions of H2Y and H4 half-planes are offset slightly due to the half-planes themselves overlapping. . . . .	33
2.3	Parameters of all chambers. Those of primed planes are almost the same as of unprimed planes. The $z$ -positions of U and V planes are relative to those of X planes. . . . .	34
2.4	Combination of D1 and D3m chambers per data taking period. . . . .	34
2.5	Parameters of the four proportional tube planes. . . . .	37
2.6	Trigger settings for Run 3 and beyond. Prescale figures shown are typical values and were adjusted as experimental needs were tuned. NIM-1 and NIM-2 triggers’ exact conditions could be changed and reconfigured from the counting room. . . . .	42
5.1	$x_2$ bin ranges . . . . .	77
5.2	Raw dimuon yields for Roadset 57 . . . . .	77

# List of Figures

1.1	The octets and decuplet of Gell-Mann’s “Eightfold Way”. Top left: the eight particles of the meson octet; top right: the spin- $\frac{1}{2}$ baryon octet; bottom: the spin- $\frac{3}{2}$ baryon decuplet. . . . .	3
1.2	Dimuon mass spectrum from E-866 $p + h$ collisions at 800 GeV/c[21]. . . . .	5
1.3	The Drell-Yan process, an $s$ channel interaction consisting of the annihilation of a quark with an anti-quark. . . . .	6
1.4	A compilation of measurements of the running of the strong coupling constant, $\alpha_s(Q^2)$ [23]. .	7
1.5	(Left) classic electromagnetic screening of a free charge in a dielectric or even a vacuum. (Center) The analogous screening in the three-charge QCD regime. (Right) The color camouflaging due to the constant absorption/emission of colored gluons[30]. . . . .	8
1.6	A depiction of the Collins-Soper reference frame. The green plane along $\hat{h}$ is the plane shared by the two hadrons. . . . .	9
1.7	Parton distribution functions for quarks and gluons and their $x$ and $Q$ dependence as calculated to NNLO by the CTEQ-TEA (CT) global analysis group[14]. . . . .	14
1.8	The Drell-Yan process has a large range of higher-order QCD corrections that need to be accounted for. (a) and (b) are high order $q\bar{q}$ annihilations, and (c) and (d) are gluon “Compton scattering” terms. . . . .	17
1.9	E-772 Drell-Yan $\frac{A}{2H}$ ratios for several nuclear targets as a function of $x_2(x_t)$ [3]. . . . .	20
2.1	Perspective view of the SeaQuest spectrometer apparatus. . . . .	22
2.2	Spill structure of the beam delivered to SeaQuest. . . . .	23
2.3	Beam profile detailed by SWIC detectors along the NM beam line. . . . .	24
2.4	A single high-intensity event with majority of all detector elements firing off. White space within the rectangles indicates inactive elements whereas red, blue, and green represent elements which have fired during that event. Track reconstruction in these cases is impossible. .	25
2.5	The Beam Intensity Monitor (BIM) Čerenkov counter. Measurements are in inches. . . . .	26
2.6	The layout of the target table and its seven target positions, as seen from above. . . . .	28
2.7	Perspective drawing of FMAG’s aluminum coils embedded in an arrangement of iron slabs. .	30
2.8	Spectrometer layout of FMAG, KMAG, and Detector Stations 1-4. . . . .	32
2.9	Proportional tube top ( $x - z$ plane) view. . . . .	36
2.10	Proportional tube side ( $y - z$ plane) view. . . . .	36
2.11	A simplistic depiction of a track passing through from Station 1, through KMAG where its path is bent by the magnetic field, and then straight on through Stations 2 and 3. . . . .	38
2.12	The trigger system at SeaQuest is composed of 9 CAEN v1495 FPGA modules. These modules output a trigger signal to the Trigger Supervisor, which tells the DAQ when to record data. .	40
2.13	A block diagram of the major functions of the v1495 FPGA [32]. . . . .	41
2.14	A standard Beam DAQ display showing beam characteristics and spill data. The bottom two plots show the output of the QIE on a ms scale. . . . .	46
3.1	(Left) Histogram of hodoscope ‘hits’ in a typical event; (Right) Histogram of high-intensity event, with marked sagging most noticeably in the middle of the y-measuring hodoscopes . .	50

3.2	A diagram of typical PMT operation. The circuit controlling the voltage-dropping resistors is the part that was upgraded in this chapter. . . . .	50
3.3	MOSFET showing gate (G), body (B), source (S) and drain (D) terminals. The gate is separated from the body by an insulating layer (white) [28] . . . . .	52
3.4	Suggested voltage division schemes for gain vs. timing/linearity compromise [29]. . . . .	54
3.5	The original PMT base inherited from the ARGUS and HERMES experiments. . . . .	54
3.6	The voltage division between subsequent stages for the original PMT base design when supplied with -1500 V. . . . .	55
3.7	The Prototype v1 board circuit diagram received from Fermilab Particle Physics Division [20]. The parts are denoted as R: resistor, C: capacitor, Q: MOSFET transistor, D: Zener diode. .	56
3.8	The voltage devision between subsequent stages for the Prototypes v1, v2, and v3 PMT base designs when supplied with -1500 V. . . . .	56
3.9	The Prototype v3 board: 3 more transistorized stages than the Prototype v1 design. . . . .	57
3.10	The (negative) voltage between subsequent stages for the Prototype v4 PMT base. . . . .	58
3.11	Inside of the light box, with the prototype board (left) wired up to a Philips XP-2008 PMT (middle), facing a fast-pulsing LED source (right). . . . .	60
3.12	Measurements of the (a) signal amplitudes and (b) bleeder and signal currents in the original and prototype v1 PMT bases. The HV was inadvertently set to -1600V V for this test instead of the intended -1500 V. . . . .	62
3.13	Measurements of the (a) signal amplitudes and (b) bleeder and signal currents in the original, prototype v1, and prototype v2 PMT bases. . . . .	63
3.14	Measurements of the (a) signal amplitudes and (b) bleeder and signal currents in the prototype v1 and prototype v3 PMT bases. . . . .	64
3.15	Measurements of the (a) signal amplitudes and (b) bleeder and signal currents in the prototype v1 and prototype v4 PMT bases. . . . .	65
3.16	(Left) The components of the disassembled original base and the manufactured new base PCB with attached daughter board. (Right) The original and new bases fully assembled, side-by-side. .	66
3.17	The $\gamma$ -decay energy spectrum of Cs-137 as seen through a scintillator-PMT-qVt setup [35]. Here, the Compton edge can be seen at channel 110. . . . .	68
4.1	(Left) The Prestart event, with event type 17; (Right) The Go event, with event type 18[33].	70
4.2	(Left) A standard physics event, with various event types, filled with a series of data banks; (Right) The ROC data bank format[33]. . . . .	71
5.1	The linear tendency of detector multiplicity to increase with intensity is observed by looking to unbiased NIM3 events. Here, the occupancy per event of the drift chambers at station 2 are shown as a function of intensity. . . . .	80
5.2	The ratio of “messy” to “clean” dimuon samples from the Deuterium target in Roadset 67 data. This shows the linear relationship of the tracking efficiency to the intensity of the events. The shaded band indicates the 95% confidence band of the fit. . . . .	81
5.3	Tracking efficiency with the data broken into three statistically equivalent bins in the five primary kinematics, $(x_1, x_2, \theta_\mu, \phi_\mu, p_T)$ . There appears to be a significant kinematic dependence on $x_1$ and $x_2$ . . . . .	82
5.4	The kinematics $x_F$ and $M_{\gamma^*}$ are investigated. A clear kinematic dependence exists in $x_F$ while $M_{\gamma^*}$ is largely consistent. . . . .	83
5.5	Comparing the tracking efficiency curves across (left) the five targets and (right) two temporally different subsets (different roadsets) of data. Confidence bands removed from the target plot for the sake of clarity. . . . .	84

# List of Abbreviations

ACNET	Accelerator control system network
AD	Accelerator division (of Fermilab)
BIM	Beam intensity monitor
BNC	Bayonet NeillConcelman signal cable connector standard
BOS	Beginning of spill
BPM	Beam profile monitor
CEBAF	Continuous Electron Beam Accelerator Facility
CODA	CEBAF On-line Data Acquisition
CS	Collins-Soper reference frame
CTEQ	Coordinated theoretical-experimental project on QCD
DAQ	Data acquisition
DC	Drift chamber
DIS	Deep-inelastic scattering
DY	Drell-Yan
E906	Experiment number 906 at Fermilab National Accelerator Laboratory, a.k.a. SeaQuest
EOS	End of spill
EOF	End of file
EPICS	Experimental physics and industrial control system
EVIO	CODA event input/output
FEE	Front-end electronics
FNAL	Fermi National Accelerator Laboratory (Fermilab)
FPGA	Field programmable gate arrays
IC	Ion chamber
KTeV	Fermilab experiment that previously inhabited the NM4 experimental hall
LED	Light-emitting diode

LINAC	Fermilab Linear Accelerator
LO	Leading order
MI	(Fermilab) Main Injector
MOSFET	Metaloxidesemiconductor field-effect transistor
NDF	Neutral density filter
NLO	Next-to-leading order
NM	Neutrino-muon beam line
NNLO	Next-to-next-to-leading order
PCB	Printed circuit board
PDF	Parton distribution function
PID	Particle identification
PMT	Photomultiplier tube
RF	Radio frequency
RFQ	Radio frequency quadrupole
ROC	Readout controller
SEM	Secondary emission monitor
SHV	Secure high voltage connector standard
TS	Trigger supervisor
QCD	Quantum chromodynamics
QED	Quantum electrodynamics
QIE	Charge (Q) integrator and encoder
RDBMS	Relational database management system
SQL	Structured querying language
SWIC	Segmented wire ion chamber
VME	Versa Module Europa

# List of Symbols

$\mu^+$	Positive muon
$\mu^-$	Negative muon
$J/\Psi$	The ground state of the <i>charm-anticharm</i> meson family
$\Psi'$	The first excited state of the <i>charm-anticharm</i> meson family

# Preface

*Preface here talking about what is contained in this thesis. Emphasize that the thesis contains the summary of my personal efforts on the SeaQuest experiment, and describe the layout of the paper. Mention that the Apparatus, PMT, and DB sections are standalone chapters that are not required in order to understand the rest of the chapters.*

# Chapter 1

## Theoretical Background

*CHAPTER STATUS: IN PROGRESS*

The topic of this paper is the exploration of the sub-structure of the *nucleon*, a particle that makes up an atom's nucleus which can be either a proton ( $p$ ) or a neutron ( $n$ ). By sub-structure, I refer to the nucleon's composition and the momentum distributions carried by the nucleon's constituent particles, quarks and gluons.

While a complete review of the history and physics behind nucleon structure and its investigative probes is beyond the scope of this paper, a brief overview of Drell-Yan, parton distribution functions, and nuclear structure phenomenology will help in understanding concepts and terminology relevant to this and later chapters.

### 1.1 Introduction

The first indication that the proton may have some internal structure was in a 1933 experiment by Estermann *et al.* measuring the magnetic moment of the proton [15]. Since the proton was thought to be a point-like Dirac particle, it's magnetic moment ( $\mu_p$ ) was expected to be  $\mu_p = \frac{e}{2m_p} = 1\text{n.m.}$ , or one *nuclear magneton*. The experiment resulted in a value of 2.5 n.m., leading many to reconsider the notion that the proton is indeed point-like.

Around the same time, Hideki Yukawa is credited for establishing the first theory of a *strong force*, a force binding together nucleons in a nuclei against the sizable *Coulomb* repulsion of protons against each other. The force was theorized to be mediated by the exchange of particles called *mesons*, and its range was limited to nuclei-scale distances, seeing as it's not observed at larger distances. Based upon the size of the nucleus, Yukawa estimated the mass of the intermediating particles to be approximately  $2 \times 10^2 m_e \approx 100\text{MeV}$ , where  $m_e$  is the electron mass. The following year, Anderson *et al.* discovered the muon ( $\mu$ ) at around this mass<sup>[citation needed]</sup>, which confused many as it did not seem to partake in strong interactions. Eventually, by 1947, the meson theory was validated by the discovery of the *pion* by Powell *et al.*<sup>[citation needed]</sup>, and

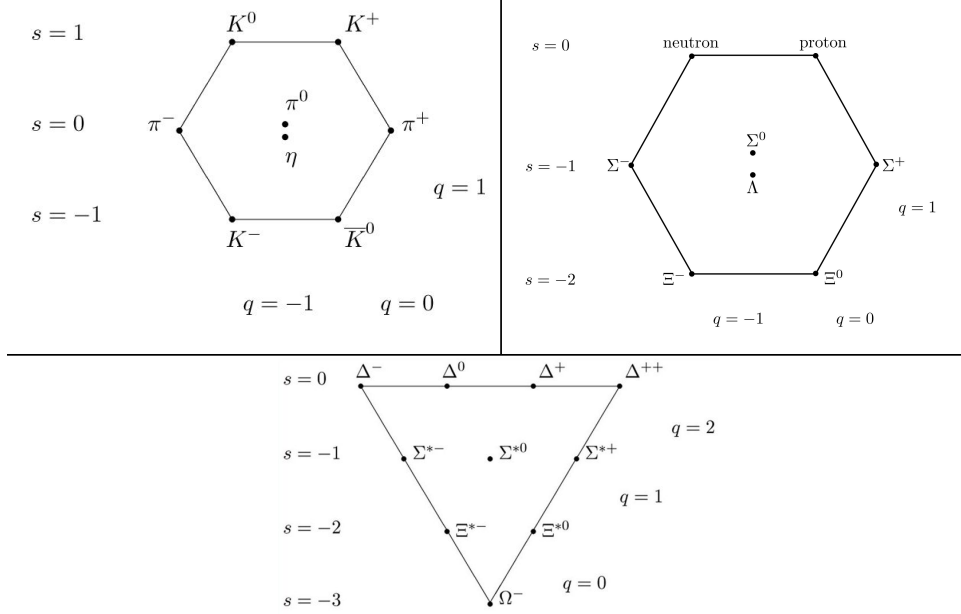


Figure 1.1: The octets and decuplet of Gell-Mann’s “Eightfold Way”. Top left: the eight particles of the meson octet; top right: the spin- $\frac{1}{2}$  baryon octet; bottom: the spin- $\frac{3}{2}$  baryon decuplet.

Yukawa was awarded a Nobel Prize for his theory in 1949. While the pion turned out to be just another composite particle, its discovery was a watershed moment in particle physics that led to a cascading series of discoveries.

Near the end of the 1960’s, SLAC began the first set of experiments to use an electron beam to investigate the nucleon in what is now known as Deep Inelastic Scattering (DIS). What they discovered was that the functions used to describe nuclear structure were largely independent of momentum transfer ( $Q^2$ ) above a certain threshold. This so-called “scaling” behavior lent credence to the theory that nucleons were composed of a point-like particles. This discovery coupled with the proliferation of new particles (the “particle zoo”) led Murray Gell-Mann and Yuval Ne’eman to construct a framework that would make some sense of it all. Gell-Mann had organized the host of mesons and baryons discovered into a geometric order named the “Eightfold Way”<sup>1</sup> as depicted in Figure 1.1. The underlying explanation for all of this, as described independently by Gell-Man and Ne’eman, was to characterize these many particles as the several combinations of three *flavors* of constituent particles, named *quarks*. The flavors, *u*, *d*, and *s* were named *up*, *down*, and *strange*. Here, mesons were predicted to be composite particles of integer spin containing two quarks and baryons be half-integer spin particles composed of three quarks. This model led Gell-Mann to predict the existence of the  $\Omega^-$  particle, along with its *strangeness*, charge, and mass. The discovery of this particle[7] earned Gell-Mann the 1969 Nobel Prize for his work on the quark model.

<sup>1</sup>Gell-Mann here makes a rather poetic allusion to the Buddhist “Noble Eightfold Path”

Though this model was a breakthrough in the understanding of fundamental particles, it did not comprehensively describe all experimental data. For example, when accounting for the total momentum of a nucleon, it was found that only  $\sim 50\%$  of the momentum was being carried by the quarks. It was not until the theory of quantum chromodynamics (QCD) came along that this and several other mysteries could be explained. QCD described the mechanism of a 3-fold *color* charge and the gauge bosons, gluons, that intermediate the strong force between quarks (and other gluons). In the particular case of the missing momentum, this was found to reside in the intermediating gluons[6], which carry only color charge, to which the electro-weak probes used were insensitive.

Many nuclear probes and methods have been used to characterize the distributions and characteristics of nuclear partons, including the aforementioned DIS process. As I will describe later in this section, much has been learned about parton probability distribution functions with this and other processes, but it is the process of hadron-hadron di-lepton production that is of primary focus in this paper, which allows for an alternative approach to investigate the structure and characteristics of the quarks inside of a nucleon, and perhaps shed some light on some ongoing mysteries in nuclear physics.

## 1.2 Di-lepton production in nucleon-nucleon collisions

Studying the production of pairs of leptons resulting from hadron-hadron collisions has proven to be a powerful tool in probing nucleon structure and parton distribution functions (PDFs). Figure 1.2 shows the mass spectrum of the muon mode of di-lepton production in proton-nucleus collisions measured at the E-866/NuSea experiment at Fermilab[21]. The resonances of the  $J/\Psi$ ,  $\Psi'$ ,  $\Upsilon$ ,  $\Upsilon'$ , and  $\Upsilon''$  can be seen atop a smooth, continuous distribution which decreases with mass. The process responsible with this distribution of  $\mu^+\mu^-$  pairs is the Drell-Yan process[13], which is illustrated in the Feynman diagram in Fig. 1.3. This process is characterized by a quark annihilating with an anti-quark to form a virtual time-like photon which then decays into a pair of leptons. The study of this process can lend some insight into nucleon structure due to the fact that the mass and momentum of the di-lepton pair directly reflects the momentum distributions of the interacting quarks and anti-quarks. Current knowledge and models<sup>[citation needed]</sup> of these momentum distributions come primarily from deep-inelastic lepton scattering (DIS) and the Drell-Yan (DY) process.

One particular focus of study for the Drell-Yan process is its nucleon number-dependent ( $A$ -dependent) behavior of its cross sections. This is of particular interest due to a phenomenon known as the EMC effect, in which the European Muon Collaboration (EMC) discovered in 1983 that parton distribution functions become modified when in the presence of the nuclear medium. This  $A$ -dependent behavior was not expected

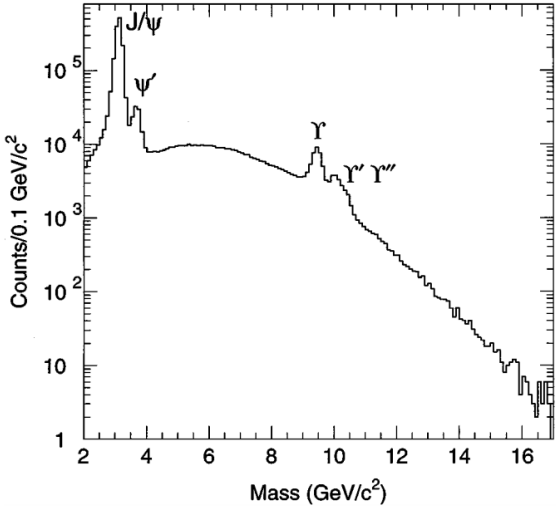


Figure 1.2: Dimuon mass spectrum from E-866  $p + h$  collisions at 800 GeV/c[21].

for hard scattering processes as the modest (maximum 8.8 MeV) binding energy of a nucleus on a nucleon was not thought to have a significant effect on quark momentum distributions within a nucleon ( $938\text{ Mev}/c^2$ ). Many experiments since [citation needed] have confirmed, extended, and precisely characterized the A-dependent behavior observed. Among the many hard scattering probes for investigating this phenomenon, the Drell-Yan process is uniquely capable of isolating the effect on the anti-quark distributions to a high degree of accuracy. The study of the effects of the nuclear medium on nucleon anti-quark distributions is the secondary research goal of the SeaQuest experiment and is the main focus of this thesis.

Within this thesis, the Drell-Yan process and its properties are discussed in *sections so and so* and various A-dependent behaviors seen in Drell-Yan and DIS are discussed in *sections so and so*. A few models are discussed in an attempt to theoretically characterize this A-dependent behavior in *sections so and so*.

In cases where a Drell-Yan process occurs, it can often be the case that the incident quark must pass through the strongly-interacting nuclear medium prior to its annihilation with the anti-quark in the target. By investigating the momentum distribution of the quark from the beam and its A-dependence, some insight can be gained regarding the parton energy loss as it moves through a foreign nuclear medium. This topic and its existing data are briefly discussed in *section so and so*.

### 1.2.1 The Drell-Yan Process

The study of continuum di-lepton production in hadron collisions,

$$h_A + h_B \rightarrow l^+l^- + X \quad (1.1)$$

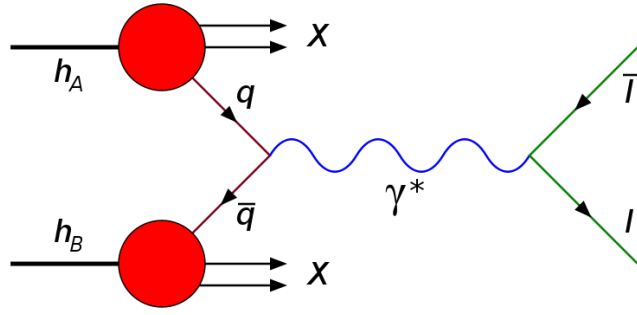


Figure 1.3: The Drell-Yan process, an  $s$  channel interaction consisting of the annihilation of a quark with an anti-quark.

can be used to study hadronic structure in a way that is complementary to the study of deep-inelastic scattering,

$$l + h \rightarrow l' + X. \quad (1.2)$$

In 1970, S. Drell and T.M. Yan were the first to suggest that, at high  $Q^2 (= M_{l+l-}^2) \geq 16\text{GeV}^2$ , the quarks inside the hadrons  $h_A$  and  $h_B$  can be considered free fermions in the instantaneous moment that they interact. The Drell-Yan model addresses the dominant subprocess here,

$$q_A + \bar{q}_B \rightarrow \gamma^* \rightarrow l^+ l^- \quad (1.3)$$

as an electromagnetic annihilation process. In this high- $Q^2$  kinematic space, the final state of the hadrons that contain these quarks becomes irrelevant. By the energy-time uncertainty principle [citation needed] of  $\Delta E \Delta t \sim \hbar$ , the timescales under consideration are  $< 10^{-25}\text{s}$ , and the corresponding distances are  $< 10^{-17}\text{m}$ , where the size of a nucleon is  $\sim 10^{-15}\text{m}$  [citation needed]. At these short space-time scales, electromagnetic annihilation dominates this quark-quark interaction.

This is further reinforced by the widely accepted non-Abelian gauge field theory of Quantum Chromodynamics (QCD) which describes the interactions between quarks and gluons. QCD provides a theoretical justification for treating Drell-Yan processes as events isolated from the rest of the hadron states, and it does so through the concept of the running of the coupling constant, or *asymptotic freedom* [8]. This characteristic feature of QCD is described by the decrease of the strength of the strong force coupling constant as the space-time scale of the interaction approaches zero (i.e. as  $Q^2 \rightarrow \infty$ ). The strong coupling constant can be

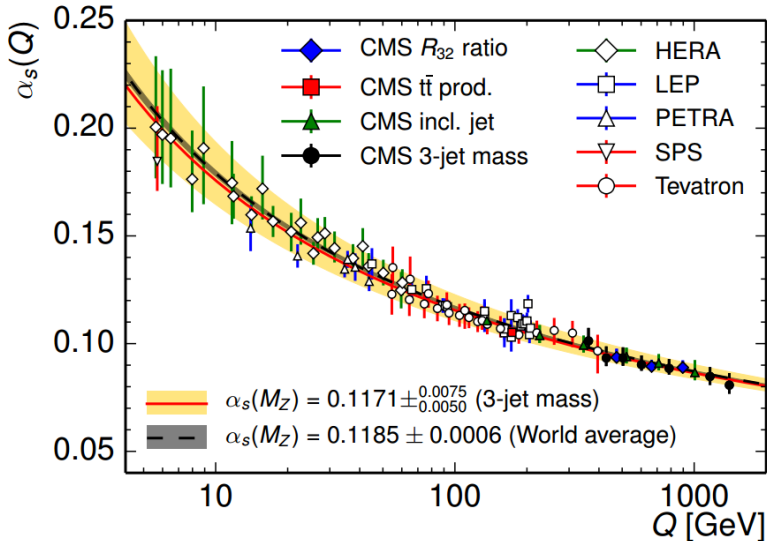


Figure 1.4: A compilation of measurements of the running of the strong coupling constant,  $\alpha_s(Q^2)$ [23].

expressed as a function of  $Q^2$ :

$$\alpha_s(Q^2) = \frac{1}{\beta_0 \ln(Q^2/\Lambda^2)} \quad (1.4)$$

where

$$\beta_0 = \frac{12\pi}{33 - n_f} \quad (1.5)$$

Here,  $\Lambda$  is the QCD scale parameter that depends on the number of quark flavors,  $n_f$ , and the renormalization scheme, measured to be around  $\sim 217$  MeV. Experimental measurements of the running of the coupling constant as measured by many different processes can be seen in Figure 1.4.

It is useful to have some intuition as to the reason for these “running” of the coupling constants. The phenomena responsible are termed “screening” and “anti-screening” (or “camouflaging”)[30]. This is straightforward in the case of the electromagnetic force which can be seen depicted in the left pane of Figure 1.5. Whether it is in some kind of dielectric medium or in an isolated vacuum (where quantum fluctuations lead to virtual  $e^+e^-$  pairs), the charges surrounding an individual charged particle are oriented in such a way as to decrease the overall observed charge. In the realm of QED, the higher energies you use to probe a particle, the closer you actually get to seeing the “actual” charge of the particle, and as such, the EM coupling constant increases at higher energies.

The same is seen in the case of QCD with its non-binary charge scheme. It’s more difficult to conceptualize, but the same screening effect exists in the case of a particle with color charge. The middle pane of Fig. 1.5 is a depiction of screening analogous to the familiar EM screening. The difference between QCD and

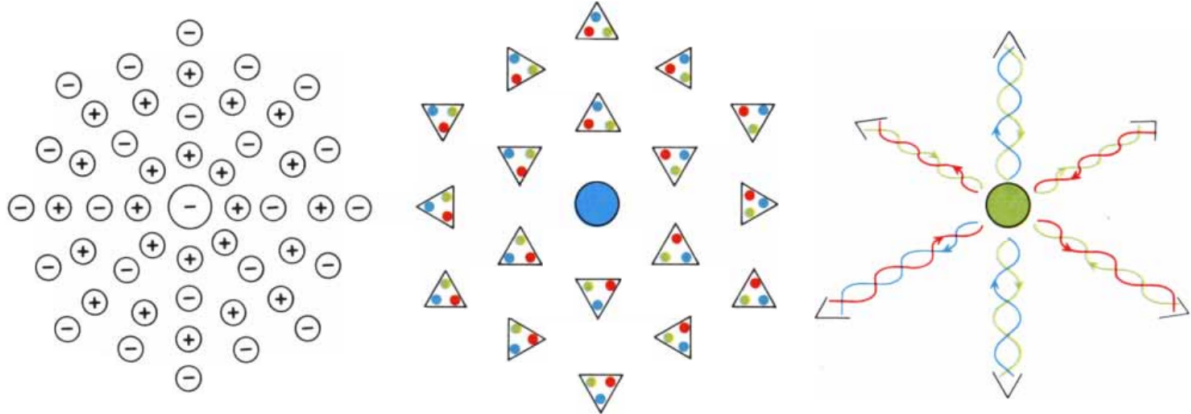


Figure 1.5: (Left) classic electromagnetic screening of a free charge in a dielectric or even a vacuum. (Center) The analogous screening in the three-charge QCD regime. (Right) The color camouflaging due to the constant absorption/emission of colored gluons[30].

QED with the behavior of the coupling constants is attributable to the fact that the force-carrying boson of QCD, the gluon, carries with it its own color charge. In the QED picture, the charge at the center is continuously emitting and absorbing photons as it interacts with the surrounding charges, but its charge does not change. With the color-charged particle, gluons are also being continuously emitted and absorbed, but an effect of that is a change in color charge. The result ends up being the phenomenon of camouflaging where, the closer you are to a color-charged particle, the less that you can “see” the *net* charge, and the actual charge of the particle is obfuscated. The net charge of the particle, statistically, becomes neutral, causing the strong force to become increasingly feeble at smaller scales (compared to the strength of QED interactions). This effect competes with and surpasses the color screening that occurs and is the root cause of the asymptotic freedom in QCD. On the flip side, the farther you get from the color charge, the more you are exposed to the full true net charge, and the stronger the coupling becomes. This increase in the coupling is the QCD confinement that is observed. An example if in the right pane of Fig. 1.5 where the quark emits many gluons, thus changing its color from Blue to Green, but when summing over all colors emitted and absorbed, the net color is still Blue.

### 1.2.2 Drell-Yan Kinematics

In the center-of-mass frame, the Drell-Yan process can be broken down into three stages with three sets of kinematics (refer to Fig. 1.3). Beginning with the quarks,  $x$  is defined as the fraction of the hadron’s momentum carried by the interacting quark or antiquark. Conventionally in fixed-target experiments, subscripts are assigned as  $x_1$  and  $x_2$ , which refer to the quark/antiquark from the beam and the antiquark/quark from

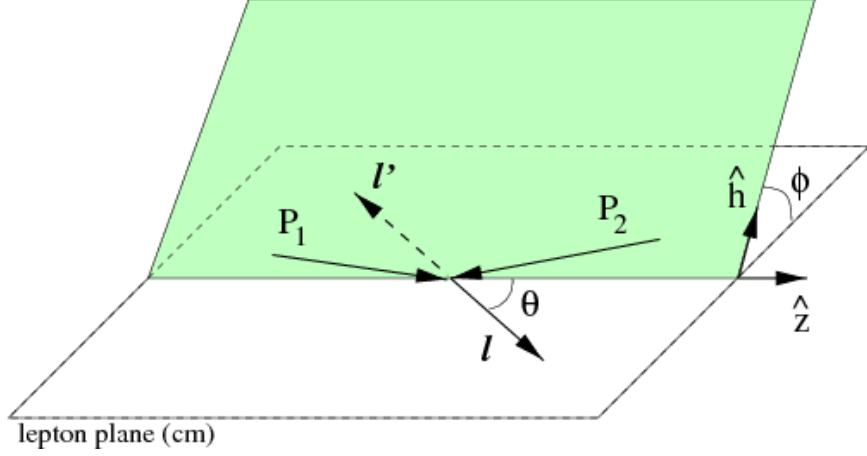


Figure 1.6: A depiction of the Collins-Soper reference frame. The green plane along  $\hat{h}$  is the plane shared by the two hadrons.

the target, respectively. This  $x$  is called the Bjorken  $x$ , and is well-known in DIS processes to have a value of

$$x = -q^2 / 2p \cdot q \quad (1.6)$$

where  $p$  and  $q$  are the 4-momenta of the hadron and the photon. In DY, the same momentum fraction  $x$  is used to describe part of the fundamental basis of the interaction. In this case,  $q$  is the 4-momentum of the virtual photon and  $p$  is the 4-momentum of the hadron that contains the quark in question.

The next stage of the process is the virtual photon. This photon's properties are effectively equivalent to the 'dimuon' or 'dilepton', which are the terms more commonly used in referring to kinematics. The first of its relevant kinematics is its mass  $M_{\gamma^*}$ , which represents its energy and virtuality. The value  $x_F$ , or Feynman-x, is the fraction of the maximum possible longitudinal momentum carried by the virtual photon in the beam direction. The transverse momentum,  $p_T$ , and the azimuthal production angle,  $\phi_{\gamma^*}$  are the remaining kinematics associated with the virtual photon.

The third stage regards the pair of leptons produced. In the frame of the virtual photon, there is a polar and azimuthal decay angle,  $\theta_\mu$  and  $\phi_\mu$ , respectively, for each of the decay muons. It becomes impossible, however, to reconstruct these variables, as the individual transverse momenta of the quarks are unknown, and thus the quark-antiquark annihilation axis is unknown. This is remedied by shifting the process into the Collins-Soper (CS) reference frame[10] which orients the reference axis to be parallel to the bisector of the angle between the interacting hadrons in the rest frame of the muon pair. A depiction of the Collins-Soper frame can be found in Fig. 1.6. In total, this brings a total of eight kinematic variables, summarized in Table 1.1.

Experimentally, six independent variables are measured, which form a basis by which all eight can be known. This is due to the fact that two pairs of variables,  $(M_{\gamma^*}, x_F)$  and  $(x_1, x_2)$  are correlated by the following, ignoring quark masses and considering  $p_\perp \ll p_\ell$ :

$$x_F \equiv \frac{p_\ell}{\sqrt{s}/2} \approx x_1 - x_2 \quad (1.7)$$

$$M_{\gamma^*}^2 \equiv E^2 - p_\ell^2 = s x_1 x_2 \quad (1.8)$$

$$E = \frac{1}{2}(x_1 + x_2)\sqrt{s} \quad (1.9)$$

$$p_\ell = \frac{1}{2}(x_1 - x_2)\sqrt{s} \quad (1.10)$$

In this frame, the longitudinal momenta of the quarks are  $x_1\sqrt{s}/2$  and  $-x_2\sqrt{s}/2$ , with  $\sqrt{s}$  being the center of mass energy of the hadronic collision. So, by measuring the 3-momenta of the  $\mu^+$  and  $\mu^-$ , the quantities  $(M_{\gamma^*}, x_F, p_T, \phi_{\gamma^*}, \theta_\mu, \phi_\mu)$ , which is sufficient to calculate the remaining  $(x_1, x_2)$  in our approximation.

Variable	Description
$x_{1/2}$	Momentum fraction of the beam/target quark
$M_{\gamma^*}$	Mass of the virtual photon (dimuon)
$x_F$	Fraction of the max. possible $p_\ell$ carried by virt. photon
$p_T$	Transverse momentum carried by the virt. photon
$\theta_\mu, \phi_\mu$	Polar and azimuthal decay angle of one of the muons, in the CS ref. frame
$\alpha$	The fine structure constant
$K(x_1, x_2)$	High-order QCD correction term
$\sqrt{s}$	Center of mass energy of the hadronic collision
$\sqrt{\hat{s}}$	Center of mass energy of the $q\bar{q}$ collision
$Q^2$	Four-momentum of the intermediate time-like photon, squared
$q_i^{t/b}(x)$	The quark number density in the nucleon of the target/beam

Table 1.1: Kinematic variables relevant to the Drell-Yan process .

### 1.2.3 Cross-Section

As the participating quarks are asymptotically free within each hadron, there will be no correlations between the probability distributions of the annihilating particles, and the process is independent of the distributions. As a result, the cross section of the Drell-Yan process can be reduced to a function of the electromagnetic annihilation process and the quark probability distribution functions. With these components and some QCD considerations, we can construct it piece by piece.

The first step is to begin with the known hard scattering cross section of  $\epsilon + \bar{\epsilon} \rightarrow l^+l^-$ , where  $\epsilon$  is an

arbitrary particle. This cross section[19] is given by

$$\sigma(\epsilon\bar{\epsilon} \rightarrow l^+l^-) = \frac{4\pi\alpha^2}{3M_{\gamma^*}^2} e_f^2 \quad (1.11)$$

where  $\alpha$  is the electromagnetic fine structure constant,  $e_f$  is the charge of the particle, and  $M_{\gamma^*}$  is the dilepton mass. With this, we add the QCD consideration that only  $q\bar{q}$  of opposite color can annihilate with each other into a colorless virtual photon. Possible combinations are  $R\bar{R}$ ,  $B\bar{B}$ , and  $G\bar{G}$  out of  $3 \times 3$  possible cases. As such, an overall factor of  $\frac{1}{3}$  is added to this cross section. Finally, factoring in the conservation of flavor (there can only be  $u\bar{u}$ ,  $d\bar{d}$ , etc. combinations) and the quark structure of hadrons A and B, we use the product ( $q_f^A(x_1)\bar{q}_f^B(x_2)$ ) of the quark probability distributions for finding quarks of the same flavor-antiflavor combination in the two hadrons. It must also be considered that the quark or antiquark may be found in either hadron A or hadron B. The product of these three factors leads us to the Drell-Yan cross section[12]

$$\frac{d^2\sigma}{dx_1 dx_2} = \frac{1}{3} \frac{4\pi\alpha^2}{3M_{\gamma^*}^2} \sum_f e_f^2 [q_f^A(x_1)\bar{q}_f^B(x_2) + \bar{q}_f^A(x_1)q_f^B(x_2)] \quad (1.12)$$

$$= \frac{4\pi\alpha^2}{9sx_1x_2} \sum_f e_f^2 [q_f^A(x_1)\bar{q}_f^B(x_2) + \bar{q}_f^A(x_1)q_f^B(x_2)] \quad (1.13)$$

where the sum is summing over flavors of quarks ( $f \in \{u, d, s, \dots\}$ ). This can be evaluated in terms of the measurables  $M_{\gamma^*}$  and  $x_F$  via Equations 1.7 and 1.8

$$M_{\gamma^*}^2 \frac{d^2\sigma}{dM_{\gamma^*}^2 dx_F} = \frac{1}{3} \frac{4\pi\alpha^2}{3M_{\gamma^*}^2} \frac{x_1 x_2}{x_1 + x_2} \sum_f e_f^2 [q_f^A(x_1)\bar{q}_f^B(x_2) + \bar{q}_f^A(x_1)q_f^B(x_2)] \quad (1.14)$$

where  $x_1$  and  $x_2$  can be expressed as

$$x_1 = \frac{1}{2} \left[ \sqrt{x_F^2 + 4\tau} + x_F \right], \quad x_2 = \frac{1}{2} \left[ \sqrt{x_F^2 + 4\tau} - x_F \right], \quad \tau = \frac{M_{\gamma^*}^2}{s} \quad (1.15)$$

The cross section can also be represented by dimensionless variables in its scaling form,

$$s \frac{d^2\sigma}{d\sqrt{\tau} dy} = \frac{1}{3} \frac{4\pi\alpha^2}{3} \sum_f e_f^2 [q_f^A(x_1)\bar{q}_f^B(x_2) + \bar{q}_f^A(x_1)q_f^B(x_2)] \quad (1.16)$$

where we introduce the rapidity term  $y$  in describing  $x_1$  and  $x_2$ ,

$$y = \frac{1}{2} \ln \frac{E + p_\ell}{E - p_\ell} = \frac{1}{2} \ln \frac{x_1}{x_2}, \quad x_1 = \sqrt{\tau} e^y, \quad x_2 = \sqrt{\tau} e^{-y} \quad (1.17)$$

It should be noted that with collider experiments, it is conventional to refer to the hadrons A and B in terms of the beam and target hadrons, respectively, and as such,  $x_1$  refers to the the quark in the beam hadron and  $x_2$  refers to the quark in the target hadron.

In each of these equations 1.13, 1.14, and 1.16, the cross sections can be factored into two parts: one subprocess cross section and one part that has only a dependence on the parton distribution functions. They are independent of each other, because one of the staples of the quark parton model is that the PDFs ( $q(x)$  and  $\bar{q}(x)$ ) are independent of the process by which they are probed. This feature is commonly referred to as the “universality” of the PDFs.

### 1.3 PDFs, Structure Functions, and the Quark Parton Model

In the context of hadron-hadron collisions, one can interpret the PDFs as follows: consider two hadrons A and B colliding; a parton of type  $a$  ( $a \in \{u, d, s, g, \dots\}$ ) comes from A and carries with it a fraction of A’s momentum ( $x_A$ ). The same goes for hadron B; a parton of type  $b$  comes from B and carries momentum fraction  $x_B$ . Now, the probability of finding the discussed parton from A at momentum fraction  $x_A$  is given by  $q_{a/A}(x_A)$ . Likewise, the probability of finding the discussed parton from B at  $x_B$  is  $q_{b/B}(x_B)$ .

In general, experimental data measuring  $F_2$  is used in conjunction with some general constraints in order to arrive at the calculated PDFs. One constraint is to consider the known number of valence quarks in a nucleon. Since the function  $q_f(x)$  can be interpreted to be the number density of quark flavor  $f$  as a function of momentum fraction  $x$ , the value  $q_f(x)dx$  represents the number of quarks with flavor  $f$  with fractional momentum in the range of  $[x, x + dx]$ . Therefore, the known number of valence quarks of flavor  $f$  ( $N_f$ ) provides the following condition.

$$\int_0^1 dx[q_f(x) - \bar{q}_f(x)] = N_f \quad (1.18)$$

Another condition considers the value  $xq(x)dx$ , which is the total momentum fraction of the hadron of the number of quarks  $q(x)dx$ . This provides a logical constraint is the summation of the momentum fractions of all partons must add up to the full nucleon momentum:

$$\sum_{q,\bar{q},g} \int_0^1 dx[xq(x)] = 1 \quad (1.19)$$

It should also be noted that the quark PDFs can be split with respect to their spin alignment (+) or

anti-alignment (–) with the nucleon’s spin

$$q(x) = q^+(x) + q^-(x) \quad (1.20)$$

and the polarized (or helicity) PDF can be defined as

$$\Delta q(x) = q^+(x) - q^-(x) \quad (1.21)$$

though, due to the fact that SeaQuest uses neither a polarized  $\Delta q(x)$ . There are two standing proposals, however, to extend the SeaQuest spectrometer for an additional period of data taking, augmenting it with a polarized proton beam (FNAL E-1027) and/or a polarized target (FNAL E-1039). The polarized beam proposal adds two beam-polarizing apparatuses named *Siberian Snakes* to provide sufficiently polarized protons. The polarized target modification calls for the construction and installation of a new cryogenic liquid target system. Both proposals have been approved by the FNAL review committee and are likely to be acted upon near the end of the E-906 contract.

The structure functions  $F_1$ ,  $F_2$ , and  $g_1$  of the nucleon are interpreted in the QPM as the charge-weighted sums over the quark flavors of the corresponding PDFs:

$$F_1(x) = \frac{1}{2} \sum_f e_f^2 q_f(x) \quad (1.22)$$

$$F_2(x) = \sum_f e_f^2 x q_f(x) \quad (1.23)$$

$$g_1(x) = \frac{1}{2} \sum_f e_f^2 q_f(x) \quad (1.24)$$

where here  $f$  represents all flavors of of quarks and anti-quarks. We see above the relation between  $F_1(x)$  and  $F_2(x)$  known as the Callan-Gross relation ( $F_2 = 2xF_1$ ).

Due to the complex nature of lattice QCD<sup>2</sup> simulations, the parton distributions  $q_f(x)$  and  $\bar{q}_f(x)$  within the nucleus are determined empirically, with only a few rules based in theory. The primary probe used to measure them has been deep inelastic scattering (DIS), examining the inclusive jet production in order to get a clearer picture of nucleon structure. Data from many different experiments are combined to extract the unpolarized PDFs. The earlier parametrizations of the PDFs first relied on fits to the measured structure functions solely from DIS experiments which are primarily sensitive to the light quark distributions and are unable to distinguish between quarks and antiquarks of the same flavor. More modern parametrizations use

---

<sup>2</sup>An approach to solving quantum chromodynamics situations by simulating quarks and gluons on a set of lattice points in spacetime and modeling their well-defined interactions.

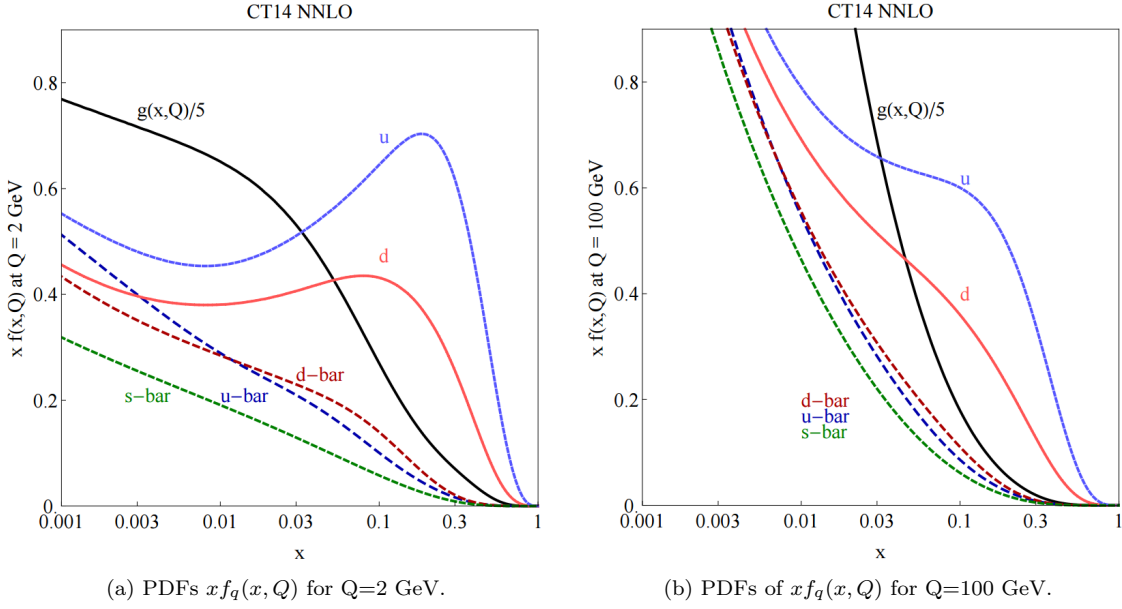


Figure 1.7: Parton distribution functions for quarks and gluons and their  $x$  and  $Q$  dependence as calculated to NNLO by the CTEQ-TEA (CT) global analysis group[14].

many different processes to extract supplementary and complementary information that can be incorporated. Lepton-charge asymmetry observed in  $W^\pm$  production provides additional light quark distribution information. Jet production and photon measurements are also used to set constraints on gluon distributions. It should be noted that Drell-Yan dilepton production from such experiments as E605 and E866 that have contributed constraints on the light anti-quark distributions from the nucleon sea.

The current status of the experimental determination of these PDFs is led by CTEQ (Coordinated Theoretical-Experimental Project on QCD) and TEA (*which stands for???*), and are illustrated in Figures 1.7a and 1.7b. The CTEQ-TEA calculated these PDFs from data on inclusive, high-momentum transfer processes, for which perturbative QCD is expected to be reliable. In the case of deep inelastic lepton scattering, only data with  $Q > 2$  GeV is used. Data in this region are expected to be relatively free of non-perturbative effects, such as higher twists or nuclear corrections. Thus, there is no need to introduce phenomenological models for nonperturbative corrections beyond the leading-twist perturbative contributions[14].

Looking to Figure 1.7 we see that at  $x > 0.1$ ,  $u$  and  $d$  quarks dominate  $\bar{u}$  and  $\bar{d}$  quarks. The SeaQuest spectrometer (described in detail in the next chapter) is a “forward spectrometer”, which means that, for PDF-relevant purposes, the high- $x_F$  ( $x_F > 0$ ) kinematic phase space is explored, which translates to high  $x_1$  and low  $x_2$ . With this consideration, the Drell-Yan process measured at SeaQuest is probabilistically dominated by a quark from the beam annihilating with an anti-quark from the target. Further, all anti-

quarks that exist in the target nucleons must come from what are called the *sea quarks*, or the virtual  $q\bar{q}$  pairs that arise from gluons splitting.

Other interesting observations and measurements that have gone into these distributions are the observations of momentum contributions from all quarks and antiquarks and the momentum fraction from just antiquarks. The momentum sum

$$x_{tot} = \int_0^1 dx[F_2(x)] \simeq \int_0^1 dx[x(q(x) + \bar{q}(x))] \quad (1.25)$$

showed that  $x_{tot}$  for quarks is  $0.512 \pm 0.018$ <sup>[citation needed]</sup>. The rest was found to be attributed to the gluons, though they could not be detected directly by an electron beam in DIS since they carry no electric charge. The momentum fraction from just anti-quarks comes from clever use of another structure function,  $F_3$ .

$$F_3^{\nu N}(x) = q(x) - \bar{q}(x) - 2s(x) + 2c(x) \quad (1.26)$$

$$F_3^{\bar{\nu} N}(x) = q(x) - \bar{q}(x) + 2s(x) - 2c(x) \quad (1.27)$$

$$F_3(x) = \frac{1}{2}[F_3^{\nu N}(x) + F_3^{\bar{\nu} N}(x)] = q(x) - \bar{q}(x) = u_v(x) + d_v(x) \quad (1.28)$$

Here, the  $v$  subscript denotes valence quark distributions,  $q/\bar{q}(x)$  are

$$q(x) = u(x) + d(x) + s(x) + c(x) \quad (1.29)$$

$$\bar{q}(x) = \bar{u}(x) + \bar{d}(x) + \bar{s}(x) + \bar{c}(x) \quad (1.30)$$

and the individual  $F_3^{\nu/\bar{\nu} N}$  structure functions are measured from  $\nu N$  and  $\bar{\nu} N$  scattering and then combined<sup>[citation needed]</sup>. With  $F_3$ , there is the Gross-Llewellyn Smith (GSL) sum rule[18]

$$\int_0^1 F_3(x) = 3 \quad (1.31)$$

which is to say that there are three valence quarks. The new information gained here with  $F_3$  though is the measurement of  $\int dx[xF_3(x)] = 0.341 \pm 0.036$ , which gives the momentum fraction carried by the valence quarks. Put this together with the results of Eq. 1.25 and one can derive the conclusion that the anti-quarks in the nucleon possess between 13% and 17% of the nucleon's momentum[16].

The last interesting sum rule to discuss is the Gottfried sum rule which is focused on flavor asymmetries

between the proton and its isospin partner, the neutron.

$$S_G = \int_0^1 dx \left[ \frac{F_2^p - F_2^n}{x} \right] \quad (1.32)$$

$$= \int_0^1 dx \left[ \sum_f e_f^2 [q_f^p(x) + \bar{q}_f^p(x) - q_f^n(x) - \bar{q}_f^n(x)] \right] \quad (1.33)$$

We assume charge symmetry insofar as  $u^p(x) = d^n(x)$  and  $\bar{u}^n(x) = \bar{d}^p(x)$ , yielding

$$S_G = \int_0^1 dx \left[ \frac{1}{3} (u(x) + \bar{u}(x) - d(x) - \bar{d}(x)) \right] \quad (1.34)$$

where these PDFs refer to the distributions in the proton. By some reorganization and grouping, this can be re-expressed in a more familiar way.

$$S_G = \int_0^1 dx \left[ \frac{1}{3} [u(x) - \bar{u}(x)] \right] - \int_0^1 dx \left[ \frac{1}{3} [d(x) - \bar{d}(x)] \right] - \int_0^1 dx \left[ \frac{2}{3} [\bar{d}(x) - \bar{u}(x)] \right] \quad (1.35)$$

The first two integrals here are the definitions of the valence quark sum rule mentioned in Eq. 1.18, and this is known to be 2 and 1 for the  $u$  and  $d$  valence quarks of the proton, respectively. As a result, we arrive at the common representation of the Gottfried Sum Rule (GSR).

$$S_G = \frac{1}{3} - \int_0^1 dx \left[ \frac{2}{3} [\bar{d}(x) - \bar{u}(x)] \right] \quad (1.36)$$

If one were to assume that, within a proton,  $\int dx[\bar{u}(x)] = \int dx[\bar{d}(x)]$ , then this sum reduces to  $\frac{1}{3}$ . More on this sum and its measured violation in a later section.

### 1.3.1 Drell-Yan Tests of the QPM

The Drell-Yan process can be described within the frameworks of QPM and QCD, so it provides a good testing ground for these models. The testing process begins with establishing the validity of the naïve Drell-Yan quark-parton model. Once this is done, detailed studies of how

- *Point-like quarks*
- *quark charge*
- *quark spin*

- end with departure of Drell-Yan from QPM with scaling violation and the magnitude of DY over prediction (K-Factor), and  $pT$

## 1.4 QCD-Improved Drell-Yan

- Gluon interactions complicate the naïve DY picture,
- Describe QCD corrective processes
- Maybe move  $\alpha_s$  and running of coupling constant to here
- Introduce  $Q$ -dependence of PDFs
- QCD calculation of K-factor
- Transverse momentum in QCD picture

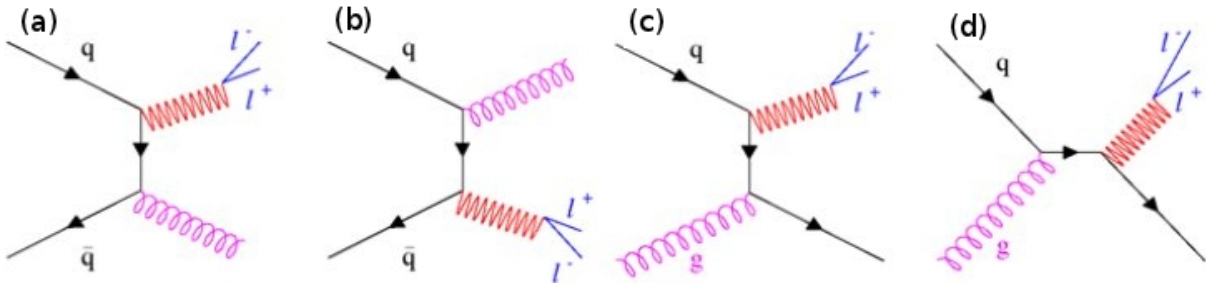


Figure 1.8: The Drell-Yan process has a large range of higher-order QCD corrections that need to be accounted for. (a) and (b) are high order  $q\bar{q}$  annihilations, and (c) and (d) are gluon “Compton scattering” terms.

## 1.5 Drell-Yan and Sea Quark Phenomenology

### 1.5.1 $\bar{d}/\bar{u}$ Asymmetry

*Start with Gottfried sum violation, give rough derivation of  $d\bar{u}/u\bar{d}$ , previous results, a model, and what SeaQuest proposes to provide, stats-wise.*

### 1.5.2 The EMC Effect

*Start from the very beginning with EMC in 1983, discuss current understanding. Draw from review paper and the SeaQuest Academy talks by Don and Arrington.*

The European Muon Collaboration, in 1983, measured the DIS cross section per nucleon ratios of  $Fe$  to  $D$  over a large kinematic range. The result, as seen in the top right of Figure ?? came as quite a surprise. It was revealed that the structure function of a nucleon bound in a nucleus differs fundamentally from that of a free nucleon [5]. This difference was not a simple or small effect either; the cross section per nucleon of a nucleus showed to be smaller than that of deuterium at very low  $x_2$ , greater than deuterium at  $0.1 < x_2 < 0.2$ , and then steadily less than deuterium for  $0.2 < x_2 < 0.6$ . This complex, unexplained behavior opened up a new field of research and theoretical work. Following suit, the different aspects of this nuclear modification garnered some common nicknames. The region where  $x_2 < 0.1$  became known as “*Nuclear Shadowing*”, the transition region of  $0.1 < x_2 < 0.2$  is known as “*Anti-shadowing*”, and the linear decline in the ratio of cross sections between  $0.2 < x_2 < 0.6$  is generally referred to as the “*EMC Effect*” [17].

Recent experiments at Hall C at JLab and SLAC suggest the following regarding the EMC Effect [31]:

- It is  $Q^2$ -independent
- Its x-dependent shape is universal (across various nuclei)
- The magnitude (slope) of the effect varies with A
- It thereby might be related to nuclear density

### 1.5.3 Models For the EMC Effect

#### Pion Cloud Model

#### Nuclei-Nuclei Short Range Correlations

### 1.5.4 E-772 at Fermilab

### 1.5.5 Nuclear Dependence of Drell-Yan at SeaQuest

- *Talk about what will be measured*
- *Which targets will be used*
- *What kinematic phase space in  $\{x_1, x_2\}$  will be explored*

- *What the statistics will be, approximately*
- *What, if anything, will be compared to models*

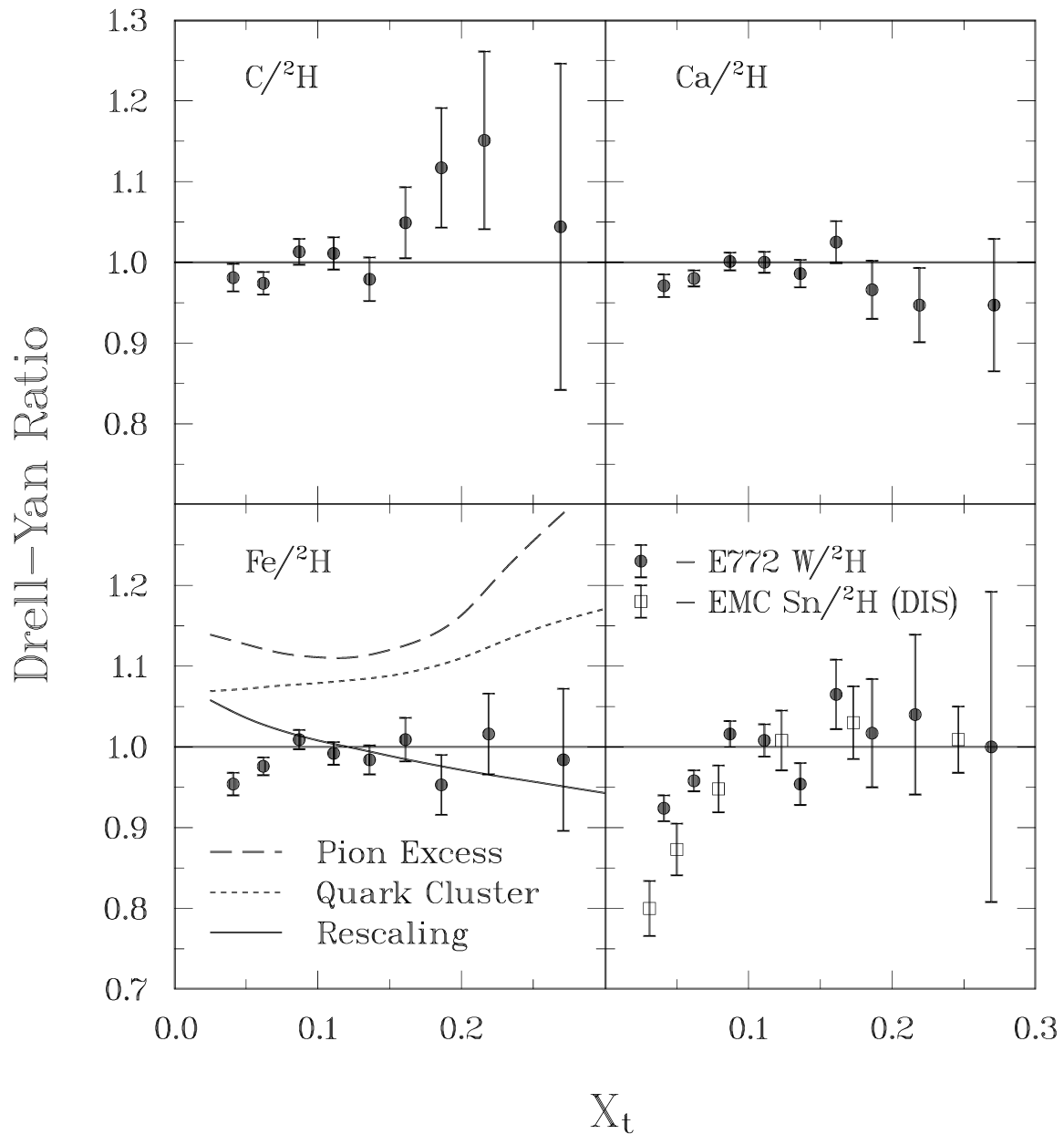


Figure 1.9: E-772 Drell-Yan  $\frac{A}{{}^2H}$  ratios for several nuclear targets as a function of  $x_2$  ( $x_t$ )[3].

# Chapter 2

## Apparatus

### *CHAPTER STATUS: FIRST DRAFT COMPLETE*

SeaQuest is the operational name of Fermilab Experiment #906 (*E-906*) performed at its Neutrino-Muon (*NM*) experimental area. The experiment was designed to take *high-intensity beam* at relatively *low center-of-mass energy*, provide *good mass resolution*, and allow for *accurate target-to-target systematic normalization*. The apparatus consists of a moving target table, two dipole magnets, 8 hodoscope planes, 24 drift chamber planes, and 4 proportional tube planes. Upstream of the target table (towards the beam source), there is also a Čerenkov counter for beam intensity monitoring and there are several segmented wire ionization chambers (SWIC's) for beam profiling.

### 2.1 Apparatus Overview

SeaQuest is a fixed-target experiment. In this style of experiment, a stationary target is placed in the path of an accelerated beam of particles, as opposed to *collider* experiments where two accelerated beams are directed against each other, in opposite directions. The proton beam interacts with the target material and produces a variety of daughter particles. These daughter particles are tracked through a forward spectrometer and selectively filtered dependent on the purpose of the study.

The tuned and monitored 120 GeV proton beam is sent from the Fermilab Main Injector (MI) where the beam protons strike one of 7 targets. The high-momentum charged particles that are produced are focused into the acceptance of the experiment's detectors with the solid iron dipole magnet, FMAG, or NM3S. This solid focusing magnet also sweeps away low-momentum particles and acts as a beam dump / absorber.

The SeaQuest Spectrometer (Fig. 2.1) consists of the aforementioned focusing magnet, several tracking chambers that record the positions of charged particles through the length of the spectrometer, and an analyzer magnet to bend the particles between tracking stations. The spectrometer measures particle momenta by recording the bend of each charged particle as it passed through the analyzer magnet, where the magnetic field is known. This is performed by reconstructing the trajectory of a particle in one-half of

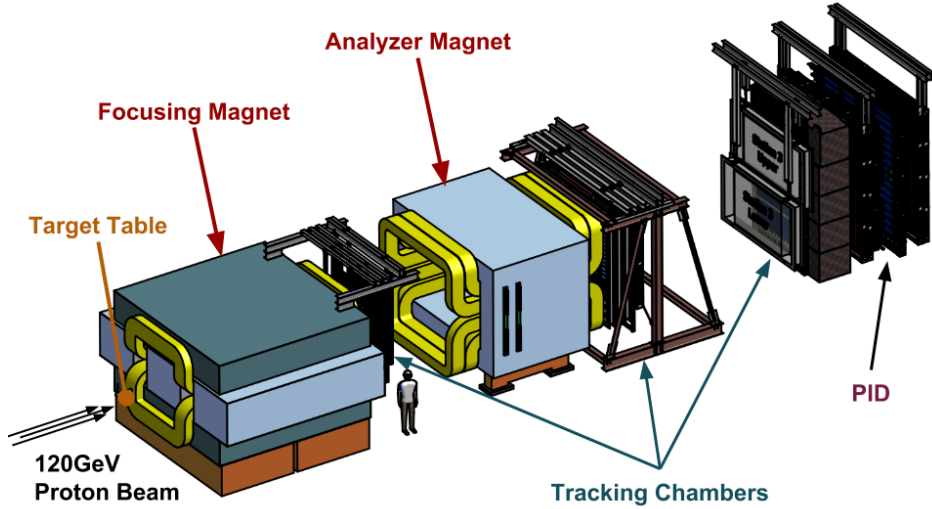


Figure 2.1: Perspective view of the SeaQuest spectrometer apparatus.

the spectrometer (before the analyzer magnet) and then similarly reconstructing the trajectory of particles in the other half. If two trajectories can be matched up, then the particle momentum can be extracted by taking the ratio of the magnet's  $p_T$ -kick to the change in the track's direction.

The spectrometer's geometric design and event triggering selection is optimized to detect oppositely-charged pairs of muons while minimizing the sensitivity to various sources of unwanted backgrounds. Positive identification of muons is achieved by requiring signals in the hodoscopes for known muon “roads” along with requiring signals in the proportional tubes located at the farthest end of the experiment, past an iron wall. Electrons and any hadrons are stopped by the solid iron focusing magnet and iron wall farther down while muons will pass through them unencumbered.

The coordinate system is defined as the following: the  $z$ -axis points along the beam direction, the  $y$ -axis points upwards vertically, and the  $x$ -axis lies along the horizontal direction in such a way that a right-handed coordinate system is formed. The terms *upstream* and *downstream* are often used when referring directions or regions in the experimental hall. *Upstream* often refers to the direction towards the beam source ( $-z$  direction), while *downstream* refers to the  $+z$  direction of the beam trajectory. The origin of the coordinate system was chosen to be the point where the proton beam meets the *upstream*-facing surface of FMAG, the solid focusing magnet.

## 2.2 Main Injector Proton Beam

*Maybe a graphic of FNAL accelerator?*

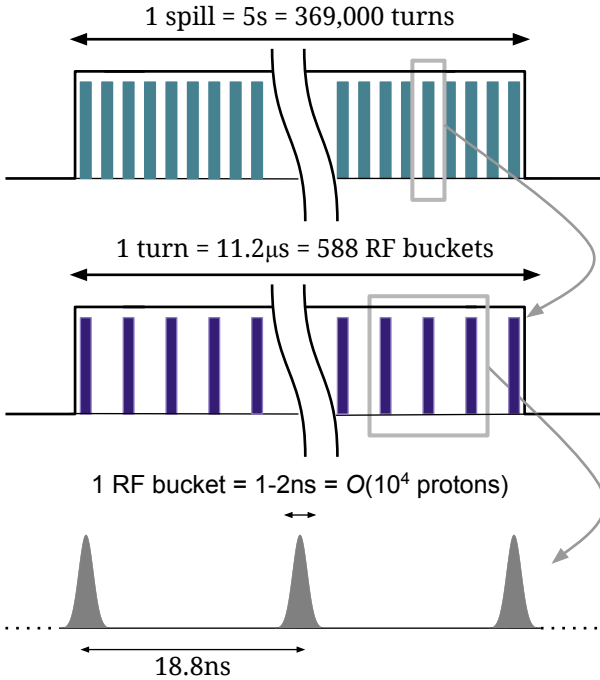


Figure 2.2: Spill structure of the beam delivered to SeaQuest.

The Fermilab Main Injector (MI) receives protons that have been accelerated by the Radio Frequency Quadrupoles (RFQ), the Linear Accelerator (LINAC), and the Booster, and it continues to accelerate them from 8 GeV up to the nominal energy of 120 GeV. Along the way, radio-frequency cavity (RFC) accelerators in the LINAC and the MI ‘bunches’ up the protons such that the beam has its characteristic 53.1 MHz structure. After the period of acceleration, the protons are then ‘scraped off’ slowly with each passing *turn* of the collected proton beam and sent down the Neutrino-Muon (NM) beam delivery line for approximately five seconds of every minute, called a ‘slow spill’ or just ‘spill’. Beam is extracted using a resonant process, and the extracted beam retains the 53.1 MHz structure of the Main Injector RFC. Each bunch, or ‘bucket’, of protons is less than 2 ns long and the time between bunches is approximately 18.8ns. The spill structure of the beam is depicted in greater detail in Figure 2.2.

The beam sent to SeaQuest is not uniform in time throughout the spill. There are beam bunches in the MI that are intentionally left empty so that the abort kickers can ramp to a full field during a gap in the beam. There are also bunches left empty to allow the injection kickers to inject 8 GeV protons from the Booster without disturbing bunches of protons already in the Main Injector. Typically, 498 of the 588 ‘RF buckets’ in the Main Injector contain protons during the SeaQuest slow spill cycle. It is the case, however, for SeaQuest, that the intensity of the bunches corresponding to these 498 full buckets varies

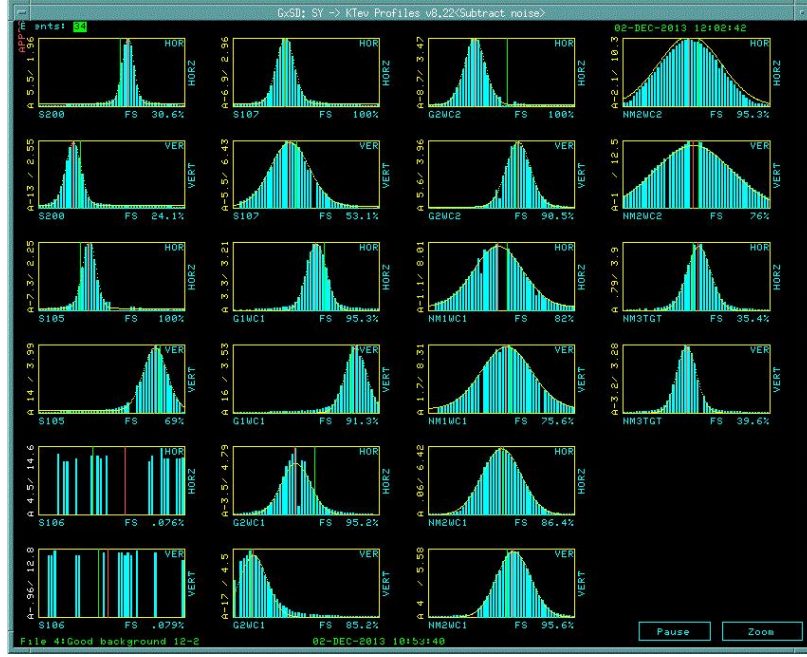


Figure 2.3: Beam profile detailed by SWIC detectors along the NM beam line.

greatly throughout the slow spill. On *average*, each bucket will have  $\mathcal{O}(10^4)$  protons and the spill has an intensity of approximately  $2 \times 10^{12}$  protons per second and therefore about  $1 \times 10^{13}$  protons delivered per spill.

Several guiding and focusing magnets bend and deliver beam to the NM beamline which serves both the test beam facility and SeaQuest at NM4. The beam is focused to a width of  $250\mu\text{m}$ . The profile, position, and intensity are measured along the NM beamline by several detectors. The intensity of the beam is monitored by an ion chamber (IC) and a secondary emission monitor (SEM) in the NM3 sector of the beamline. The beam profile and position are monitored by SWICs and beam-position monitors (BPMs), respectively. The Accelerator Control Network (ACNET) display of the SWIC readout can be seen in Figure 2.3. The closest BPMs and SWICs to the spectrometer were located in NM2 enclosure. The beam profile does not maintain its  $250\mu\text{m}$  shape and spreads slightly as it moves towards the spectrometer. The final beam profile is measured by inspecting the upstream-facing side of the solid targets, and it was found to be approximately 6mm wide by 1mm high.

## 2.3 Beam Intensity Monitor

SeaQuest's trigger system (described in detail later) mostly fires on fake dimuons caused by two low  $p_T$  muons from unrelated pion decays. The hits in downstream hodoscopes from the pions combined with hits

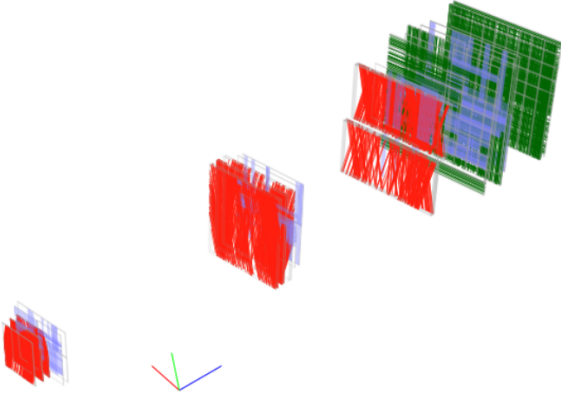


Figure 2.4: A single high-intensity event with majority of all detector elements firing off. White space within the rectangles indicates inactive elements whereas red, blue, and green represent elements which have fired during that event. Track reconstruction in these cases is impossible.

in the upstream hodoscope from two other unrelated particles frequently add up to a false dimuon signal. Since this type of fake trigger involves four unrelated particles, the probability that a trigger will occur increases with  $I^4$ , where  $I$  is the intensity of the beam bucket; the number of protons in the triggered beam bunch.

The SeaQuest data acquisition system (also described later in detail) can read out approximately 3000 events per second without significant dead time. During the commissioning run of SeaQuest, the trigger rate was very high and the trigger dead time was close to 100%. These triggers were taken at such high beam intensities that the occupancy of all SeaQuest detector elements was more than 50%, making pattern recognition essentially impossible (see Figure. 2.4). The Beam Intensity Monitor (BIM) was designed to solve this problem.

The SeaQuest Beam Intensity Monitor (BIM) senses when the beam intensity is above a programmable threshold. If an RF bucket with an intensity above this threshold is detected, the BIM sends a signal to inhibit certain triggers until the intensity once more falls below the threshold. The inhibit threshold is tuned frequently as trigger and beam conditions change, but it is typically set at  $\sim 95,000$  protons per RF bunch. For reference, a full RF bucket at an intensity of  $2 \times 10^{12}$  protons per spill is  $\approx 10,000$  protons.

The beam intensity is measured using an atmospheric pressure gas Čerenkov counter. A gas mixture of 80% Argon and 20% CO<sub>2</sub> is used as the Čerenkov radiator. The counter and readout electronics were designed to have  $O(ns)$  time resolution, and a linear response over a large dynamic range. A diagram of the counter is shown in Figure 2.5. A 45 degree aluminized Kapton mirror directs light to a single photomultiplier tube. A *baffle* of black construction paper held parallel to the mirror ensures that the proton path length

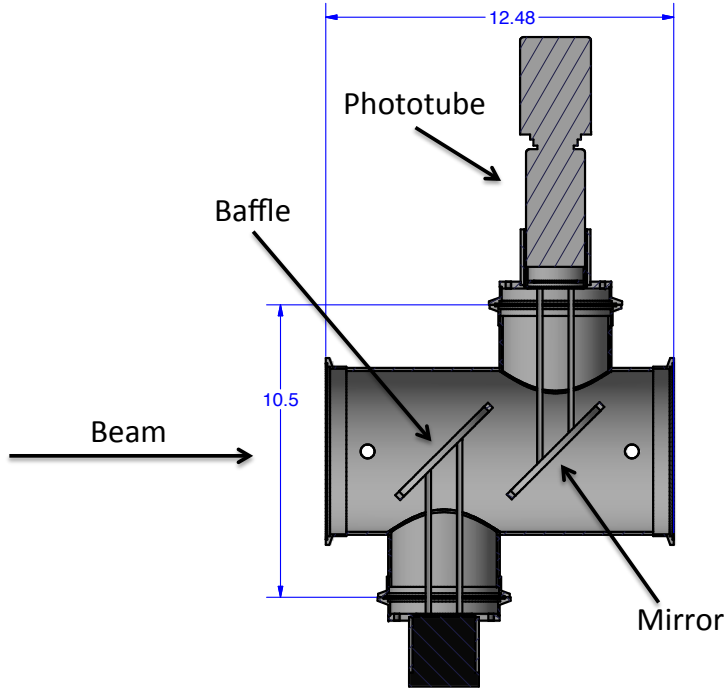


Figure 2.5: The Beam Intensity Monitor (BIM) Čerenkov counter. Measurements are in inches.

through the light-radiating gas with respect to the mirror is independent of beam position. A two-inch diameter 8-stage photomultiplier tube (PMT) is positioned close to the mirror so that all Čerenkov light created between the baffle and the mirror falls directly on the aperture of the PMT. It was observed during the commissioning run that after exposure to  $\approx 3 \times 10^{17}$  protons ( 3 weeks of uninterrupted usage), the mirror reflectivity is significantly reduced in the beam spot, and the mirror then needs to be replaced.

The signal from the BIM is integrated and digitized using a custom charge (Q) integrator and encoder (QIE) integrated circuit board, which comes from a family of circuits used first by the KTeV experiment at Fermilab[36]. The chip is clocked with the Main Injector RF clock and provides an ADC (analog-digital conversion) every 18.8ns clock cycle. The light incident on the photomultiplier tube is attenuated using neutral density filters (NDF's) so that the QIE least count corresponds to  $\sim 30$  protons per beam bunch.

In addition to inhibiting triggers during high-intensity periods of beam, the BIM readout module also provides critical information used to calculate the number of protons incident on the SeaQuest targets while the experiment is ready and able to trigger. This value is needed to normalize SeaQuest cross section measurements. The BIM readout module provides the following:

- Sum of all ADC signals for the entire spill (QIESum).

- Sum while inhibit is asserted at trigger logic.
- Sum during trigger dead time.
- A snapshot of beam intensity 16 buckets before and after the triggered RF bucket

These are used to calculate a ratio of protons that were ‘live’ (the experiment can trigger) via the following:

$$\%_{\text{live}} = \frac{QIESum - (\text{inhibit sum} + \text{dead time sum})}{QIESum} \quad (2.1)$$

$$\text{liveProton} = \text{totalProton} \cdot \%_{\text{live}} \quad (2.2)$$

where “totalProton” is the intensity value recorded from the SEM detector located just upstream of the BIM Čerenkov counter. The SEM itself is calibrated by foil activation. The snapshot of the triggered RF bucket intensity along with the 32 surrounding RF bucket intensities is used for studies and corrections of the rate-dependent effects on detector efficiencies and reconstructed measurements.

## 2.4 The SeaQuest Targets

A wide range of atomic weights (from 2 to 184) is required to do an A-dependence study of the Drell-Yan process. At SeaQuest, the targets used are  $^1H(\ell)$ ,  $^2H(\ell)$ ,  $C$ ,  $Fe$ , and  $W$ . In addition to the two liquid targets and the three solid targets, two positions on the target table were used for measuring background signal rates: an empty flask, identical to the flasks used for the  $^1H$  and  $^2H$  targets, and a single empty solid target holder. Colloquially speaking: the  $^1H$  target is interchangeably referred to as the liquid hydrogen target,  $\ell H_2$ ,  $LH2$ , or  $H_2$ ;  $^2H$  is likewise referred to as the liquid deuterium target,  $\ell D_2$ ,  $LD2$ , or  $D_2$ ; the empty flask is referred to as the “Empty” target; the empty solid target holder is referred to as the “None” target.

These are all mounted on a laterally-moving, remotely positionable table (in the  $\pm x$  direction), able to move over a range of 91.4cm. The table’s center is located at  $(0, 0, -1.25)$  meters, directly in front of the upstream face of FMAG, the solid iron focusing magnet. Because of the  $\sim 5.0$ cm diameter of the targets and the 6x1mm dimensions of the beam, the targeting efficiency was 100%. The details of the target materials are summarized in Table 2.1, and the layout of the target table can be seen in 2.6.

The  $H_2$  gas used is “Ultra High Purity 5.0 Grade” or 99.999% pure. The deuterium has come from two different sources. The first of these is a Fermilab-provided supply of gas left over from previous bubble chamber experiments. This gas was known to have a small hydrogen contamination and was measured by

Position	Material	Density [g/cm <sup>3</sup> ]	Thickness [cm]	Interaction Length	Spills/ Cycle (%spills)
1	$H_2$	0.07065	50.8	0.06902	10 (43%)
2	Empty	NA	NA	0.0016	2 (9%)
3	$D_2$	0.1617	50.8	0.1144	5 (22%)
4	None	NA	NA	0.0	2 (9%)
5	Iron	7.874	1.905	0.1135	1 (4%)
6	Carbon	1.802	3.322	0.0697	2 (9%)
7	Tungsten	19.30	0.953	0.0958	1 (4%)

Table 2.1: Characteristics of the seven SeaQuest target positions. The “Spills/Cycle” is only a typical configuration and can vary according to needs and running configurations. The non-zero interaction length of the empty flask is due to the 51 $\mu$ m-thick stainless steel end-caps of the flask and the 140  $\mu$ m-thick titanium windows of the vacuum vessel that contains it.

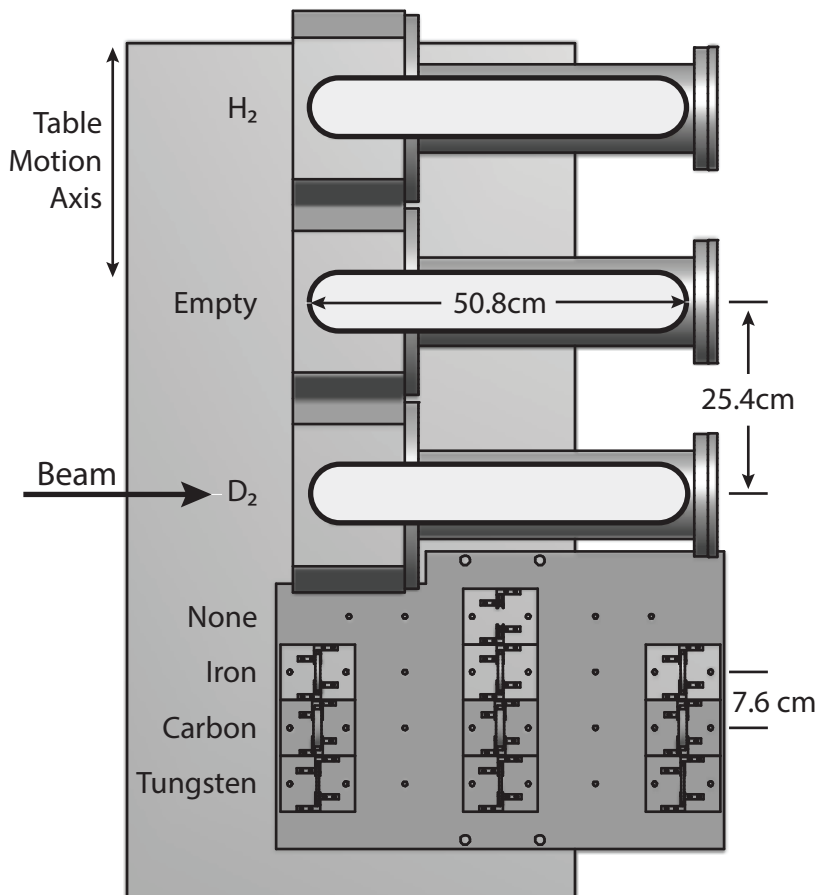


Figure 2.6: The layout of the target table and its seven target positions, as seen from above.

mass spectroscopy to have a composition of 85.2% D<sub>2</sub>, 12.7% HD, 1.2% <sup>4</sup>He, and 0.8% H<sub>2</sub> by mole. As the analysis of experimental data commenced, handling the ramifications of the D<sub>2</sub> impurity came under focus. Unexpected bottle-to-bottle variation in contamination became evident, and the sample-taking methodology itself for spectroscopy became suspect of introducing contamination. In order to no simplify analysis and reduce the substantial complexity and cost of further gas analysis, SeaQuest switched to commercially available “Research Grade” D<sub>2</sub>, which is better than 99.6% pure with virtually all HD to balance. The data analyzed in this paper deals with the impure D<sub>2</sub> target material before this switch. Further information on the D<sub>2</sub> composition and how it is handled in the context of analysis will be covered in Chapter 5.

Each of the three solid target positions is divided into three disks of 1/3 the total thickness provided in Table 2.1. These disks are spaced 25.4cm apart to approximate the distribution of the liquid target, thereby minimizing target-dependent variation in spectrometer acceptance. The one exception to this is that during the Run II period the iron disks were more closely spaced (17.1cm). The decision to place these iron disks closer together than the rest during Run II is still unclear.

The target table is able to move between two different targets in about 30 seconds. This allows a change between targets in the 55 seconds between successive spills. With this frequent target interchange, the systematic uncertainties associated with drifts in beam characteristics, monitor gains, and detector efficiencies are reduced to a minimum when investigating A-dependent ratios. How much beam time each target received is determined by interaction lengths of the targets along with the amount of statistics desired for certain targets. As the flagship measurement of SeaQuest is the  $\bar{d}/\bar{u}$  asymmetry, more emphasis was placed on the hydrogen and deuterium than the nuclear targets. The spills per cycle and beam time allocation can be found in Table 2.1.

## 2.5 Focusing and Analyzing Magnets

Two large dipole magnets are used in the experiment to select forward going ( $x_F > 0$ ) dimuons, reject low-momentum particles, and analyze their kinematic characteristics. The most upstream magnet, denoted “FMAG”, is a solid iron A-frame magnet with an aperture of 1.22m in the  $x$ -direction and 66cm in the  $y$ -direction. It is assembled from 43.2cm x 160cm x 503cm iron slabs, as shown in Fig. 2.7. The magnet has no air gap, and the iron has extremely high purity, allowing a 2000A excitation current to generate a nearly constant, central magnetic field of 1.9 Tesla (yielding a 2.91 GeV/c total magnetic deflection). The field is generated by exciting the embedded aluminum “*bedstead*” coil to 2000 Amps at 25 Volts (50 kW). The current exciting FMAG is monitored by the Fermilab ACNET system and is broadcast to the SeaQuest

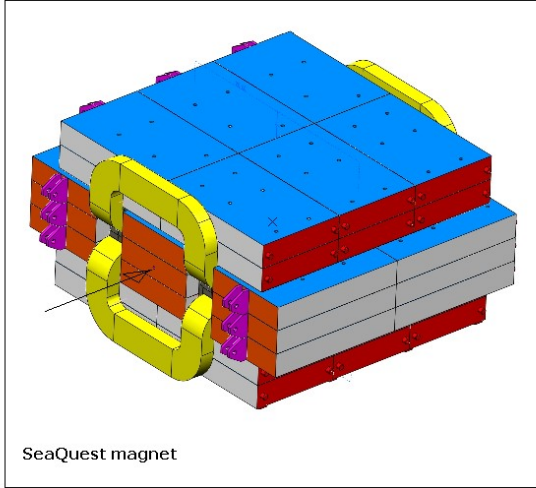


Figure 2.7: Perspective drawing of FMAG’s aluminum coils embedded in an arrangement of iron slabs.

slow data acquisition system every acceleration cycle. The excitation is also input to the beam-disabling safety system in order to prevent the beam from hitting the SeaQuest spectrometer when FMAG is not fully powered. FMAG also acts as the beam dump for the 120 GeV beam. There is a 5cm diameter by 25cm deep bore drilled into the upstream end of FMAG (recall, this is the origin of the experiment’s coordinate system). The 120 GeV protons that do not interact in the SeaQuest targets 125cm upstream of FMag, interact in the central iron slab. Most of the 2.0 kW beam power is dissipated in this slab and is eventually conducted to the coils and external surfaces to be radiated away.

The downstream magnet, denoted “KMAG”, is a 300cm long iron rectangular magnet with a 289cm wide by 203cm high central air gap. It was originally constructed by the KTeV collaboration[2] at Fermilab. It is excited to a central field of 0.4 Tesla (0.402 GeV/c magnetic deflection) by 1600 Amps at 270 Volts (430kW). The spatial distribution of the magnetic field in KMAG was measured by the KTeV group and re-verified by SeaQuest. In normal running conditions, both FMag and KMAG bend muons horizontally in the same direction. This two-magnet configuration is often referred to as a focusing spectrometer.

The 2.91 GeV/c and 0.402 GeV/c magnetic deflections deliver a transverse-momentum ( $p_T$ ) kick along the to charged particles passing through the spectrometer. The magnets bend the paths of the muon in the  $\pm x$  direction, with the sign depending on the orientation of the magnetic fields and the particles’ charges. Between Run II and Run III of data taking, the current direction was reversed, thereby reversing the direction of the magnetic fields. During Run II, the magnetic fields were pointing in the  $-y$  direction, and in Run III, the magnetic fields were flipped to point in the  $+y$  direction. This was done for two reasons: (1) to identify any left-right asymmetries in the experiment, and (2) to limit the amount of radiation on the electronics in the experimental hall, as a large number of positive particles were being swept directly

towards the electronics racks during Run II.

*Note: Maybe add something track resolution effects due to multiple scattering in FMAG? Or save for Analysis chapter?*

## 2.6 Beam Dump, Shields, and Absorbers

In order to prevent damage to the downstream detectors from the beam and reduce signals from incidental radiation, the spectrometer is designed with a beam dump and two hadron absorber walls. Approximately 125cm downstream of the target table is the water-cooled beam dump whose upstream face is located at (0.0, 0.0, 0.0) m. The beam dump is one of the many solid iron 5m blocks that fill and surround the FMAG coils. The whole length of the beam dump along the beam axis is equivalent to  $\approx 35$  nuclear interaction lengths of iron.

Between the downstream face of FMAG and Station 1, there is a 2 cm thick wall of borated polyethylene which is put in place as a fast neutron shield. This material is 5% boron by weight, with the rest being polyethylene. The polyethylene contains high hydrogen content, making it an effective fast neutron radiation shield, slowing down the fast neutrons down to thermal speeds. The boron in the material provides attenuation of thermal neutrons, thus reducing the levels of capture-gamma radiation elsewhere in the experiment. Borated polyethylene at this thickness is a common and optimal neutron shielding material for areas of low to intermediate neutron flux where the temperature is below 82°C *[citation needed]*. These conditions make the downstream side of FMAG ideal for its placement.

Farther downstream, there is another hadron absorber wall located between Station 3 and Station 4. The absorber wall consists of a stack of 98cm thick iron blocks. This is an equivalent of  $\approx 6$  nuclear interaction lengths. The purpose of this wall is to identify muons at the rear of the apparatus by effectively blocking all other types of particles. The only charged particles which can penetrate this absorber wall that weren't swept away by either magnet are muons.

## 2.7 Tracking Detectors

The tracking detectors are the instruments used for measuring the values of the kinematic variables of the dimuon pairs. Several different types of detectors are grouped together to form a detector *Station*. The types of detectors used are hodoscopes, wire chambers, and proportional tubes. There are four stations throughout the experimental hall that provide tracking information at different points along the spectrometer, numbered from 1 to 4 in order of increasing  $z$ . Station 1 is located between FMAG and KMAG. Station 2 is located

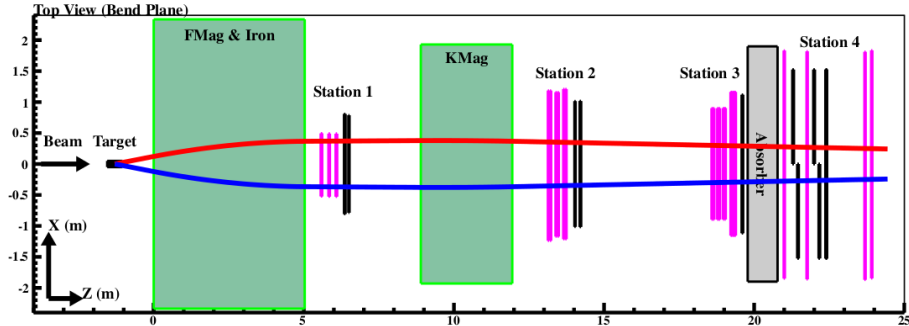


Figure 2.8: Spectrometer layout of FMAG, KMAg, and Detector Stations 1-4.

at the downstream face of KMAg. Station 3 and 4 are just upstream and downstream, respectively, of the iron absorber wall. The Station layout can be seen in Fig. 2.8

### 2.7.1 Triggering Hodoscopes

Hodoscope arrays are located at each of the four detector stations. These detectors' primary usage is to select events with two opposite-signed muon tracks in them. Certain 'roads' through the spectrometer are defined in the fast trigger logic, and when two desired roads are observed in a given event, the trigger system tells the data acquisition systems to record that event's data. In addition to this, the hodoscopes provide analysts with the ability to discard or ignore certain hits in adjacent chambers for which there is no corresponding nearby hodoscope hit. This is useful in decreasing the hit multiplicities in the wire chambers, which in turn decreases the combinatoric complexity of reconstruction algorithms.

Each of the eight hodoscope planes is split into two halves: top and bottom in the case of planes with vertically-oriented paddles, or left and right for planes with horizontally-oriented paddles (denoted by 'T', 'B', 'L', and 'R', respectively). In each half-plane, the hodoscopes are a set of long rectangles arranged 'picket fence'-style with a small 0.3175cm overlap, as to prevent any particles from possibly slipping between paddles. A single hodoscope detector element is composed of plastic scintillator material connected to Philips XP 2008 photomultiplier tubes (PMT) by plexiglass light guides. Stations 1, 2, and 4 each have two hodoscope planes, with planes of both vertically- and horizontally-oriented paddles (for measuring in  $x$  and  $y$ , respectively). Station 3 consists only of vertically-oriented plane, and thus measures in the  $x-z$  direction only, which is in the experiment's  $x-z$  bend plane. The hodoscope planes are named according to detector station and the direction that they measure. For example, the  $y$ -measuring hodoscope plane in Station 2 is called "H2Y". The individual half-planes are named according to detector station and which half it is of the two. For example, the top half of the  $x$ -measuring hodoscope plane in Station 1 is referred to as

“H1T”. As such, the “H3X” detector is composed of “H3T” and “H3B”. The detailed specifications of each hodoscope plane are given in Table 2.2. A precise alignment of the hodoscopes was achieved by examining the distributions of positions of tracked muons at each hodoscope plane when a given hodoscope element in that plane was fired.

Detector	Paddle Width [cm]	Overlap [cm]	# of paddles (per half-plane)	Width × Height (per half-plane) [cm] × [cm]	<i>z</i> -position [cm]
H1X	7.32	0.3175	23	162 × 70	666
H1Y	7.32	0.3175	20	79 × 140	653
H2X	13.00	0.3175	16	203 × 152	1421
H2Y	13.00	0.3175	19	132 × 241	1400 (L), 1406 (R)
H3X	14.59	0.3175	16	228 × 168	1959
H4X	19.65	0.3175	16	305 × 183	2234 (T), 2251 (B)
H4Y1	23.48	0.3175	16	152 × 366	2130 (L), 2146 (R)
H4Y2	23.48	0.3175	16	152 × 366	2200 (L), 2217 (R)

Table 2.2: Parameters of all hodoscope planes. *z*-positions of H2Y and H4 half-planes are offset slightly due to the half-planes themselves overlapping.

## 2.7.2 Drift Chambers

Each of Stations 1, 2 and 3 is equipped with a drift chamber (DC) to measure the passing *x* and *y* positions of muons at its *z* location, with each DC flat vertical to the *z* axis, and a drift cell is of the box shape. These measured positions are critical for reconstructing the trajectory of muons, and thereby their kinematics. Each DC contains six drift chamber planes, arranged in three pairs with parallel wire orientations (each pair referred to as a “view”). Wires oriented vertically (*x*-measuring) are referred to as being in the “X” view and at angles of  $+14^\circ$  and  $-14^\circ$  with respect to the *y*-axis are the “V” and “U” planes, respectively. The second plane in each view is offset from the first by one-half of a wire-to-wire distance (“cell width”) in order to resolve the left-right ambiguity of drift direction. This offset plane of each pair is referred to as the *primed* plane, and is denoted with a ‘*r*’. So, in each DC, there are X, X’, U, U’, V, and V’ planes, with primed and unprimed planes (like X and X’) constituting a view.

The individual drift chambers at Stations 1 and 2 are called “D1” and “D2”, respectively. Station 3 has two drift chambers since the desired acceptance area it has to cover is substantially larger than one DC can cover. These are split vertically to cover the top and bottom halves, and are called “D3p” and “D3m” where “p” and “m” stand for “plus” and “minus”. Table 2.3 summarizes the parameters of the DC’s. D1 and D3m have been upgraded during the data taking, as listed in Tab. 2.4. This original and upgraded versions are referred to as DN.1 and DN.2, respectively.

Chamber	Plane	Number of wires	Cell width [cm]	Width $\times$ height [cm] $\times$ [cm]	$z$ -position [cm]
D1.1	X	160	0.64	102 $\times$ 122	617
	U, V	201	0.64	101 $\times$ 122	$\pm 20$
D1.2	X	320	0.50	153 $\times$ 137	617
	U, V	384	0.50	153 $\times$ 137	$\pm 1.2$
D2	X	112	2.1	233 $\times$ 264	1347
	U, V	128	2.0	233 $\times$ 264	$\pm 25$
D3p	X	116	2.0	232 $\times$ 166	1931
	U, V	134	2.0	268 $\times$ 166	$\pm 6$
D3m.1	X	176	1.0	179 $\times$ 168	1879
	U, V	208	1.0	171 $\times$ 163	$\pm 19$
D3m.2	X	116	2.0	232 $\times$ 166	1895
	U, V	134	2.0	268 $\times$ 166	$\pm 6$

Table 2.3: Parameters of all chambers. Those of primed planes are almost the same as of unprimed planes. The  $z$ -positions of U and V planes are relative to those of X planes.

Run	Period	Chamber combination
1	2012 Mar.-2012 Apr.	D1.1, D3m.1
2	2013 Nov.-2014 Aug.	D1.1, D3m.2
3	2014 Nov.-2015 May	D1.1, D3m.2
3	2015 Jun.-2015 Jul.	D1.2, D3m.2
4	2015 Sep.-	D1.2, D3m.2

Table 2.4: Combination of D1 and D3m chambers per data taking period.

The acceptance size of each chamber has been adjusted with a Drell-Yan event simulation in order to be as sensitive as possible to the  $x_2$  range of interest. Particularly, the greater the acceptance width is, the higher the reach in  $x_2$  is. This makes the hit-rate tolerance of the chambers a key feature because the spectrometer is exposed to a large number of background particles, particularly near the edges where the desired  $x_2$  events occur. It is particularly significant for the most-upstream station (i.e. Station 1) which receives the highest hit rates. Experimental data shows that the rate tolerances are 3.0 MHz/wire at D1, 1.6 MHz/wire at D2 and 0.7 MHz/wire at D3 with a beam intensity of  $5 \times 10^{12}$  protons/spill. The gas-amplification gain should not be degraded under these hit rates.

For Run 2 and beyond, the gas mixture used for almost all the chambers is Argon:Methane:CF4 (88%:8%:4%) with a drift velocity of about  $20 \mu\text{m}/\text{ns}$ . A “fast gas” mixture used for D1.2 (upgraded D1) is Argon:CF4:Isobutane:Methylal (68%:16%:13%:3%) with a drift velocity of  $50 \mu\text{m}/\text{ns}$  and thereby a better hit-rate tolerance. This is “fast” in comparison to the  $\approx 20 \mu\text{m}/\text{ns}$  rest of the DCs. The spatial resolution of each plane is required to be  $400 \mu\text{m}$ , which corresponds to a momentum resolution of  $\Delta p/p = 0.03 \cdot p$  ( $\text{GeV}/c$ ). The resolution of dimuon invariant mass is dominated by the multiple scattering in FMAG; the chamber momentum resolution is about 10% of the total mass resolution at maximum.

The D1.1, D2, and D3m.1 chambers have been inherited from previous Drell-Yan experiments that have been conducted at Fermilab. Chambers D2 and D3m.1 have their origin in E-906 [26] and D1.1 is from SeaQuest’s direct predecessor, E-866/NuSea [21, 34]. Since these chambers have not been used for decades since E-866, they had to be refurbished by restringing  $\approx 30\%$  of their sense wires due to them being loose or broken. Newly supplied electronic readout boards were also mounted on these chambers.

The D3p and D3m.2 chambers were designed and constructed specifically for this experiment in order to cover the large acceptance required at Station 3. D3p was newly constructed by the TokyoTech SeaQuest collaborators and was shipped from Japan to Fermilab. The first part of data taking, Run 1, was carried out using D3m.1 while preparing for the construction of D3m.2. The newer D3m.2 is wider than D3m.1 by 25 cm at each side, allowing the high- $x_2$  statistics on  $\bar{d}/\bar{u}$  and  $Y_A/Y_{2H}$  to increase by  $\approx 20\%$  at  $x_2 \sim 0.3$  and  $\approx 10\%$  at  $x_2 \sim 0.4$ . The operational stability also improved, as D3m.1 suffered from frequent dead/noisy wires, HV trips, and leak currents. The D1.2 chamber was also designed and constructed for this experiment by the University of Colorado Boulder. As it is wider than D1.1 by 25 cm at each side and greater hit-rate tolerance, the anticipated statistics is expected in the high- $x_2$  region is expected to increase still more. It was installed in the experimental hall near the end of Run 3.

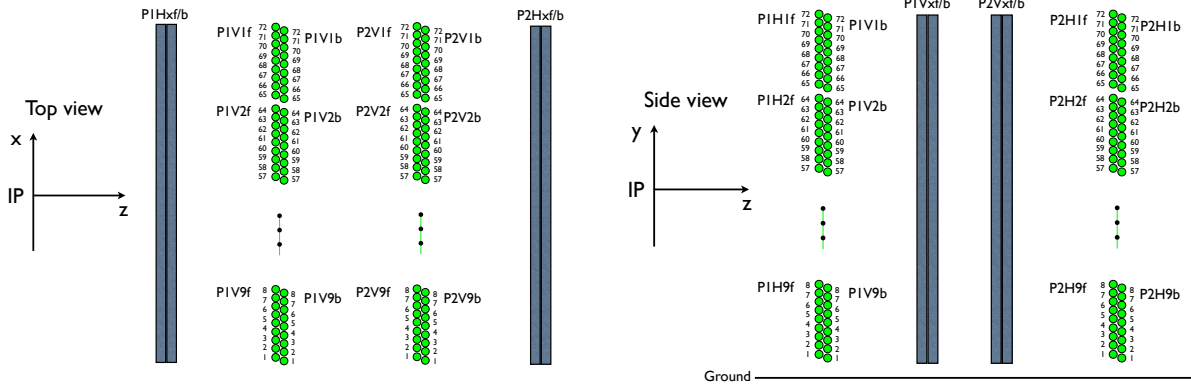


Figure 2.9: Proportional tube top ( $x-z$  plane) view. Figure 2.10: Proportional tube side ( $y-z$  plane) view.

### 2.7.3 Proportional Tubes

Downstream of Station 3 and the 1 m thick iron hadron absorber wall is Station 4 with its hodoscope planes and proportional tube detectors (prop tubes). At Station 4, the only beam-induced particles that remain that can leave tracks in an ionization detector are high energy muons. The prop tubes enable the task of muon particle identification (PID) for the experiment and consist of four planes. Each detector plane is made of 9 prop-tube modules, with each module assembled from 16 12-ft long 2" diameter prop-tubes staggered to form two sub-layers. The first and fourth planes are oriented along the horizontal direction (tubes parallel to the floor) to provide positional measurements in  $y$ , as shown in Fig. 2.9. The second and third planes are arranged vertically to measure  $x$ -position as shown in and Fig. 2.10.

Each plane of proportional tubes is composed of 9 *modules*, each having a set of 16 proportional tubes: 8 in line in a horizontal or vertical orientation and 8 more offset (“primed”) from the first 8 by 0.5 inches. This offset structure prevents any muons from going undetected between tubes and allows for left-right disambiguation for two hits in adjacent primed-unprimed sub-plane pairs in the same module. The modules are labeled 1–9 in increasing order from left to right for the  $x$ —measuring planes and from 1–9 in increasing order from top to bottom. So, the top module of the first vertical plane of prop tubes is P2H1. Additionally, in each module, the primed and unprimed sub-planes are referred to as *f* for “front” (facing upstream) and *b* for “back” (facing downstream). This substructure can be seen in detail on Fig. 2.9 and Fig. 2.10.

A single prop tube is made of 2-inch diameter aluminum tubes with a wall thickness of 1/16 inches. The central anode wire is a gold-plated 20 $\mu\text{m}$  diameter tungsten wire kept at approximately 1.95 kV. Considering the staggered nature of each plane’s substructure, one can in principle achieve a spatial resolution of 0.3mm. During Runs 2 and 3 of data taking, a resolution of 0.5mm for high energy muons was observed, which is

more than sufficient for muon identification purpose. The gas mixture for prop-tubes is P-10 (Ar:Methane = 90:10) mixed with a 10% CF<sub>4</sub> gas (Ar:CO<sub>2</sub>:CF<sub>4</sub> = 70:20:10) which yields the maximum drift time about 400ns. With this maximum, the prop tubes can handle a singles rate up to 2MHz while normal operational hit rates are typically below 1MHz.

A typical desired high-energy muon within spectrometer acceptance will traverse through two prop-tubes in each plane and induces hit signals on two anode wires. The path of a track is reconstructed from the drift time measured on the two anode output, with a custom TDC board that provides 0.44 ns timing resolution. With the hit information reconstructed from readouts of the forward and backward planes in  $x - z$  and  $y - z$  direction, precise reconstruction of the track trajectories can be obtained. Ideally, 8 hits from the 4 planes are used to form a track pointing back to the target. If such is the case, a candidate muon track is successfully identified.

Detector Plane	Number of modules	# tubes per module	Width ( $x$ ) $\times$ height ( $y$ ) [cm] $\times$ [cm]	$z$ -position of front (back) sub-plane [cm]
P1H	9	16	368 $\times$ 368	2,099 (+4)
P1V	9	16	368 $\times$ 368	2,175 (+4)
P2V	9	16	368 $\times$ 368	2,367 (+4)
P2H	9	16	368 $\times$ 368	2,389 (+4)

Table 2.5: Parameters of the four proportional tube planes.

#### 2.7.4 Mass Resolution from Chamber Resolution

The mass resolution of the spectrometer is, in part, limited by the resolution of the tracking chambers and the distances between them. For an arbitrary set of hit positions in Stations 1, 2, and 3 ( $r_1, r_2, r_3$ ) which are separated from each other in  $z$  by distances  $z_{12}$  and  $z_{23}$ , with KMAG in between Stations 1 and 2 supplying a  $P_{kick}$ , one can derive  $\Delta P/P$ . A line, or track segment, is first reconstructed between  $r_2$  and  $r_3$ . The slope (and its uncertainty) of this track segment in the  $z - x$  plane is:

$$s_{23} = \frac{r_3 - r_2}{z_{23}} , \quad \Delta s_{23} = \frac{1}{z_{23}} \sqrt{\Delta r_3^2 + \Delta r_2^2} \quad (2.3)$$

The values of  $\Delta r_n$  here are the position resolutions of the individual tracking chambers at each Station. One can use this slope to project a trajectory through KMAG and onto Station 1. The momentum is calculated by seeing where the actual hit position is in Station 1 and looking to the distance ( $d$ ) between where the particle hit the station and where it would have hit had KMAG's magnetic field not existed. This is called a *sagitta analysis*, as the magnetic field moves the particle's trajectory as if along a circle, and we are looking

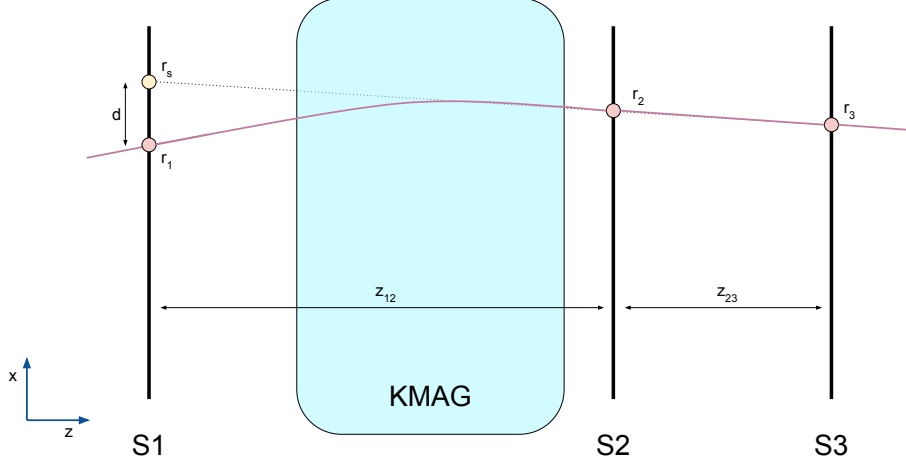


Figure 2.11: A simplistic depiction of a track passing through from Station 1, through KMAG where its path is bent by the magnetic field, and then straight on through Stations 2 and 3.

to the particle's path along the sagitta of that circle. Ultimately, the momentum uncertainty is related to this distance as:

$$\frac{\Delta P}{P} = \frac{P}{P_{kick}} \Delta d \quad (2.4)$$

The expected sagitta point ( $r_s$ ) is located at:

$$r_s = s_{23}z_{12} + r_2 \quad (2.5)$$

$$\Delta r_s = \sqrt{\Delta s_{23}^2 z_{12}^2 + \Delta r_2^2} = \sqrt{\Delta r_3^2 \left(\frac{z_{12}}{z_{23}}\right)^2 + (1 + \left(\frac{z_{12}}{z_{23}}\right)^2) \Delta r_2^2} \quad (2.6)$$

And the distance,  $d$  follows as:

$$d = r_s - r_1 \quad (2.7)$$

$$\Delta d = \sqrt{\Delta r_s^2 + \Delta r_1^2} = \sqrt{\Delta r_3^2 \left(\frac{z_{12}}{z_{23}}\right)^2 + (1 + \left(\frac{z_{12}}{z_{23}}\right)^2) \Delta r_2^2 + \Delta r_1^2} \quad (2.8)$$

The momentum resolution due to chamber resolution can therefore be described as:

$$\frac{\Delta P}{P} = \frac{P}{P_{kick}} \sqrt{\Delta r_3^2 \left(\frac{z_{12}}{z_{23}}\right)^2 + \left(1 + \left(\frac{z_{12}}{z_{23}}\right)^2\right) \Delta r_2^2 + \Delta r_1^2} \quad (2.9)$$

The dependence of the resolution on  $P/P_{kick}$  works such that the larger the  $P_{kick}$  is (w.r.t. particle momentum  $P$ ), the more the track is bent, and the more precisely the original momentum is defined. Besides

chamber resolution, other contributions to this momentum resolution are from multiple scattering through FMAG’s iron beam dump and from the spectrometer’s angular resolution. These will be discussed elsewhere in this paper.

The mass resolution is linked to momentum resolution via the following relation

$$\frac{\Delta M}{M} = \frac{\Delta P}{2P} \quad (2.10)$$

The factor of two arises from the fact that the Drell-Yan dilepton mass comes from two independent muons with the same momentum resolution. This mass resolution is important because it, in turn, contributes to the  $\Delta x_2/x_2$  resolution, which is the key dependent variable for SeaQuest measurements.

$$\frac{\Delta x_2}{x_2} \approx 0.57\Delta x_F + 0.012M^2 \frac{\Delta M}{M} \quad (2.11)$$

## 2.8 Trigger

The SeaQuest Trigger System is designed to quickly select candidate dimuon events from the high-rate, high-background environment using discriminated hodoscope signals.

### 2.8.1 Design Requirements

The trigger must select events of interest to the main physics goals with good enough efficiency (maximum signal-to-background ratio) to facilitate high-statistics analyses. In general, it is optimized to accept high-mass (4 – 10 GeV) dimuons originating from the targets and beam dump. The event selection is also designed to intentionally reduce acceptance of dimuons from other, higher-rate sources, such as  $J/\Psi$  decays and non-Drell-Yan dimuons originating from the beam-dump, though enough  $J/\Psi$  events are triggered on to allow high-statistics analysis of  $J/\Psi$  physics. Other goals of the trigger design are to keep the triggering rate low enough to maintain an acceptable DAQ livetime and to keep the trigger’s internal throughput deadtime-free. By design, there should be no bottleneck at this stage, and the trigger should be capable of firing on any and all RF-buckets while the DAQ is live.

The hardware, firmware, and design should be sufficiently flexible to quickly accommodate changes in the spectrometer, beam conditions, and physics goals. Any changes to the geometric acceptance of the spectrometer, such as new/moved detectors or changes in the magnetic fields must be immediately reflected in the trigger selection in order to maintain high signal efficiency and good background rejection power. Similarly, a change in the beam duty factor or intensity should be accompanied by a change in the event

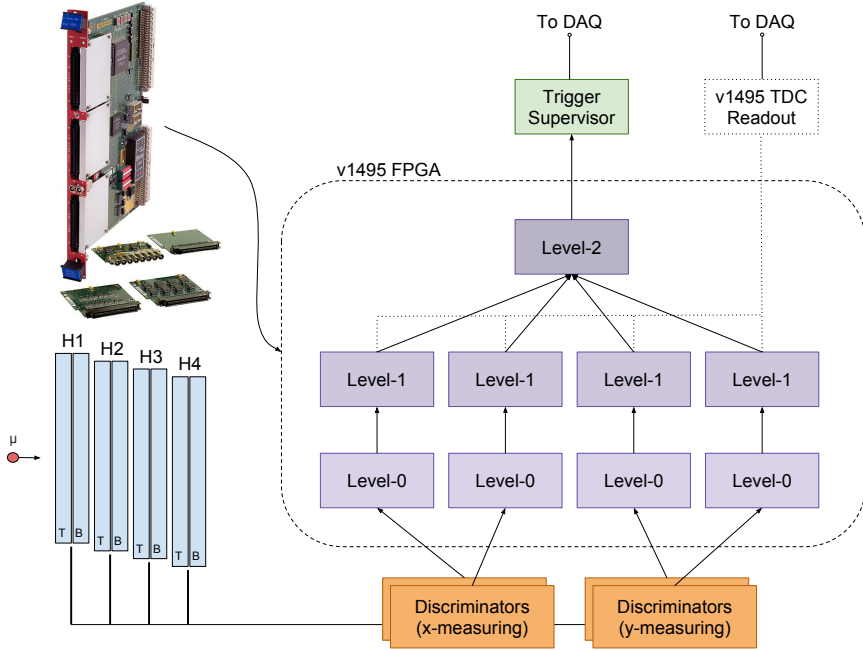


Figure 2.12: The trigger system at SeaQuest is composed of 9 CAEN v1495 FPGA modules. These modules output a trigger signal to the Trigger Supervisor, which tells the DAQ when to record data.

selection, ensuring trigger rate optimization and zero internal deadtime. Finally, the trigger should be capable of specific modifications to facilitate special runs for other physics goals. For these reasons, the design of the trigger system underscores a significant need for flexibility in its hardware and design.

Lastly, the design of the trigger system should include self-diagnostic capabilities, allowing for constant monitoring of the trigger system's performance. Internal pulser-testing is employed to test the function of each compiled firmware every time the trigger logic changes. For added transparency, data from the internal TDC's is used by online and offline software to monitor the self-consistency of the trigger for each recorded physics event.

### 2.8.2 Trigger Hardware

The triggering system, which is depicted in Fig. 2.12, begins with the Stations 1-4 hodoscope arrays. Hodoscopes are used for this task as the time resolution and high speed is limited only by the speed of light through the scintillator paddles and secondary emission of electrons (through the stages of the PMTs. This occurs over the span of nanoseconds, which allows for fast triggering on RF buckets that occur every 19ns during spills. The hodoscope planes - both x- and y-measuring planes - are separated into top and bottom sections as far as triggering is concerned. The signals from the hodoscope arrays are passed through a set

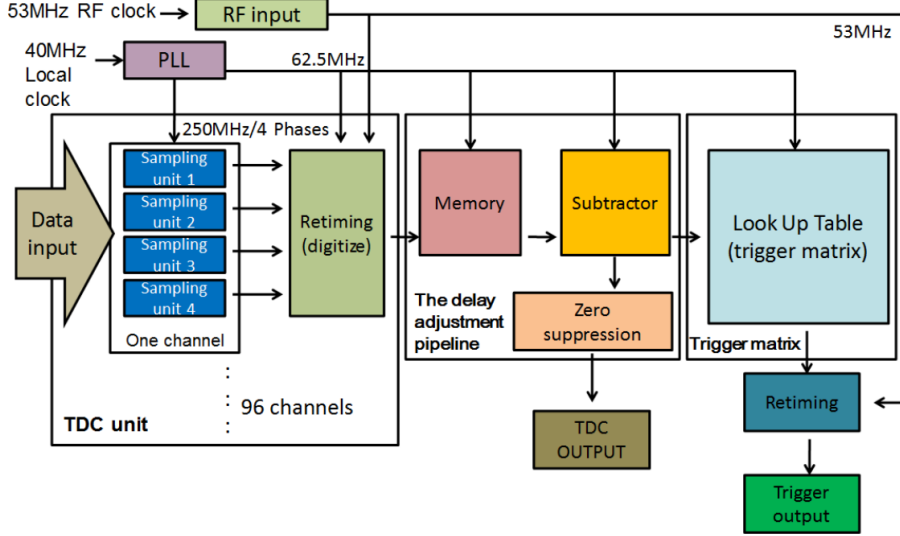


Figure 2.13: A block diagram of the major functions of the v1495 FPGA [32].

of discriminator modules, which will only pass a signal on to the rest of the trigger if there is enough of a signal from the PMT's past a preset threshold.

The output of the discriminators is passed along to one of the nine CAEN v1495 FPGA (Field Programmable Gate Arrays) VMEbus (Versa Module Europa) modules [9]. This hardware trigger consists of a single decision stage with a three-step parallel pipeline. These steps are referred to as the *level-0*, *level-1*, and *level-2* stage triggers. The detailed internal flowchart of the CAEN v1495 electronics can be seen in Fig. 2.13.

At the first step, level-0, there is nothing actively performed during nominal data taking. The signal is passed on through, unaltered, to level-1. As it stands, level-0 is not used for any of the triggering modes. This stage is, however, extensively used for the pulser testing and self-diagnostic purposes. The level-0 stage is capable of being programmed to pulse arbitrary patterns on to the level-1 stage, which is very useful for observing how level-1 (and subsequently, level-2) will behave in a controlled setting. Whenever a new firmware is installed on the v1495, a pulser test is performed to ensure that all design requirements are met before uploading the firmware for production data taking.

The next level-1 trigger records the hit signals from the x- and y-measuring hodoscope hits split into top and bottom partitions with respect to their location in the SeaQuest spectrometer. The hit patterns are tested via a lookup table against a preselected set of hodoscope hit patterns, or “*trigger roads*”. Each trigger road corresponds to a set of four hodoscopes: one from each station, with all being in the top or bottom half of the spectrometer. In this lookup table, there is a charge and approximate  $p_T$  value for each preselected road. These are known via studies of Monte Carlo studies of muon paths from di- or single-muon

events originating from the targets or beam dump. The roads were selected such that as many good dimuons are selected while reducing roads that are dominated by background signal that might cause trigger and/or DAQ deadtime.

During data taking, only the x-measuring hodoscopes were used for the v1495 trigger. As such, the two level-1 stages that look to the y-measuring hodoscope signals were unused. The level-1 trigger logic identifies four-out-of-four X1-X2-X3-X4 coincidences, which are characteristic of high  $p_T$  single muons produced from the targets or beam dump. Each time a candidate coincidence that satisfies a preselected road is found, the level-1 step outputs certain logical bits indicating the track's charge, detector half (top or bottom), and  $p_T$  bin.

The third step of the triggering logic is the level-2 trigger, or the “*Track Correlator*” stage. This step takes the outputs of level-1 (charge, detector half,  $p_T$  bin) and finds if any combinations satisfy any of the preprogrammed triggering modes. If one of these modes was satisfied, a signal is sent to the Trigger Supervisor (TS) module that communicates with the DAQ system to record an event at a specific synchronized RF bucket.

### 2.8.3 Triggering Modes

The v1495 FPGA had five configurable sets of physics triggers were used in the trigger system for the majority of production-level data taking. These five are referred to interchangeably as “Matrix” and “FPGA” triggers, followed by the number 1-5 indicating which of the five. These modes are described in detail in Table 2.6.

Trigger	Condition	Sign	# $\mu$	Prescale
FPGA-1	$T \wedge B$	Opposite	2	1
FPGA-2	$(T \wedge T) \vee (B \wedge B)$	Opposite	2	1000
FPGA-3	$T \wedge B$	Same	2	123
FPGA-4	$T \vee B$ , all $p_T$	+ $\vee$ -	1	30000
FPGA-5	$T \vee B$ , $p_T > 3\text{GeV}$	+ $\vee$ -	1	2000
NIM-1	Y-coincidence	NA	NA	30000
NIM-2	X-coincidence	NA	NA	1000
NIM-3	Random RF	NA	NA	1000

Table 2.6: Trigger settings for Run 3 and beyond. Prescale figures shown are typical values and were adjusted as experimental needs were tuned. NIM-1 and NIM-2 triggers’ exact conditions could be changed and reconfigured from the counting room.

Different trigger settings were used for capturing data for different purposes. The primary triggering mode is FPGA-1, which looked for a combination of two roads of opposite sign that reside in opposite halves of the spectrometer. The FPGA-2 looked for good muon pairs that occurred in the same half. This, however, turned out to have a combinatoric problem that had two adverse effects: track reconstruction

was difficult for these types of events, and the trigger fired off too often, causing high trigger and DAQ deadtime. As such, FPGA-2 was disabled for much of data taking. FPGA-3 trigger looked for the same kind of signal as FPGA-1, but with same-sign muon pairs. This type of event is useful for analyzing the experiment’s combinatoric background. FPGA-4 and -5 are “singles” triggers that record events that are useful for estimating backgrounds and detector efficiencies. Each of these has a “*prescale factor*” that limits how many of each mode actually fires the trigger. For example, FPGA-3 has a prescale factor of 123, which means that, within a single spill, there must be 123 FPGA-3 events before it tells the DAQ to record one. This keeps certain high-frequency trigger modes from dominating the readout and causing undue deadtimes.

In addition to the v1495 FPGA triggering mechanism, the outputs of the hodoscope discriminators are also sent up to the control room to a set of NIM logic modules. These signals, however, do not describe each hodoscope paddle but instead are *ANDs* of the tops and bottoms of each plane. For example, if one or more paddles in H1T fires, then a positive signal is sent out indicating that H1T fired. These signals can be used to form a rudimentary trigger on situations such as 4- or 3-out-of-4 coincidences in the X- or Y-direction hodoscope planes. In general, NIM-1 is used for Y-coincidences, and NIM-2 is used for X-coincidences.

The third NIM trigger mode is of particular importance, as it is used for estimating a great deal regarding backgrounds and rate dependence issues. The NIM-3 trigger is called the “Random RF” trigger, as it is controlled by two different clocks beating against each other. When the two clocks are in coincidence, they will send a signal to the Trigger Supervisor to record the event corresponding to the next immediate RF bucket. This trigger allows the experiment to get a random sample of the events that are occurring at the spectrometer, notably without a bias that a selective trigger can incur.

## 2.9 Data Acquisition Systems

The whole of the SeaQuest experiment spans two sectors of the NM beamline (NM3 and NM4) and records not only detector data but also accelerator and atmospheric conditions. Designing a data acquisition (DAQ) for this experiment, therefore, requires a bandwidth and timing which cannot be provided by a single central computer system. SeaQuest has therefore employed four separate DAQ subsystems called “Main DAQ”, “Scaler DAQ”, “Beam DAQ” and “Slow Control”. The Main DAQ records the main detector information and the trigger timing. Scaler DAQ records various scaler readouts once per spill to reduce bias from the dead time of Main DAQ. Beam DAQ records information from a beamline Čerenkov detector read out by its QIE board. The Slow Control is a catch-all for everything else, from magnet current to radiation monitors that are read out once per spill.

### 2.9.1 Main DAQ

The MainDAQ is powered by a Jefferson Lab developed software package named CODA (CEBAF<sup>1</sup> On-line Data Acquisition). The Trigger Supervisor could receive up to 12 different kinds of triggers. The first four triggers (FPGA 1-4) can be prescaled up to 24 bits. The second four triggers (FPGA 5, NIM 1-3) can be prescaled up to 16 bits. The rest of triggers (NIM4, flush trigger, Beginning of Spill (BOS), End of Spill (EOS)) are not prescalable. The Main DAQ can configure which triggers are enabled at the Trigger Supervisor level and what the prescale factors are for each triggering mode. Once the TS receives a trigger, it will count the prescale factor and, based on how many triggers of that type have fired so far, it will decide if the Main DAQ will accept the trigger or not.

Once the TS accepts the trigger, it sends an “accepted trigger” signal to the other front end electronics, such as the detectors’ TDC readouts. Facilitating intercommunications, the Main DAQ system is connected to the TS and the CPU’s in the VME crates via a local network. These CPU’s are known colloquially at SeaQuest as readout controllers, or “ROC’s”. The TS connects with each VME crate, and when the TS sends an “accepted trigger”, an interrupt signal is sent to each of the ROC’s. The ROC’s will then start reading the various front-end electronics (FEE).

The TS also sends a signal to the QIE of the BIM, and the QIE retains information regarding the  $\pm 16$  RF buckets around that triggered RF bucket to assist in investigating the beam quality around each of our event triggers. The output of the QIE is encoded into a scaler latch card format. If the beam intensity in RF buckets neighboring the trigger is higher than the user-select threshold, then the board will issue a veto signal to the TS to ignore this trigger.

The Main DAQ’s deadtime is considerable, as it has to communicate with the TDC’s, which have the longest copy-in-progress time of  $32\ \mu s$ . The average TDC readout time is approximately  $300\ ns$  per 32bits (one hit), and as such, the slowest ROC which contains 7 TDCs has, on average,  $150\ \mu s$  deadtime. This deadtime is accounted for under the umbrella term of “*busy*” time and factored into the calculation of the “live protons” received by the experiment.

### 2.9.2 Scaler DAQ

The Scaler DAQ is used to ensure that the detector and trigger systems are working properly. The readout controller CPU is an MVME5500 [27] with four scalers. One of these scalers is triggered by the coincidence of a  $7.5\ kHz$  gate generator and the beam spill signal. This records the  $7.5\ kHz$  response of the hodoscope arrays. The other three scalers are triggered by the BOS or EOS signals and thus record spill-level rates.

---

<sup>1</sup>The old acronym inside of an acronym bit. CEBAF: Continuous Electron Beam Accelerator Facility

Data collected by these spill-level scalers are the number of times each Main DAQ trigger is satisfied (both raw and accepted), the intensity of the beam, and the rates of the hodoscope arrays. The readout of this VMEbus DAQ is done using CODA very similarly to the Main DAQ but on a completely different system. An independent program analyzes the data in real-time in order to monitor the performance of the detectors and triggers, as well as the quality of the beam.

### 2.9.3 Beam DAQ

The Beam DAQ is composed of a Čerenkov detector in the proton beam (the Beam Intensity Monitor discussed earlier in this chapter), a QIE board, and a custom C++ program to control their operation and read out. The Beam DAQ is responsible for recording the 53 MHz structure of the beam, i.e. the intensity of each RF bucket. Its calculation of the 53 MHz duty factor  $DF = \frac{\langle I \rangle^2}{\langle I^2 \rangle}$  is the primary measure of beam quality that accelerator operators use for tuning. In short, the duty factor is a measure of the *uniformity* of the intensity of the beam. If we were to ignore the buckets intentionally left empty, and if it were to be the case that every RF bucket had the same number of protons, the 53 MHz duty factor would be 100%.

There four types of data recorded by the QIE have already been covered in the Beam Intensity Monitor section: QIESum, beam inhibit, busy time, and the  $\pm 16$  RF bucket intensities. The Beam DAQ commences read out of each of these blocks of data when the EOS signal is seen. The block of QIE data for all buckets is about 300 MB. To read this much data in time to analyze it and be ready for the next spill, the DAQ program utilizes multithreaded processes. Three threads are used to read the data from the QIE board's three ethernet chips, and up to eight threads are used to analyze the data. Analyzed data is displayed on a public webpage so that shifters and accelerator operators can monitor the quality of the beam (Fig. 2.14). The fully processed data is also written out to tab-delimited ASCII files, which are archived and also uploaded to our online MySQL server.

### 2.9.4 Slow Control Readout

The Slow Control readout system is an aggregation of many different readouts from various parts of the experiment. This is also the umbrella term for other critical monitoring and bookkeeping tasks that must be performed. The one common thread to them all is that they only *need* to be read out / performed once per spill in order to give perspective on the conditions of the experiment for each given spill. The term “Slow” in Slow Control is adapted from the term “Slow Spill”, which is used to characterize the method of beam delivery to SeaQuest. The Slow Control is run by an array of Python, Perl, and Bash scripts that, for the most part, run independently. These scripts primarily interact with and read out from EPICS, ACNET,

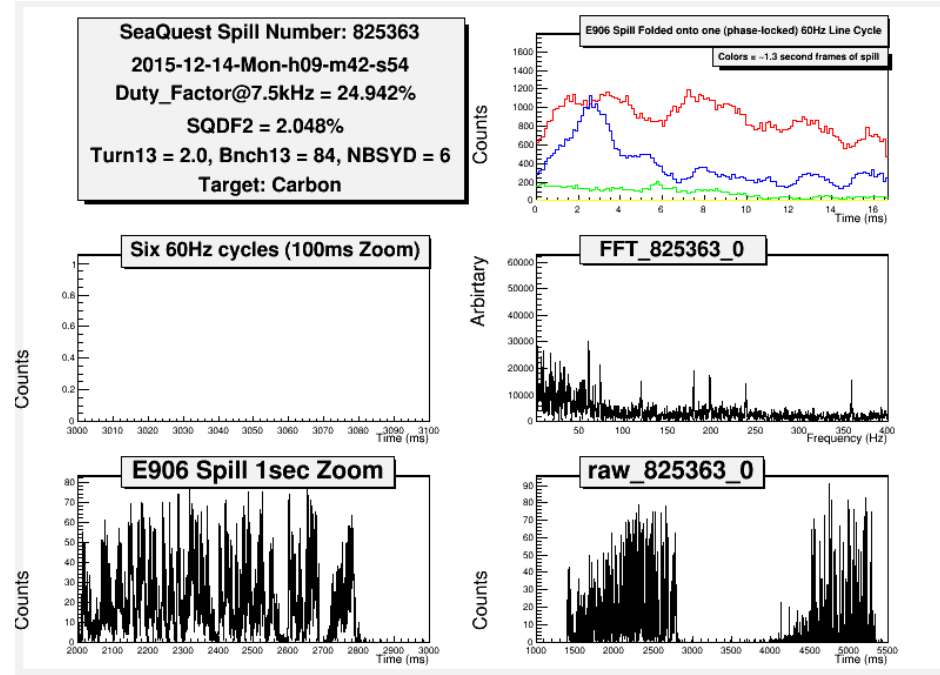


Figure 2.14: A standard Beam DAQ display showing beam characteristics and spill data. The bottom two plots show the output of the QIE on a ms scale.

and the local Spill Counter.

### EPICS, ACNET, and Kiethley

The EPICS software package (Experimental Physics and Industrial Control System) is used for communicating any number of variables across the experiment's local network. EPICS is used for feeding readouts from many different sources and formats, and making them available to any other system that may have need of certain information, but does not natively communicate with a different system's format. Bridging this gap, EPICS is able to gather information regarding the target, beam, and environmental data into one place.

The EPICS server is installed on SeaQuest's target control computer, where the target position, pressures, temperatures, and proximity sensors are monitored and controlled. These values are critical to track and monitor, as they affect what target is in position at any given spill, along with information that may infer the cryogenic liquid targets' densities. Additionally, there is information regarding the operational mode of the target table, such as whether or not the target table is being manually controlled or if it is automatically repositioning itself. In Slow Control parlance, information from the target computer that is sent to the EPICS server is labeled as "Target" type data.

Several values are read into the EPICS server from the Accelerator Network (ACNET), which monitors

many critical systems. Beam intensities (S:G2SEM) and FMAG / KMAG currents are two of the major factors that must be factored in for any analysis. There are additional readouts with esoteric names that can record anything from beam pipe vacuum to upstream radiation monitors. It is important to note that the FMAG and KMAG variables from ACNET are read out to the EPICS server every 3 s, particularly because it is unsafe to deliver beam to the sensitive detectors without FMAG being fully powered. As such, the FMAG current is read into the beam interlock system. In the Slow Control feed, this type of information is labeled as “Beam” data.

Finally, there is a Keithley multimeter [\[citation needed\]](#)in SeaQuest Hall near the electronics racks by Station 3. This device has the responsibility of relaying information regarding ambient temperature, air pressure, and humidity up to the control room. This information on its own is not typically used for any analyses, but in the case that, for example, a rise in humidity results in any electrical device failures, the monitoring data exists to diagnose it as such. This data is gathered by a ‘kscan’ program that is run on the target machine, and its operation typically takes 11s to return a result. Data from the Keithley multimeter that is put into the Slow Control feed is labeled as “Environment” data.

## Spill Counter

Perhaps one of the most critical components of the data acquisition is the coordination between the many sources of data in the DAQ. The Main DAQ, Scaler DAQ, Beam DAQ, and Slow Control do not share a single clock or network, so some measures need to be taken to ensure that data from different sources regarding a single spill’s worth of data actually all correspond to the same spill. The concept of a locally maintained Spill Counter arose as a solution to this problem, and it is handled in the form of a simple Python script and a flat text file containing a single integer.

The enacted solution begins with placing an initialized spill counter ( $spillID$ ) value (currently  $O(10^5)$ ) into an otherwise empty text file at a specified location. Then, when the ACNET readout receives a BOS/EOS signal from AD, a simple python script performs the following:

- Read the current spillID from the file
- Broadcast this value over the EPICS server
- Insert a single ASCII-encoded event into the Main DAQ and Scaler DAQ CODA streams containing only that spillID number
- Waits for 20 s while other scripts may want to use the current spillID value to connect its value to the spill that just ended

- Updates the file to contain spillID + 1

This simple approach has been very effective in its usage so far, and the spillID incremented via this method has been shown to be accurate upon scrutiny of data contents across DAQs. This can be easily done by looking at a series of full and empty spills, as it is obvious which spills had a nominal beam spill and which did not by investigating the output of each DAQ. The weakness lies in the fact that this system relies on a single file, which is susceptible to any number of file access and timing issues. At some point in the future, it would be advisable to have all spillID-using systems to read the current value from the broadcasted EPICS server value instead of having several applications attempting to access and read the single file (even if just read-only).

### **Python Slow Control Script**

With all of this going on to aggregate data from several sources, there is one final script that takes this aggregated data and makes it readily available for the rest of the DAQ systems. A `read_slowcontrol.py` script, once every 60 s supercycle, puts the following together into a single ASCII text file:

- Clock time (“vxticks”) of the Trigger Supervisor
- Spill count data
- Beam data
- Environmental data
- Target data
- Timestamp

Once all of this is written to a file, this is sent to the Main DAQ and Scaler DAQ to be integrated into the full CODA file as a plain text event with a simple, tab-delimited format.

# Chapter 3

# Photomultiplier Tube Base Upgrade

## *CHAPTER STATUS: FIRST DRAFT COMPLETE*

During Run I of SeaQuest, observations of hodoscope wire maps (as in Fig. 3.1) suggested an apparent drop in expected performance in the  $y$ -measuring hodoscopes. While this performance was most obviously seen in the  $y$ -measuring hodoscope planes, the  $x$ -measuring planes were likely also affected. This effect was assumed to be due to high-intensity RF buckets that caused very high multiplicity in all of the detectors in the spectrometer for that event. The result of these intense events seemed to push the PMTs and/or their PMT base electronics past their operational capacity.

The understood cause of this “*sag*” in performance, as it came to be called, was due to a destabilization in the voltage divider in the PMT base. This critical component holds each dynode stage at a specific voltage, and when this destabilizes and is unable to maintain an appropriate voltage difference between dynode stages, inefficient performance of the PMT results.

During the Fall of 2012, prototyping and testing were performed with the goal in mind being to assemble a new base for the Philips XP-2008 PMTs [29] and compare its performance to the original PMT base and to some modern, high-performance Hamamatsu PMTs. Once a base design tested well, the new bases would be manufactured and installed in the existing frames of the original PMT bases.

## 3.1 PMT Basic Construction and Operation

Figure 3.2 shows a schematic design of a typical photomultiplier tube and base setup. It consists of a photocathode that is followed by an electron multiplier section (or dynode string) then an anode from which a final signal is delivered. During operation, a high voltage is applied to the photocathode, dynodes, and anode in such a way that there’s a potential “ladder” going from stage to stage. When an incident photon from the hodoscope scintillator paddle hits the photocathode, an electron is emitted via the photoelectric effect. The voltage difference between the cathode and dynode stages draws the emitted electron to the dynodes, and each time an electron hits a dynode, some of that electron’s energy is transferred to other

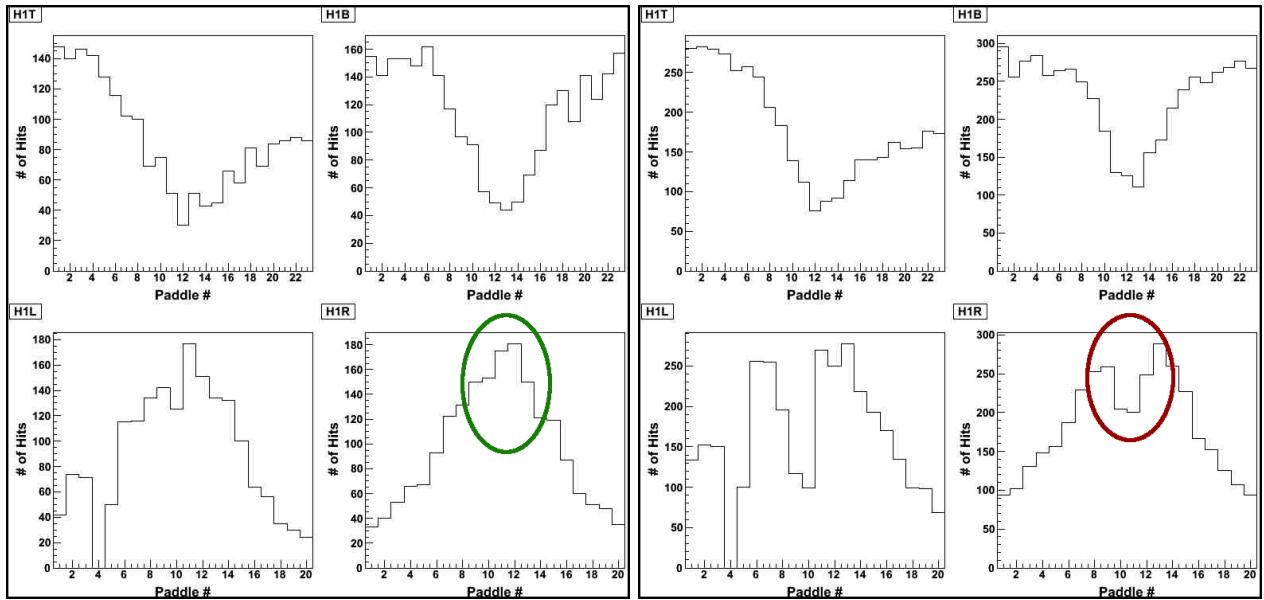


Figure 3.1: (Left) Histogram of hodoscope ‘hits’ in a typical event; (Right) Histogram of high-intensity event, with marked sagging most noticeably in the middle of the y-measuring hodoscopes

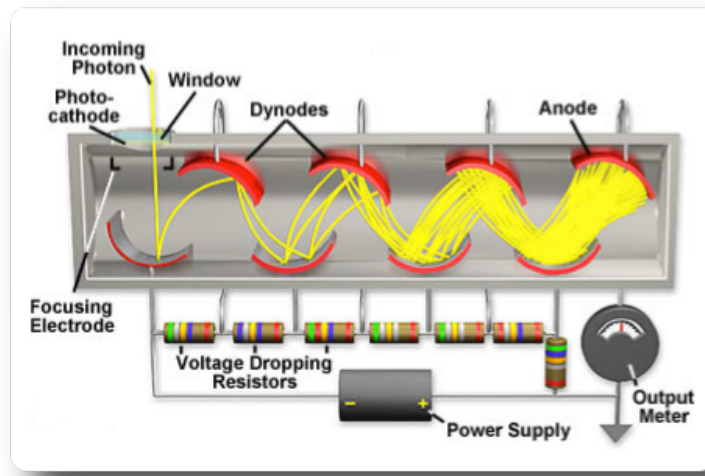


Figure 3.2: A diagram of typical PMT operation. The circuit controlling the voltage-dropping resistors is the part that was upgraded in this chapter.

electrons in the dynode. These electrons then are emitted and become accelerated towards the next dynode stage. This process is called secondary emission, and by the time the process is repeated, there is a cascade or avalanche of electrons that land on the anode, resulting in a signal that can be amplified and analyzed.

It is the case that the voltage divider ultimately supplies the electrons that are emitted in this signal cascade. If too many photons and resultant electron cascades occur, the dynode stages' voltage divider will destabilize as they attempt to resupply the dynode stages with electrons. The problem that was experienced at SeaQuest was that these high-intensity events were flooding the PMTs with photons, causing this "saturation" which caused this destabilization and the inefficient performance that was observed. The goal specifically was to test out modern base designs that provided for added stability to the performance of the voltage divider, even under high rates.

In general, each base divides around a -1500 V potential total over the photocathode (K), ten dynode stages (D1-D10), and the anode (A). There are two currents that are referred to here:

- Signal Current: This is the signal that passes over the anode, which is the end-result of the cascading secondary emission electrons from each dynode stage.
- Bleeder Current: This is the current through the voltage divider. It is termed the "bleeder" current since the compounding electrons in the signal current must be "bled" from the current through the voltage divider.

Throughout these voltage base designs, capacitors are commonly implemented in the latter dynode stages where the most electrons are emitted. These capacitors, when charged, are able to replenish the lost charge on its corresponding dynode stage in the event that an intense light pulse induces a large signal current. As the capacitor is able to hold its own charge, this resupply can occur without requiring the charges to be drawn from the bleeder current, thereby keeping the voltage across the dynode stages more stable.

## 3.2 PMT Base Design Iterations

There were several iterations of base design to determine which was best to approach for full base production and installation at SeaQuest. The core addition was the inclusion of transistors between dynode stages, according to the improvements suggested by C.R. Kerns in his paper regarding high-rate PMT bases [22]. Common solutions to destabilization in PMT bases have been to have (1) very large capacitor banks with charges  $> 10^3$  times greater than the time-averaged dynode current and/or (2) miniature on-board,separately-powered Cockcroft-Walton power supplies for the final dynode stages. A Kerns-style

transistorized base allows for a light-weight, small size, and simple base that does not require extra power supplies or voluminous energy storage capacitors.

In general, there are three important features that were tuned in this set of prototypes that affected the performance of the phototubes:

- Lower resistance
- Transistors (with protective diodes)
- Higher capacitance between dynode stages
- Distribution of voltage division

The lower overall resistance of the voltage divider increases the bleeder current. This means that the base will be more capable of handling high-intensity, as it will be better able to replenish the charges on each dynode stage in the case of a large signal. Typically, the larger the bleeder current, the larger the signal current can be without destabilizing the voltage divider. Higher rates usually put higher demand on the signal current, so by reducing the overall resistance, one can easily increase the rate capability. The shortfall here is that with voltage constant and resistance decreased, according to Ohm's Law ( $V = IR$ ), the current will increase. As a result, the power dissipated by the circuit ( $P = I^2R$ ) will go as  $I^2$ , and the PMT base may heat up to critical temperatures faster than it can dissipate the heat as there is no significant ventilation in the PMT base enclosure. The Philips XP-2008 manual quotes that for continuous usage and storage the ambient temperature should not exceed  $50^\circ C$  ( $122^\circ F$ ). In addition to heat concerns, there's typically a power rating for the class of small on-board resistors that were planned to be used. Approaching or exceeding that power limit would run the risk of burning out a resistor and rendering the base inoperable.

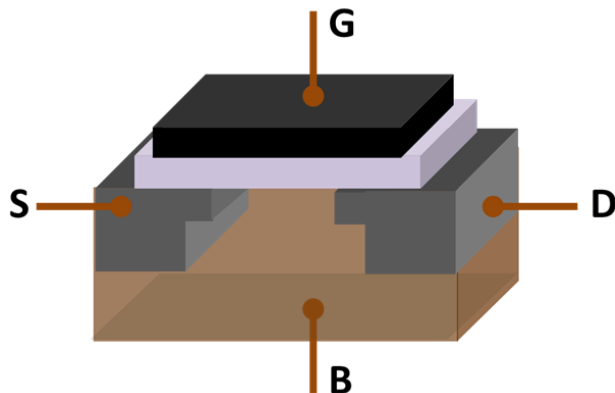


Figure 3.3: MOSFET showing gate (G), body (B), source (S) and drain (D) terminals. The gate is separated from the body by an insulating layer (white) [28]

Metaloxidesemiconductor field-effect transistors (MOSFETs) are introduced here to maintain the proper voltage division. In general, MOSFET transistors have an *source*, a *drain*, and a *gate*, where current flows freely through from the source to the drain, gate permitting (Fig. 3.3). If at any point a certain voltage across the gate of the transistor is not supplied (here, the voltage across dynode stages), then the source-to-drain current through the transistor is stopped until the proper gate voltage is restored. This helps greatly to “intelligently” regulate the voltage across the dynodes. Wherever transistors are used, diodes are also implemented to prevent the unlikely case of a current moving across the transistors’ gate in the wrong direction. This protects the transistors from being damaged particularly when powering the circuit on and off.

Having capacitors along the higher dynode stages allows for a quick resupply of charges to the dynodes, thus maintaining proper voltage division. This, however, is only a stop-gap measure and is only effective under cases of high instantaneous currents. It is the case that, should there be a constant too-high rate of operation, the capacitors will not be able to recharge themselves. Typical recharge time for the capacitors discussed in this section can range from 0.1-1 ms.

Finally, the specific division of voltage across each stage, from D1 to A, has an influence on the behavior of the PMT operation. As we see from the operations manual of the phototube in Fig. 3.4, in the case of a progressively increasing voltage division, there is a good compromise between timing and linearity. With respect to phototube operation, “linearity” is the quality that the amount of charge deposited on the anode is linearly proportional to the energy of the incident photon. “Timing”, on the other hand, is the quality that the time it takes for a high-energy photon signal and a low-energy photon signal to progress through the stages should be the same. For the purpose of optimization at SeaQuest, we wish to optimize the amount of signal (i.e. amplification or *gain*) that the phototube can accommodate. For this, the recommended voltage partitioning is flat from D1-A [29].

It should be noted that the prototype iterations of PMT base design changes were not intended to cover the entire phase space of these tunable parameters. The purpose of these tests was to get a sense of how changing one or more of these parameters could affect the PMT high-rate capabilities. The decision for a final base design had to be decided on with relative speed to get them manufactured, built, and installed before Run II of the experiment. As such, true optimization of all parameters could not be achieved within the scope of these tests.

### Recommended voltage divider

#### Type A for maximum gain

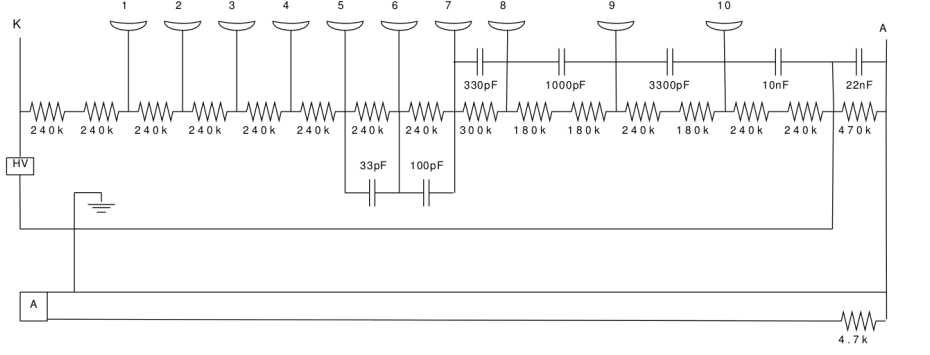
K	D1	D2	D3	D4	D5	D6	D7	D8	D9	D10	A	(total :12)
2	1	1	1	1	1	1	1	1	1	1		

#### Type B for bets timing / linearity compromise

K	D1	D2	D3	D4	D5	D6	D7	D8	D9	D10	A	(total :18.25)
2	1	1	1	1.25	1.25	1.5	2.25	2.25	2.5	2.25		

K: photocathode      Dn: dynode      A: anode

Figure 3.4: Suggested voltage division schemes for gain vs. timing/linearity compromise [29].



NOTES: Ground of the HV supply to the ground of the anode output separated, where they were connected with the 22nF capacitor and 470k resistor in parallel, in order to

- I) keep the noise on the HV ground away from the anode
- II) to avoid non-linear effects coming from the final 10th dynode

On some bases, the ground of the HV supply and anode output are shorted together with a braid.

Precision: +/- 22% (S), 33pF only +/- 10% (K)

Figure 3.5: The original PMT base inherited from the ARGUS and HERMES experiments.

### 3.2.1 Original Base

The base that came attached to the PMTs were manufactured specifically for use by the ARGUS experiment, which was a relatively (by SeaQuest standards) lower-rate collider experiment that used  $e^+e^-$  annihilation at the *DORIS II* ring at DESY. After their tenure at ARGUS, they were handed down to the HERMES experiment located at the *HERA* polarized electron accelerator at DESY.

Though no actual circuit diagram was documented for the original PMT base, it was dissected and each component was measured. The results can be found in Fig. 3.5, and its voltage division seen in Fig. 3.6. It features a simple string of resistors with capacitors of increasing capacitance along the last six stages. The voltage division can be recognized to be similar to the timing-linearity compromise scheme described in Fig. 3.4. With a total resistance of approximately  $3.95 M\Omega$  and the operational voltage of -1500 V, the expected standing (bleeder) current even when sitting in the dark is expected to be 0.38 mA. With this in mind, we would expect the voltage divider to destabilize when the signal current approaches this value.

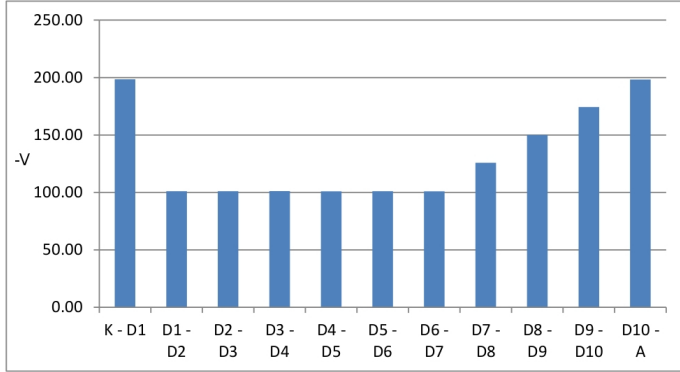


Figure 3.6: The voltage division between subsequent stages for the original PMT base design when supplied with -1500 V.

### 3.2.2 Prototype Base v1

Once the task was set to update the PMT base design, the Fermilab Particle Physics Division was consulted on the matter. In 2010 a base design with similar goals for the exact same PMT model was designed by Sten Hansen [20]. The circuit diagram for the new base can be found in Fig. 3.7.

Here, the resistance was significantly reduced by a factor of about 2.9, allowing for much more bleeder current, without exceeding or closely approaching the on-board resistors' power rating. Also, the voltage division was designed to be relatively "flat" (Fig. 3.8) across stages from D1 to A, which is stated to be recommended for optimal gain. With a total resistance of approximately  $1365\text{ k}\Omega$  and the operational voltage of -1500 V, the expected standing (bleeder) current even when sitting in the dark is expected to be 1.1 mA. Already here, we see that this design parameter alone suggests its ability to withstand  $\sim 3x$  more signal current as compared to the original base.

The introduction of MOSFET transistors is seen between each stage from D7 to D10. Sending the current in parallel over a  $1\text{ M}\Omega$  resistors allows the gate of the transistor to measure the voltage without drawing much current. The Zener dynodes are there in place before each transistor gate to ensure that current only goes one way across the sensitive gate channels.

It is also notable that there are banks of capacitors in parallel across the higher dynode stages. Since there is higher current through this circuit than the original base under the same voltage, there will be a greater demand on the capacitors to resupply the dynode stages with spent charge. The two  $10\text{ nF}$  capacitors in parallel across each stage (which amount to  $20\text{ nF}$  total) is significantly greater than the capacitance across the stages of the original base.

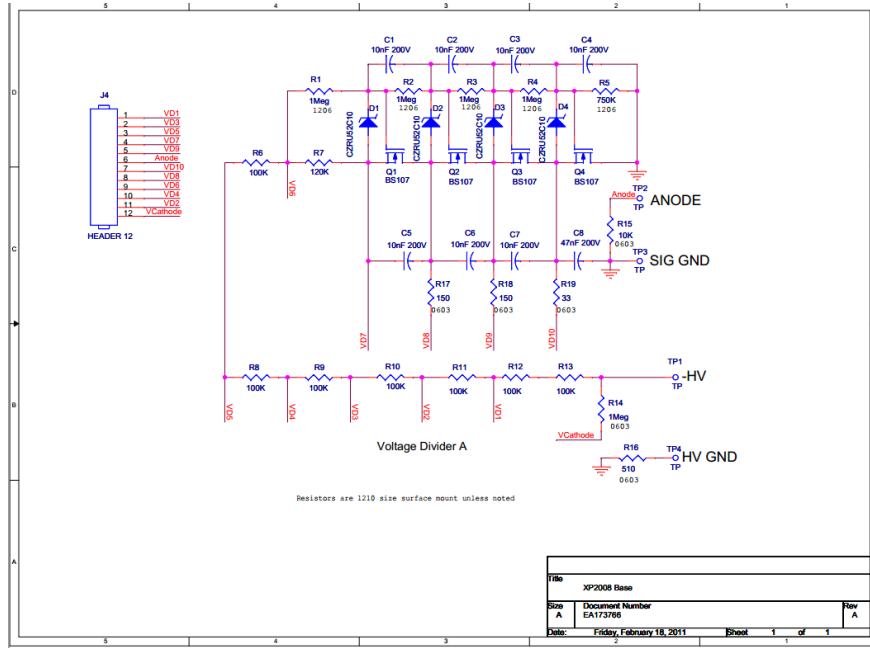


Figure 3.7: The Prototype v1 board circuit diagram received from Fermilab Particle Physics Division [20]. The parts are denoted as R: resistor, C: capacitor, Q: MOSFET transistor, D: Zener diode.

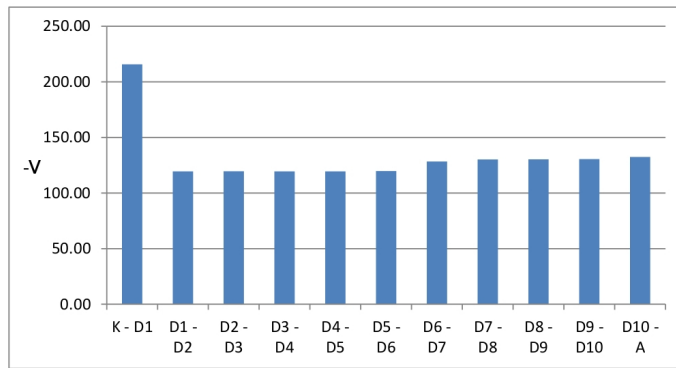


Figure 3.8: The voltage deviation between subsequent stages for the Prototypes v1, v2, and v3 PMT base designs when supplied with -1500 V.

### 3.2.3 Prototype Base v2

The first modification made to the prototype board was to keep everything identical except for the total resistance of the circuit. This was accomplished by halving the resistance of each of the first six stages (R6-R13 on Fig. 3.7) from to increase the bleeder current. The resulting current of the base at -1500 V is at around 2.2 mA. The voltage division retained the same values as described in Fig. 3.8.

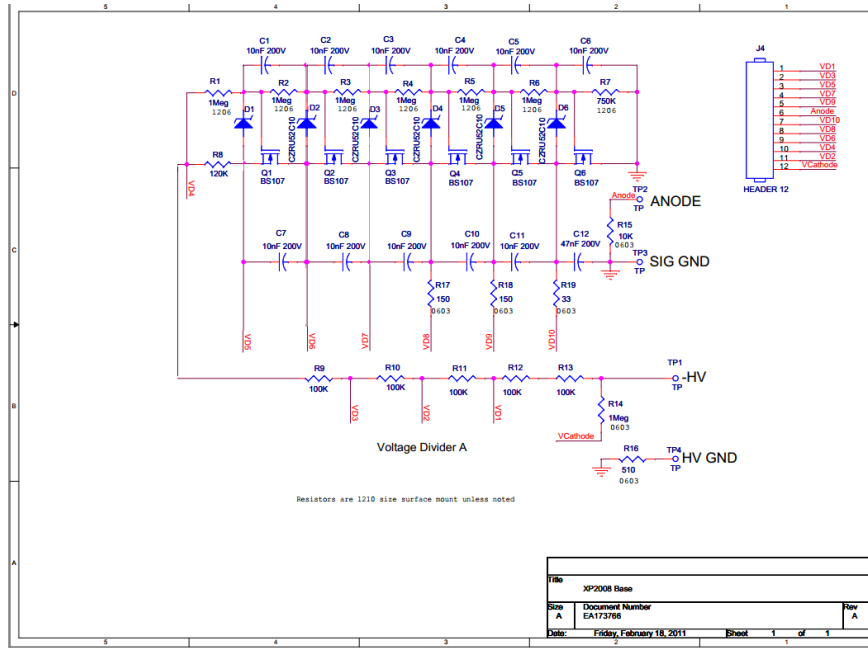


Figure 3.9: The Prototype v3 board: 3 more transistorized stages than the Prototype v1 design.

### 3.2.4 Prototype Base v3

In the case that destabilization was occurring prior to the dynode stages with the added capacitors and transistors, the third prototype was decided to take the Prototype v1 design and add more “transistorized” stages earlier on. This entailed extending the parallel configuration of capacitors, transistor, diode, and  $1 M\Omega$  to the D5-D6 and D6-D7 stages. This prototype configuration can be seen in Fig. 3.9. The voltage division was not significantly altered by this change and remained relatively the same as what is described in Fig. 3.8.

### 3.2.5 Prototype Base v4

The final modification arose from a suggestion from a Fermilab collaborator. It was suggested that it may significantly extend the dynamic range of the tube/base by increasing the voltage drop in, specifically, the

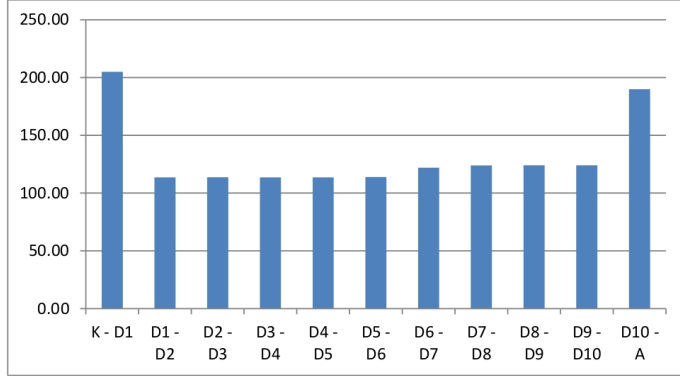


Figure 3.10: The (negative) voltage between subsequent stages for the Prototype v4 PMT base.

last stage relative to the other stages. This reduced to simply replacing R5 (of Fig. 3.7), a  $1\text{ M}\Omega$  resistor, with a  $1.5\text{ M}\Omega$ . All of the rest would remain unchanged from Prototype v1. The premise for this modification was in the case that the final batch of electrons needed help being “swept” to the anode with a higher voltage difference. The change applied resulted in the voltage distribution according to Fig. 3.10.

### 3.3 PMT Base Comparisons

There is a specific difficulty with the objective to increase the rate capability of our PMT’s. This difficulty is that there was not a known instantaneous intensity or target rate capability to attain. The intensity that caused the original PMT performance to sag is unknown, and if it was known, it would be difficult to match the intensity with an experimental setup. As a result, the objective of these tests was to *compare* the performance of the same PMT under controlled conditions using the original and various prototype bases.

Due to the effects of using different PMTs and due to temperature and humidity fluctuations, the PMT behavior can be somewhat variable from test to test. For this reason, one can only reasonably compare results within each base comparison test, and not across different comparison tests. Each was performed on different days, and sometimes with different PMTs.

#### 3.3.1 Testing Apparatus, Measurements, and Procedure

In this experiment, a PMT attached to a PMT base was placed into a light-tight box facing a fast-pulsing 470nm wavelength LED, which provides the driving photonic signal.

## PMT Test Setup

The LED light source assembly consisted of a machined aluminum block that housed the LED, which was a fast-pulsing, narrow beam, water-clear blue LED, peaking in the  $\lambda = 450\text{ nm}$  region. This block had a sliding aluminum insert which had a 1/4" depression used for inserting a 1" diameter NDF of arbitrary optical density [4]. The LED, according to specifications, has a N ns rise time and a N ns fall time, which is important when considering pulsing frequencies on the order of 30 MHz.

The LED itself was driven by an Agilent 33520 Function / Arbitrary Waveform Generator [1] capable of generating signals up to 30MHz. The LED's unadulterated intensity was by far too much light to perform any useful test with such photosensitive hardware. Its intensity was attenuated by use of a neutral density filter (NDF), with a rating  $D = 3.0$ , where the NDF allows 1 in  $10^D$  photons through (1 in 1000 for  $D = 3.0$ ). When testing began, a  $D = 4.0$  NDF was used, but the amount of light reaching the PMT was so small that no decrease in PMT performance for any of the bases was observed all the way up to the highest LED frequencies. As such, the  $D = 3.0$  NDF was chosen for this study.

These were all kept within the light-tight box<sup>1</sup> loaned to the SeaQuest collaboration from the Daya Bay group. This light box was equipped with a patch panel that had both BNC and HVBNC connectors by which to power the PMT base and read out its signal. The light box and all of the installed components can be seen in Fig. 3.11.

A simple data acquisition was assembled from an amplifier, discriminator, and scaler in order to observe that the PMT was functioning properly and firing off at the rate that the LED was set to pulse at.

## Measured and Calculated Quantities

The PMT base was powered by a high voltage supply, and an ammeter was connected between the two in order to measure the amount of current drawn, or bleeder current, from the HV power supply. The PMT signal was processed by an oscilloscope, averaging the pulse over 300 pulses. The primary measurement was measuring the area of the averaged pulse ( $V \cdot s$ ).

We calculated the signal current from the anode as:

$$Q_{pulse} = \frac{\int V dt}{R} \quad (3.1)$$

$$I_{signal} = f Q_{pulse} \quad (3.2)$$

where  $f$  here is the driving frequency of the pulsing LED,  $R$  is the termination resistance of the signal ( $50\Omega$ ),

---

<sup>1</sup>These light-tight boxes are paradoxically referred to as both "light boxes" and "dark boxes", as they're used for testing light-sensitive equipment and they're made to be very *dark* inside.

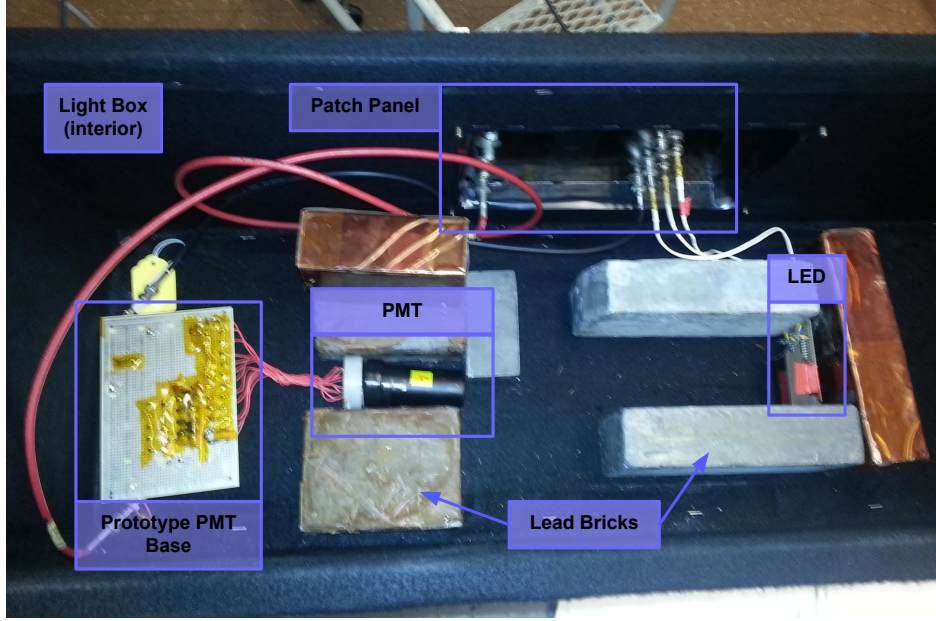


Figure 3.11: Inside of the light box, with the prototype board (left) wired up to a Philips XP-2008 PMT (middle), facing a fast-pulsing LED source (right).

and  $\int V dt$  is the integrated area of the averaged PMT pulse. The amplitude of the pulses was also measured, as it was important in determining if it were feasible to remove the typically noisy hodoscope amplifiers from the SeaQuest stations 1 and 2 DAQ setup.

The measured and calculated quantities of interest are the bleeder current, the averaged signal amplitude, averaged signal area, and signal current over the anode.

Due to the limitations of the instruments used in these tests, there is some systematic uncertainty to consider. The ammeter used to measure the bleeder current between the HV supply and the PMT base used an analog gauge that had closely spaced ticks at 0.2 mA intervals. As such, the systematic uncertainty for the bleeder current is considered to be  $\pm 0.05$  mA. Also, due to pulse-to-pulse variations which cause a mild amount of smearing in the average, the measurement of the amplitudes and signal areas have an uncertainty of  $\pm 5$  mV and  $\pm 0.1$  nVs, respectively. The uncertainty in the signal area translates to an uncertainty in the calculated signal current of around  $\pm 0.04$  mA. These fluctuations are considered negligible with respect to the quantities measured.

### Test Procedure

Most of the prototyping was performed over the span of two weeks. As new suggestions were made at base improvements and the iterations v1-v4 progressed, more comparison tests were performed. The procedure for each test was the same and is as follows:

1. Connect the base to the PMT and to the HVBNC and BNC connectors.
2. Close the lid to the light box.
3. Gradually power the PMT (-250 V every 5 s) until it is as -1500 V.
4. Watch the scaler counter on the DAQ to see if it is rapidly counting. No (or very few) counts on the scaler. means the box is light-tight.
5. Let the PMT and base warm up to near-operational temperatures with its standing current for a minute or two.
6. Power on the function generator and LED, setting the function generator to create a 16 ns square wave pulse to the LED circuit (the minimum achievable pulse width [1]) at a frequency of 10 Hz.
7. For each of several frequencies from 10 Hz to 30 MHz, perform the following:
  - (a) Observe the scaler to ensure that the count is increasing at the same rate as is set by the function generator. This confirms that both the PMT, base, function generator, and LED are generally working as planned.
  - (b) Trigger on the signal from the PMT output.
  - (c) Average the signal over 300 triggered pulses and then freeze the frame.
  - (d) Record the current draw from the HV supply (bleeder current).
  - (e) Measure and record the pulse amplitude with the oscilloscope cursor.
  - (f) Measure the pulse area using the signal integration feature, setting vertical cursors at the zero-intercept on each side of the pulse.
  - (g) Return to triggering mode and increase the function generator frequency as warranted.
8. Power off the function generator and LED circuit.
9. Step the PMT voltage down slowly to 0 V.
10. Open the light box and replace the base for subsequent tests as necessary, repeating the steps above.

### 3.3.2 Original vs. Prototype v1

The first test was to compare the original base with the first iteration of the prototype base. It was generally expected that this new design with more modern technology would exceed the performance of the original base, but the question was twofold: to what extent does it perform better and what is the baseline by which to compare future improvements?

The first important observation is the baseline amplitudes of the signals from the two bases, as seen in Fig. 3.12(a). While the absolute voltage itself is not as useful since the LED doesn't necessarily reflect actual operating conditions, we do see that the amplitude from the new base design is increased by a factor of more than two. This in itself is significant in when considering the limits of the discriminators that were

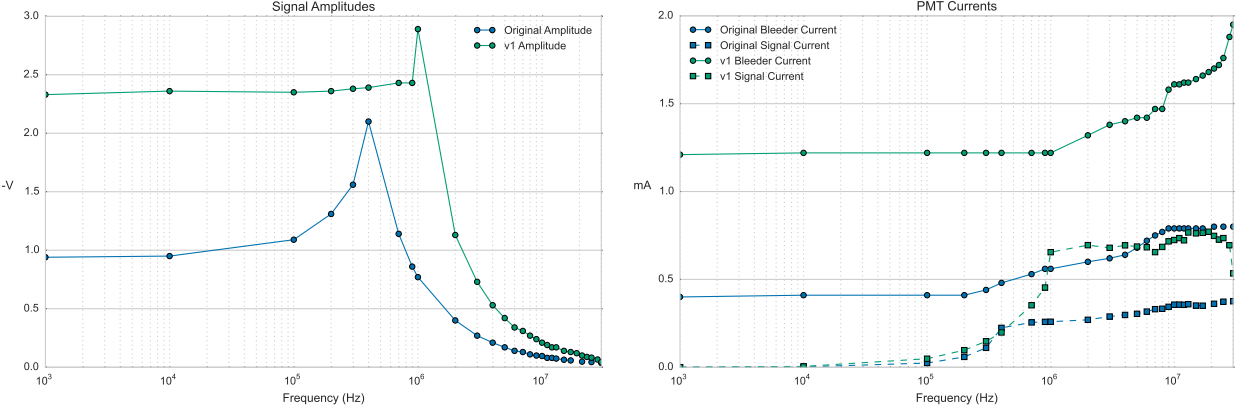


Figure 3.12: Measurements of the (a) signal amplitudes and (b) bleeder and signal currents in the original and prototype v1 PMT bases. The HV was inadvertently set to -1600 V for this test instead of the intended -1500 V.

used in the hodoscope arrays for Stations 1 and 2. With even a modest boost to gain and signal amplitude, the PMT signals should be large enough that an amplifier is not required in order to get a discriminator to trigger on a PMT pulse. Seeing as the amplifiers used had often caused troubles with the amount of electronic noise they tended to imbue, this was an encouraging observation.

Next, we look at the behavior of the amplitudes as the frequency progresses. It is safe to assume that the unchanging behavior in the lower frequencies indicate that the voltage divider is stable and that there is no voltage breakdown yet. At higher frequencies, there is a qualitative peak in amplitude for both bases, followed by a steep decline. This rise and then sharp fall would seem to indicate the end of stable PMT base operation, with the fall indicating the onset of degradation of performance.

To better identify the conditions that cause this onset, we look to currents applicable to both bases (Fig. 3.12(b)). In this particular test, we see the original base peak in amplitude at  $\sim 4$  MHz and prototype base v1 peak at  $\sim 10$  MHz. Looking to the currents, we see that these particular points mark a certain point for both where the signal current reaches almost exactly 50% of the bleeder current. The baseline improvement with this base over the original one was estimated to extend the operational range by a factor of three – the point where the amplitude drops below the low-frequency baseline.

Around the time of these tests, Sten Hansen conducted a SPICE (Simulation Program with Integrated Circuit Emphasis) simulation of the prototype circuit and was able to reproduce what was observed. In particular, it was observed that the gain began to change dramatically when the anode (signal) current reaches a significant fraction of the total current drawn from the HV supply; a current that is much less than 100%. It was concluded that 50% was consistent with his findings.

### 3.3.3 Original vs. Prototype v1 vs. Prototype v2

Several suggestions were made in altering the prototype base in order to maximize this improvement, including lowering the overall resistance of the circuit. If the signal current grows at the same pace, then by increasing the bleeder current, there is a chance that a higher frequency signal will be required to bring the signal current up to the point where the divider breaks down, which we estimated above to be  $\sim 50\%$  of the increased bleeder current.

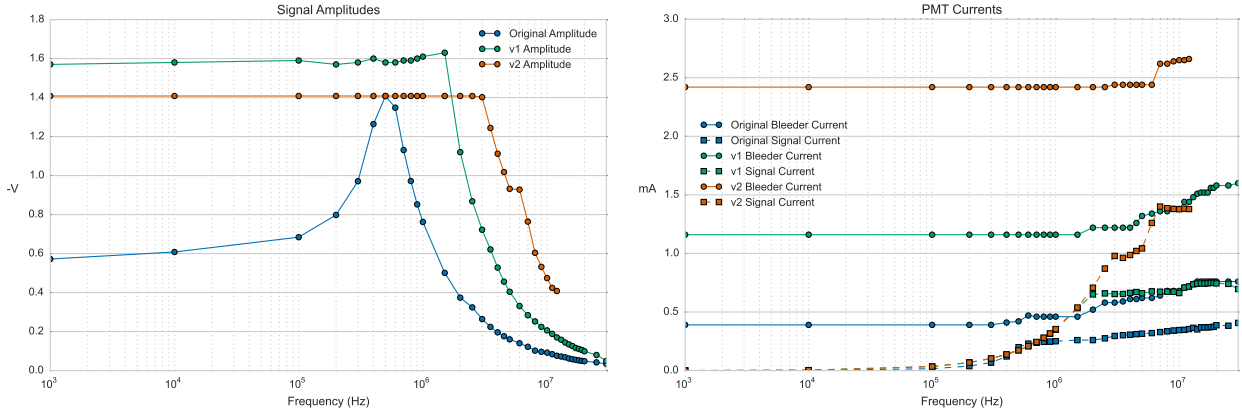


Figure 3.13: Measurements of the (a) signal amplitudes and (b) bleeder and signal currents in the original, prototype v1, and prototype v2 PMT bases.

Looking to Figure 3.13(a), we see that this basic premise is technically sound. The prototype v2 base exceeds the dynamic range of both the original base and the prototype v1 base by factors of approximately a factor of four and two, respectively. This is a significant improvement, and this, at first, seems to be an avenue to pursue. However, an issue arose after increasing the LED frequency from 13 MHz to 14 MHz when a resistor burned out. The test continued with the rest of the bases, but the results paint a clear picture of what happened.

By halving the resistance, the bleeder current doubled (Figure 3.13(b)). This caused the power being dissipated by the resistors to exceed their power rating. The prototype bases were built with 0.25 W resistors, and as the bleeder current rose well above 2.5 mA, one of the resistors failed. This did not bode well for how a smaller on-board resistor might fare with the same current.

To further exacerbate matters, it was found that the LeCroy 1440 HV supplies that were to be used could only supply a maximum of 2.5 mA per channel [24]. Seeing as these power supplies had proven themselves sensitive and prone to communication and performance failures, it was deemed inadvisable to demand anywhere near the maximum current from these HV supplies.

For these reasons, it was decided that the new PMT base design of prototype v1 not be modified in this

manner which might suffer from overheating, component failure, and a too-high current demand.

### 3.3.4 Prototype v1 vs. Prototype v3

Perhaps it was the case that the “transistorized” steps were doing their job well and the destabilization was occurring at prior stages. Since the only downside of adding additional steps was added cost, a base with more transistorized stages was created as depicted in Fig. 3.9.

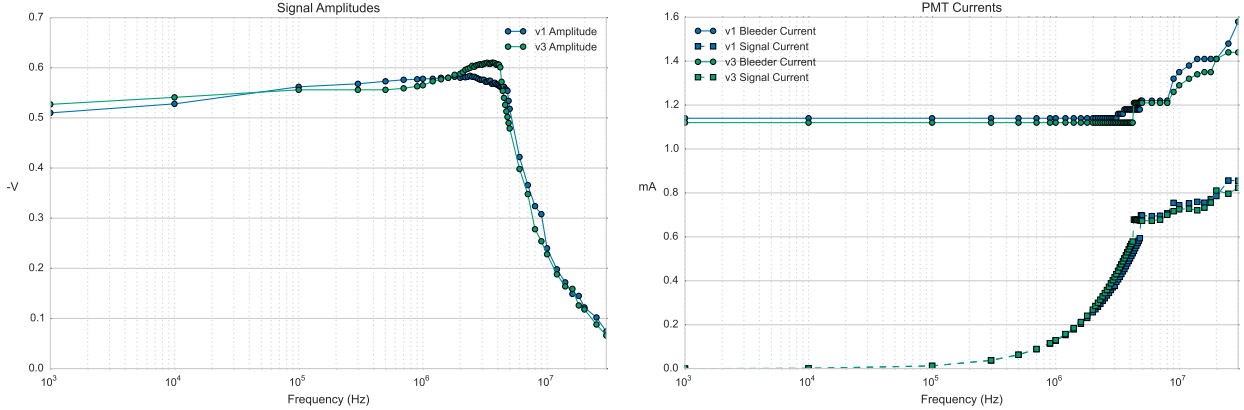


Figure 3.14: Measurements of the (a) signal amplitudes and (b) bleeder and signal currents in the prototype v1 and prototype v3 PMT bases.

As is quite evident in Figure 3.14, there was no significant difference in the performance of the two prototype bases. As such, this modification was not adopted into the final design.

### 3.3.5 Prototype v1 vs. Prototype v4

The final test modification of increasing the resistance and thereby the voltage drop across the final D10-A stage was tested against the prototype v1 base.

This modification turns the voltage divider slightly away from the “optimum gain” configuration and more towards the “optimal timing / linearity compromise” configuration. This is seen to have a direct effect on how a loss in gain can be observed between the v1 and v4 base in Fig. 3.15(a). While the rate capability does seem to slightly increase from 4 MHz to 5 MHz, the value of having a higher gain was deemed more desirable. Higher gain, again, means that the then-used noisy amplifiers would no longer be needed, and the marginal loss in rate capability was considered a reasonable tradeoff.

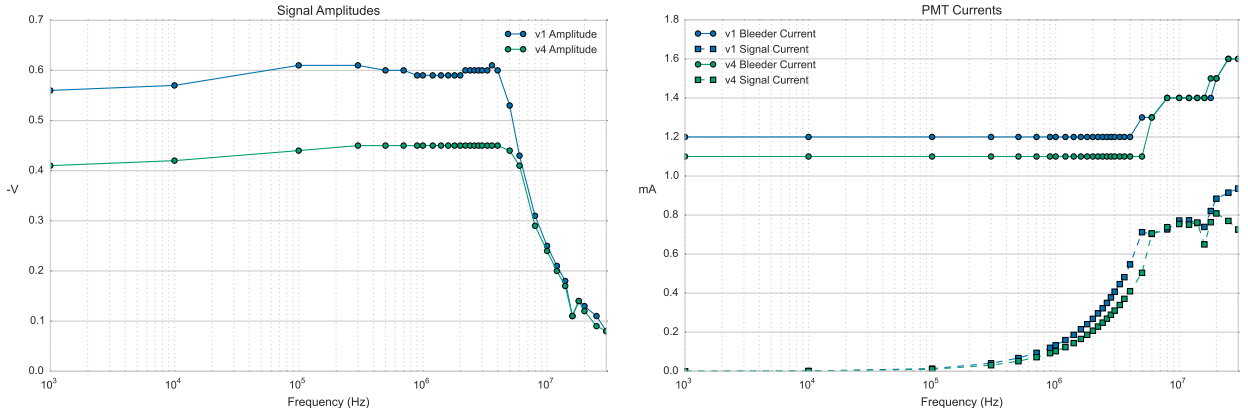


Figure 3.15: Measurements of the (a) signal amplitudes and (b) bleeder and signal currents in the prototype v1 and prototype v4 PMT bases.

### 3.3.6 Base Comparison Conclusions

After these tests were conducted and the information regarding each of the bases' performances was evaluated, it was decided that the prototype v1 base design was the optimal base configuration to move forward with. This base design yielded a clear improvement in both signal amplitude ( $\sim 2x$ ) and rate capability ( $\sim 3x$ ) at the expense of more complex circuitry and an increased supply current draw. It then became the task to fit this circuit onto small printed circuit boards (PCBs), and then manufacture, install, and test them.

## 3.4 Base Manufacturing and Installation

It was decided that the original base structure was well-packaged and well-shielded with its  $\mu$ -metal canister. As such, a two-component board was designed by Sten Hansen that consisted of a 2.5" diameter board and a small rectangular "daughter board". By June of 2013, the mother and daughter boards (attached) had been manufactured and delivered to UIUC for assembly into the rest of the base.

Since the sockets that coupled the board to the PMT pins was not commercially available, they had to be salvaged by deconstructing the original bases. This consisted of cutting the components between the two boards of the original base and then using a solder vacuum to separate the board from the socket pins. The socket and the other structural elements of the PMT base were separates and prepared for construction with the new base PCB (Fig. 3.16).

The deconstruction and re-soldering of the bases took place over the span of about three weeks. Each base was tested to provide the same voltage division across stages and was tested in operation inside the

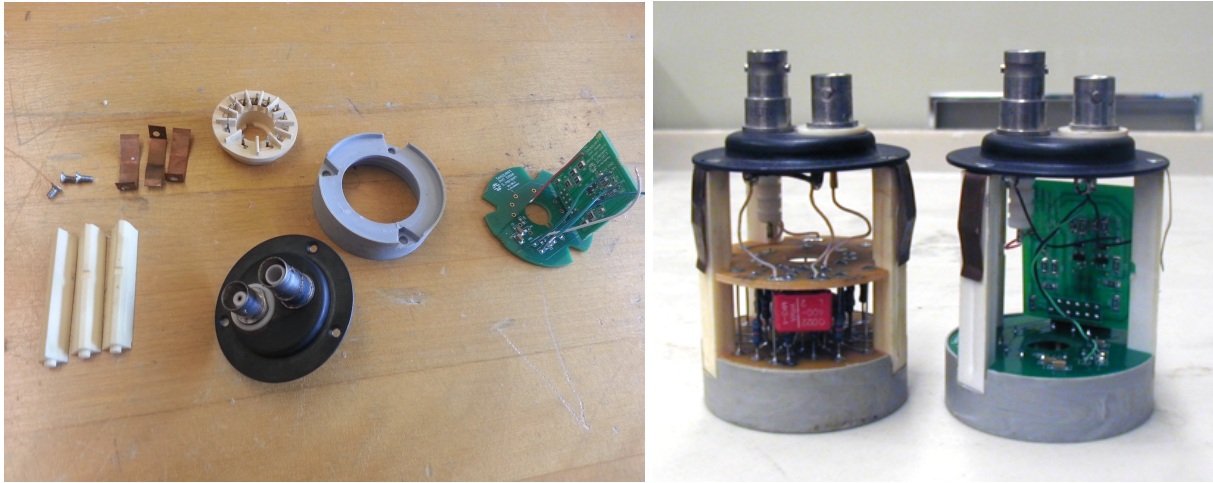


Figure 3.16: (Left) The components of the disassembled original base and the manufactured new base PCB with attached daughter board. (Right) The original and new bases fully assembled, side-by-side.

light box apparatus by observing its signal characteristics and the rate of the scaler counting (which should match up with the LED frequency).

After all bases were constructed and tested, the final task was to find the optimal operating voltage for a PMT assembly that would be suitable for detecting minimum ionizing particles passing through a scintillator paddle similar to the ones used at Stations 1 & 2 at SeaQuest. We also want the minimum possible voltage, as higher voltages correspond to increased noise. This was performed by assembling three stacked scintillator paddles, each with a PMT attached to their light guide. Their outputs were passed through a discriminator and then to a coincidence unit, which in turn had its output sent to a scaler counter. The top and bottom PMTs were powered to -1500 V, and their coincidences were counted on one channel of the scaler counter. Simultaneously, the middle paddle, set to a variable voltage setting, had its coincidences with the top and bottom paddles counted on the other channel of the scaler counter. The ratio of these two counts ( $\epsilon = (\text{triple coincidence}) / (\text{top} - \text{bottom coincidence})$ ) described the efficiency of the middle hodoscope. The voltage of the middle PMT is varied until a plateau in the efficiency is identified and recorded to be the ‘nominal voltage’ of this reference PMT.

All of the constructed PMT bases and the “reference” PMT and base were then sent up from UIUC to FNAL to be installed into Stations 1 & 2 and used for “gain matching”. The gain matching is done by exposing a scintillator paddle to a  $\gamma$ -ray source while connected to a PMT and adjusting its voltage until it produces the same signal amplification, or *gain*, as the rest of the PMTs. The original PMT that the rest are matched to is the reference PMT from the previous efficiency study.

Matching the gain is not a simple task, and the typical approach is to take advantage of a physical

phenomenon called the Compton Effect occurs in scintillator material when a  $\gamma$ -ray scatters off of it. Often times, the  $\gamma$ -ray of energy  $E$  will not deposit the whole of its energy, but only a portion of it. The spectrum of the photons that scatter off will have energy

$$E' = \frac{E}{1 + \frac{(1-\cos\theta)E}{m_e c^2}} \quad (3.3)$$

where  $\theta$  is the angle of deflection and  $m_e$  is the electron mass. This, in turn, deposits transferred energy  $E_T = E - E'$  into the scintillator which has a maximum value of

$$(E_T)_{max} = E \left( 1 - \frac{1}{1 - \frac{2E}{m_e c^2}} \right) \quad (3.4)$$

This energy is known as the Compton Edge, as it is characterized by a very sharp falloff in the energy spectrum of energy deposited by a source of a specific energy. The particular energy of this edge is not important for the purpose of gain matching. Instead, it's used as a qualitatively sharp feature that can be clearly identified when examining the energy spectrum of photons in scintillator material, as seen in Figure 3.17. As such, it can be used as a landmark to use for adjusting the voltages of each PMT in a way such that the gain of each is the same.

Once installed onto a scintillator paddle, the reference PMT was powered to nominal voltage and a radioactive Cs-137 source was pointed at the paddle. Since the PMT signal has some *linearity* to its signal, the amount of energy of incoming photons will translate approximately linearly to the amount of signal out of the PMT. The signal from the PMT (with the Cesium source pointing at the scintillator paddle) is passed through a qVt (charge-voltage-time) module in “Q-mode” to histogram the total integrated charges of the PMT signals. The qVt’s channel location of the Compton edge for this reference PMT at this nominal voltage is recorded. Then, every other PMT is powered and measured through the qVt with the Cesium source, and its voltage is adjusted until the Compton edge falls on the same channel. This procedure is generally known as “gain matching”.

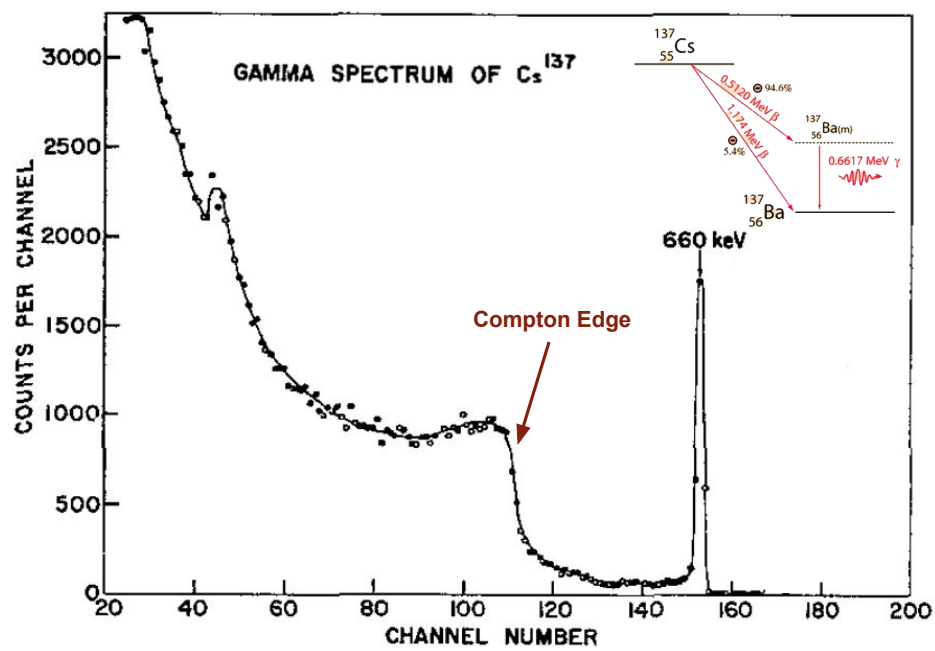


Figure 3.17: The  $\gamma$ -decay energy spectrum of Cs-137 as seen through a scintillator-PMT-qVt setup [35]. Here, the Compton edge can be seen at channel 110.

# Chapter 4

# Data Productions

## *CHAPTER STATUS: IN PROGRESS*

During my tenure at SeaQuest, I was primarily in charge of the effort to decode the raw, serialized data from the data acquisition systems and store it in a manner in which it could be readily accessible by collaborators worldwide. Beyond that, emphasis was placed on curating the tracked physics data and preparing it in such a way that facilitates quick and simple analysis from many different analytical software packages.

The technologies used to perform this were a combination of compiled C/C++ codes, MySQL, ROOT, and the Fermilab Computing Division’s primary computing grid. The end product provided to all collaborators was in the form of unified MySQL database “schemas” (or, groups of tables) possessing all of the combined run, spill, event, slow control, and tracked information, along with specific data quality flags in place to assist in the selection of good analysis data.

## 4.1 Raw Data Processing

The three raw outputs of the data acquisition systems, as described above (and in Chapter 2) are Main DAQ CODA files, Scaler DAQ CODA files, and Beam DAQ ASCII files. Each raw data file corresponds to the data taken from certain subsystems over approximately one to two hours of running time. These three types require varying degrees of de-serialization, parsing, processing, and storage – a process as a whole defined as *decoding*.

All raw data files are backed up to long-term tape storage (managed by FNAL Computing Division), and the decoded and processed data gets stored on one of four MySQL servers to be used for analysis by the collaboration. Data is also output to ROOT files for ease of use by independent tracking programs.

event_length = 4		
event_type = 17	1	0xCC
time		
run number		
run type		

event_length = 4		
event_type = 18	1	0xCC
time		
(reserved)		
number of events in run thus far		

Figure 4.1: (Left) The Prestart event, with event type 17; (Right) The Go event, with event type 18[33].

#### 4.1.1 CODA Event Format

A single CODA file can be described as being a chain of events. These can generally be divided into “CODA Events” for those related to the CODA file itself, and “Standard Physics Events” when containing experimental data read out by CODA and its subsystems. Each event can be represented by an array of unsigned 32-bit integers. When using the CODA EVIO (event input/output), one whole event is read out into such an array, which can vary in size from 6 to  $\sim 50,000$  integers long, depending on the type of content.

CODA Events primarily correspond to the actions taken by a shift-taker using the *regui* application on the data acquisition computer. The types of events that fall under this category are: Sync, Prestart, Go, Pause, and End. It should be noted that the Sync and Pause events do not generally get used at SeaQuest. These provide markers in the CODA file of what commands were given to CODA through the course of taking data.

Before data taking can begin The readout controllers and the trigger supervisor need to be loaded with a designated firmware in order to operate properly. Before a CODA file is started and created, this “Download” is performed, and then CODA is ready to transition from the downloaded state to the prestarted state. The CODA file is then initialized with a prestart event, whose format can be seen in Figure 4.1. The most important information stored in the prestart event is the run number, which is used universally through the experiment.

Once in a prestarted state, a “Go” action is initiated to transition it into data taking mode. This action generates a Go event. If ever paused, a Go event would be created once data taking was resumed. Go events contain the current time and the number of events in the run so far, also seen in Figure 4.1. It should be noted that the “time” stored in these events is not trusted, as the data acquisition computers are not synced to an official external source.

The last CODA Event of importance is the End Event. This contains the number of events in the run, but primarily serves as a marker to any programs reading the CODA file that the EOF (end of file) has been

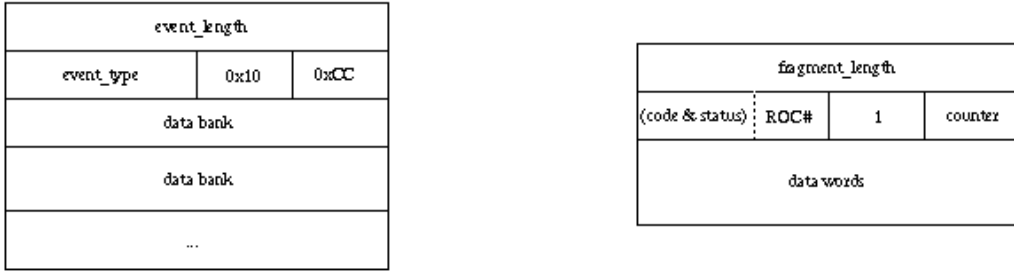


Figure 4.2: (Left) A standard physics event, with various event types, filled with a series of data banks; (Right) The ROC data bank format[33].

reached, and to commence any post-run processes.

Most of the events in the CODA file, however, will be “Standard Physics Events”. The contents of these can be varied, but can be characterized generally as having a header containing the total length of the event (in number of 32-bit integer “data words”), followed by several “data banks”, which are typically filled with a series of ROC outputs (Fig. 4.2). The contents and formats of the ROC data banks are completely controlled by the ROC programming, and whatever set of 32-bit words the ROC has to read out, it will store in its “data words” block.

#### 4.1.2 ROC Data Bank Formats

#### 4.1.3 Decoding Raw Data

The CODA file decoding process is nearly identical in the cases of the Main DAQ and Scaler DAQ outputs, and only differ by content; the Scaler DAQ reads out specific scaler data, and the MainDAQ contains TDC readouts of the detectors. For each one to two hour *Run*, the CODA files can be well-described as the following sequence of events (and the data they contain):

1. Prestart Event (Run data)
  2. Begin Spill Event (Spill data, Scaler readout)
  3. Many Physics Events (Event data, TDC readout)
  4. End Spill Event (Spill data, Scaler readout)
  5. SlowControl Event (Slow control readout, Spill ID readout)
  6. Spill Counter Event (Spill ID readout)
- ...(Repeat 2-6 for each *Spill*)

The decoding programs use C and C++ in conjunction with Jefferson Lab's CODA I/O library[33] to read these events and parse them according to their individual formats. Data from these CODA events are decoded and placed into hierarchical categories.

## Run Level Data

Run-level data contains data and metadata pertaining to the entirety of the run that is recorded. At the time of the Prestart Event, the date and time of the run are stored, along with a readout of the specific settings of all non-trigger TDC boards. Settings regarding which triggers are enabled and what each of their prescale factors is also stored in the run-level data.

After the End Event is encountered, metadata is aggregated and stored regarding such items as the number of chamber hits, the types of triggers that were fired, the target positions used, average magnet currents, and other useful metrics. All of these fields of settings and aggregated values can be used later on to quickly determine if a run is analyzable, or if it has characteristics that are desirable for specific niche analyses.

## Spill Level Data

The *Beginning of Spill* (BOS) and *End of Spill* (EOS) events bookend the set of physics events for a given spill. At each BOS and EOS events, the 140 MHz VME scalers are read out. At the beginning of the spill, all scalers are zeroed out, and then read out again after the spill has ended.

Slow Control events are read out between spills, which contain data regarding the current spill identifier number, target systems, beam and radiation monitors, and environmental readings.

The spill identifier (*spillID*) is what is used to synchronize the data together across various data acquisition systems. As such, the *spillID* is read out redundantly in both Slow Control and Spill Counter events (which contain only the *spillID* value) to ensure that the data is appropriately labeled.

When the End Event (for the whole CODA file) is reached, the independently-recorded Beam DAQ data (recorded in an ASCII file) is read and stored with the rest of the Spill-level data.

## Event Level Data

For each spill,  $\sim 3k$  events are triggered to be recorded, though this number can vary greatly with the particular beam settings of a run. With each event, three types of information is stored: the trigger which fired the event, a measure of the beam intensity per RF bucket, and the full detector readouts. The detector readouts require the most processing of all the rest of the data. The CODA files contain the hardware

addresses of each detector *hit*, along with a *TDC time*. The following steps briefly summarize the processing steps:

1. Mapping: Map the hardware address to a detector name and detector element number
2. Timing: Classify hits as in-time or not and calculate *drift time* from TDC time
3. R-T (time-to-space): Translate *drift time* to *drift distance*
4. After-Pulse Elimination: Remove hits that result from signal reflection and other electronic artefacts
5. Trigger Road Reconstruction: Use *v1495* TDC hits to reconstruct possible trigger roads that may have fired
6. Hodoscope Masking: Remove drift chamber hits that have no adjacent hodoscope hit
7. Trigger Road Masking: Same as hodoscope masking, but only using hodoscopes from reconstructed trigger roads

This fully processed data is then stored into one the experiment’s MySQL databases and/or a ROOT file.

## 4.2 Online and Offline Processing

There are two running modes of raw data processing: on-line and off-line. For on-line mode of productions, all Run- and Spill-level data is decoded, but only 1-in-*n* Physics Events are processed, where *n* is typically between 3 and 15, depending on the event data taking rates. This “*sampling mode*” is used in order for the decoding to reliably keep up with even high-intensity beam data. This data pipeline is important for on-line monitoring of the experiment by shift crews. With this up-to-the-minute stream of data, any abnormalities in duty factor, wire maps, et al. can be observed directly and acted upon quickly.

For off-line, or “batch”, productions, a large group of categorically similar runs is defined, and the chain of production processing is initiated. The steps of this process is generally decoding, tracking, archiving, and merging. The logical blocks of runs are typically defined by “roadset”, or, the version of the set of trigger roads used in the L1 trigger matrix. Differences in these trigger matrices can affect the distributions to a degree commensurate with the difference in the set of roads that are triggered on by the FPGA-1 trigger. As such, each block of data using a given roadset should be analyzed individually and then have its results combined with those of other roadsets via a weighted average.

The decoding and tracking is performed on Fermilab Computing Service’s FermiGrid, which provides the computing resources necessary to process hundreds of runs simultaneously. The tracking has also expanded

its capabilities to run on the Open Science Grid, which is a grid computing network that pools together computational resources from national laboratories and universities throughout the world[11]. This allows the intensive reconstruction algorithms to perform its tracking on thousands of grid nodes at once.

A single decoding job submission will output the processed data to one of the four available MySQL servers and also to a ROOT file. The processed data in ROOT form at this stage is called the “digit” data. Whether or not the decoding sends Hit and TriggerHit information to the MySQL schemas is an option that can be set at the time of batch processing. The current operating mode is to perform batch processing, sending Hit/TriggerHit data to MySQL for only 1-in-50 runs. This allows users to capture a glimpse of full hit distributions for runs within a roadset while preventing a single pass of the experiment’s data from filling up all available data storage space.

After this step, jobs will be submitted to run one or both of the two tracking programs based on the ROOT file and/or the MySQL data. Once the tracking is completed, the ROOT file is archived on the Fermilab BlueArc NAS backup system for storage and for tracking.

Upon the completion of decoding and tracking of a specified range of runs, all of their Run-, Spill-, and Event-level data, along with its tracked data, is combined into a single *merged* schema. These *merged* schemas are mirrored across all four of the MySQL servers for optimal redundancy and availability.

### 4.3 RDBMS Data Structure

The processed data is primarily stored in MySQL Server 5.1 databases. MySQL is an open-source **Relational Database Management System** (RDBMS) developed by Oracle that is well-suited for the storage and responsive querying of hierarchical data.

Each run is decoded into its own schema, and contains its own instances of all tables of a specified design. The tables are all *join*-able to each other by sharing *foreign keys* with each other in the form of the *runID*’s, *spillID*’s, and *eventID*’s. The contents of the tables are *indexed* in such a way that *joins* and queries gain a speed performance boost, but this comes at the cost of disk space.

The data on the server is world-wide accessible and can be queried using the standard querying language. The queried data can be directed to any analysis code in any programming language due to the large array of MySQL API’s available.

#### **4.3.1 Data Schemas**

#### **4.3.2 Schema Table Organization**

#### **4.3.3 Future Technologies**

### **4.4 Data Quality**

*Talk about dataQuality bits, the levels they're used at, and how to use them in selecting data.*

# Chapter 5

## Analysis

*CHAPTER STATUS: PLANNING/OUTLINE*

### 5.1 Reconstruction and Tracking of SeaQuest Dimuons

#### 5.1.1 Hit Reduction

#### 5.1.2 Particle ID

#### 5.1.3 Muon Momentum Reconstruction

#### 5.1.4 Kalman Filter Track Fitting

#### 5.1.5 Vertex Fitting

#### 5.1.6 Monte Carlo Validation

### 5.2 Data Selection

*Talk about roadset characteristics, amount of data*

### 5.3 Analysis Cuts

*Here give summary of all levels of implemented cuts.*

#### 5.3.1 Run Level Cuts

*Give ranges of runs that are excluded. Maybe add a subsection about the manual target position study.*

Bin#	$x_2$ Range
0	(0.08, 0.14]
1	(0.14, 0.16]
2	(0.16, 0.18]
3	(0.18, 0.21]
4	(0.21, 0.25]
5	(0.25, 0.31]
6	(0.31, 0.53]

Table 5.1:  $x_2$  bin ranges

	target	yield
None	104	
Empty	84	
LH2	3138	
LD2	3472	
C	1721	
Fe	1370	
W	1553	

Table 5.2: Raw dimuon yields for Roadset 57

### 5.3.2 Spill Level Cuts

*Dump out Kenichi's data quality slides here, with some plots showing visualizations of good and bad value ranges for some interesting fields.*

### 5.3.3 Event Level Cuts

*FPGA1 cut and maybe nonsense RF+00 cuts? Should be a brief section.*

### 5.3.4 Dimuon Level Cuts

*x1, x2, xF, mass, trackSeparation, etc.*

### 5.3.5 Track Level Cuts

*Talk about target-dump separation along with the rest of the other cuts.*

## 5.4 Dimuon Yields

### 5.4.1 Binning of Data

The  $x_2$  bins for this EMC ratio measurement were chosen such that each bin in  $x_2$  has similar levels of statistics.

Concurrent with this analysis, studies of  $\bar{d}(x_2)/\bar{u}(x_2)$  and parton energy loss are conducted. Due to the nearly identical source of signal across these studies (good Drell-Yan target dimuons), a consistent selection of kinematic binning maintains a certain continuity among analyses. The  $x_2$  binning chosen can be found in Table 5.1

### 5.4.2 Raw Yields

*Summarize the raw, unweighted and uncorrected yields here.*

### 5.4.3 Live Proton Calculation and Integration

*Summarize the reasoning for the live proton value and define its calculation. Finish with the number of live protons per roadset per target, and then the yields per live proton values.*

## 5.5 Dimuon Weights and Corrections

Weighting of events is a standard procedure for mapping one distribution onto another. The most common example is with Monte Carlo (MC) simulation weighting. A simple physics event MC meant to simulate a well-defined process will ‘throw’ an event with certain kinematics randomly drawn from known distributions via *inverse transform sampling*. By doing this, the simulation is already close to being physical, but according to the cross section of a given process, a certain combination of kinematics will be decidedly more or less probable. A weighting subroutine calculates this likelihood for each event and assigns a weight with respect to how likely that event is based on the kinematics thrown. When binning this weighted data, the adjusted number of events in a bin is given by

$$N_{bin} = \sum_{i \in bin} w_i ; \quad \sigma_{bin} = \sqrt{\sum_{i \in bin} w_i^2} \quad (5.1)$$

which reduces to the Poissonian statistical picture when all weights are 1.

Weighting in this manner can be used in any case where it is desirable to map one distribution to another, as in the case of applying corrections in the case of efficiencies and background subtractions. The most intuitive connection between the use of weights and corrections is in the case of efficiency corrections. Let us say that a dimuon with a certain set of kinematics, for whatever combination of effects, has a reconstruction efficiency of 80%. This means that four out of five actual dimuons with these kinematics will be reconstructed. If you know this efficiency  $\epsilon_{recon}$ , you can apply a weight as  $w = 1/\epsilon_{recon}$  to each dimuon, as each dimuon represents, in part, a larger population that is not fully represented. In the case of our example, a single dimuon represents  $1/0.80 = 1.25$  dimuons in order to make up for the ones that are missed due to that specific inefficiency.

At SeaQuest, there is an issue of rate dependence, and as the sources of this effect is identified, we apply a correction for each source in the form of an applied weight. Here, we discuss the reconstruction efficiency

and empty/none target background subtraction corrections.

### 5.5.1 “kEfficiency” Correction Using Messy/Clean Data

It is a matter of combinatorics at SeaQuest that, as the intensity increases, the number of background hits on all of the detectors increases. As the number of hits in all the detectors increases, the harder it becomes for the tracking to identify the actual dimuon(s) from the whole event. This is regarded to be an intensity-dependent tracking efficiency. Seeing as the primary tracking algorithm for SeaQuest is kTracker, this is known as the “kEfficiency”, and its intensity, target, and kinematic dependency makes it a factor to model and correct for.

The procedure developed by Evan McClellan of UIUC for calculating this kEfficiency is to take compare the performance of the tracking on a clean MC sample of dimuons to an analogous sample that’s mixed in with real intensity-dependent background. To do this, a *single* sample of MC-generated dimuons and all of their hits is generated; this sample is denoted as the “*clean*” sample. Then, this sample is mixed with all of the hits from a NIM3 event from the experimental data. The NIM3 trigger, as is discussed in Chapter 2, is the randoms trigger, and by using these events we avoid any effects due to trigger selection bias. This mix of MC dimuons and NIM3 triggered data is denoted as the “*messy*” sample. These NIM3 events all have an intensity, and by embedding a clean MC dimuon into a situation typical of an event at a given intensity, we get a basis by which to judge how efficiently the tracking can reconstruct a dimuon in the clean sample versus the messy sample as a function of intensity (and other kinematic variable).

It is important to note that the DY cross section is so small that there is a negligible chance that a given randomly-triggered NIM3 event will contain an actual dimuon, nonetheless a dimuon matching the characteristics of the MC dimuon that is embedded. As such, it is assumed that the dimuon embedded in the NIM3 event is the only dimuon to find in the event. It is also justified to assume that the kinematics of a dimuon is in no way correlated to the intensity, and the intensity of an event relates only to the amount of background hits observed. The relation to the intensity and the number of background hits can be observed in Figure 5.1.

Once the messy and clean samples are prepared, the tracking software is run on them and the two outputs are compared. The first step is to bin the resulting reconstructed dimuons into intensity bins. This binning uses the weights of the dimuons that is assigned by the GMC that created them. The weights are used instead to avoid undue influence on the efficiency from dimuons that are highly unlikely to occur. The value of the bin and its uncertainty are calculated according to Eq. 5.1.

For each matching bin, the ratio of  $\frac{\#_{messy}}{\#_{clean}}$  values is used to calculate the efficiency of the tracking for

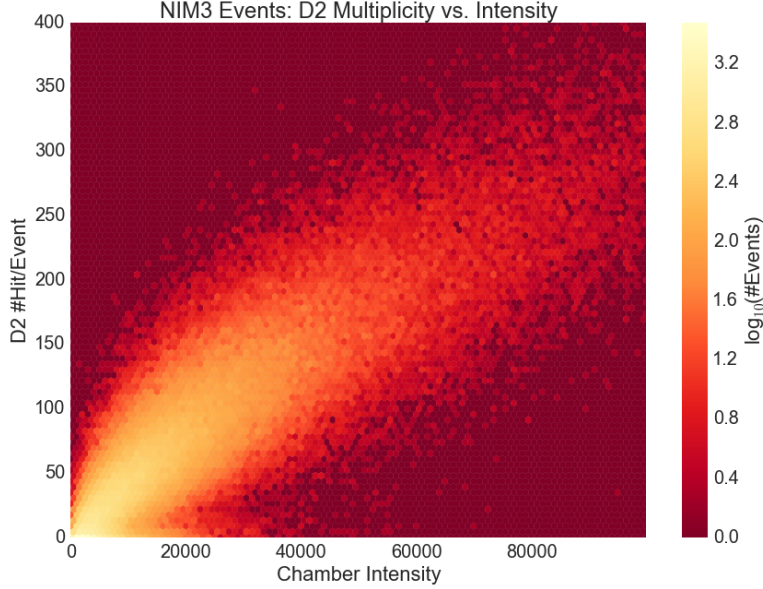


Figure 5.1: The linear tendency of detector multiplicity to increase with intensity is observed by looking to unbiased NIM3 events. Here, the occupancy per event of the drift chambers at station 2 are shown as a function of intensity.

that bin. The uncertainty of that efficiency is more complicated, as the relation between the messy and clean samples is of a *binomial* nature. Each dimuon successfully reconstructed in the messy sample represents a *positive* outcome from the number of possible outcomes which is represented by the clean sample. With this kind of relationship, binomial uncertainty calculations must apply. For large enough  $N$  number of trials and efficiency  $\epsilon \notin \{0, 1\}$ ,

$$\epsilon = \frac{N_+}{N} ; \quad \delta\epsilon = \sqrt{\frac{N_+ N_-}{N^3}} = \sqrt{\frac{\epsilon(1-\epsilon)}{N}} \quad (5.2)$$

but when weighted trials are involved, things become more complicated in calculating the statistical error. The calculation of this statistical error[25] is as follows:

$$\epsilon = \frac{\sum_{i \in +} w_i}{\sum_i w_i} \quad (5.3)$$

$$\delta\epsilon = \frac{\sqrt{\sum_{i \in +} w_i^2 \left(\sum_{i \in -} w_i\right)^2 + \sum_{i \in -} w_i^2 \left(\sum_{i \in +} w_i\right)^2}}{\left(\sum_i w_i\right)^2} \quad (5.4)$$

where

$$\sum_{i \in -} w_i = \sum_{i \in +} w_i - \sum_{i \in +} w_i \quad (5.5)$$

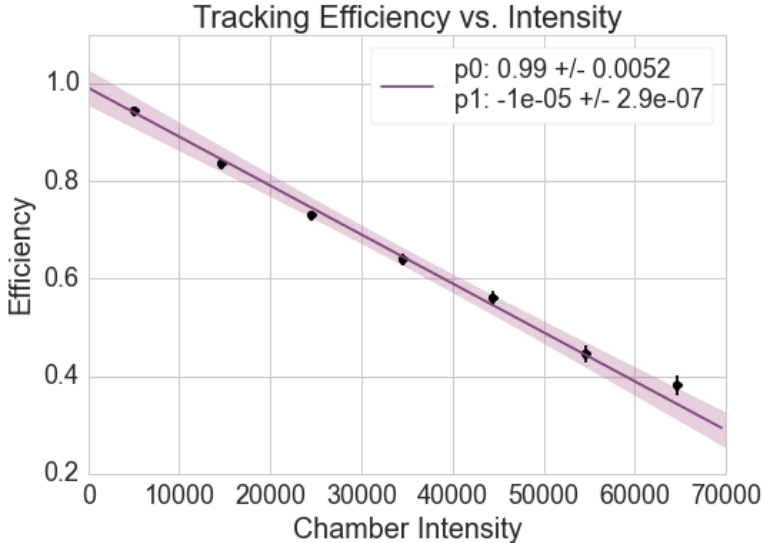


Figure 5.2: The ratio of “messy” to “clean” dimuon samples from the Deuterium target in Roadset 67 data. This shows the linear relationship of the tracking efficiency to the intensity of the events. The shaded band indicates the 95% confidence band of the fit.

$$\sum_{i \in -} w_i^2 = \sum_{i \in +} w_i^2 - \sum_{i \in +} w_i^2 \quad (5.6)$$

For a set of efficiencies, a linear function is fit to the efficiencies. This fit function would then be used to calculate the efficiency for any given dimuon that occurs at any given intensity. The linear parameters are fitted to the data (which is weighted by its statistical uncertainties) by a  $\chi^2$ -minimization procedure to render a line of best fit along with a confidence interval (Fig. 5.2)

Further, these fits have a statistically significant kinematic dependence, so it becomes important to unfold the kinematic space and perform this procedure for several kinematic bins in one or more dimensions to assure an accurate efficiency calculation. Of the six defining kinematics of the dimuon, we examine the dependence of the fit on five of them:  $(x_1, x_2, p_T, \theta, \phi)$ , neglecting the azimuthal production angle  $\phi_{\gamma^*}$ . Each of these five kinematics is divided into three bins (low, medium, high) values to observe on which kinematics the linear fit depends. The results are shown in Figure 5.3. The curves produced seem to indicate that there only exists a kinematic dependence on the  $x_1$  and  $x_2$  kinematics. If this is the case, then the clean and messy samples can be split two-dimensionally in these two kinematics, and a fit can be made to both variables. When analyzing dimuons, its kinematics can indicate which fit to use to calculate the tracking efficiency based on the intensity of the event, and a weight can be calculated.

But before we come to any clear conclusions, let us investigate two more kinematic phase spaces. We know from the discussion in Chapter 1 that  $\{x_1, x_2\}$  can be used almost interchangeably with  $\{x_F, M_{\gamma^*}\}$ ,

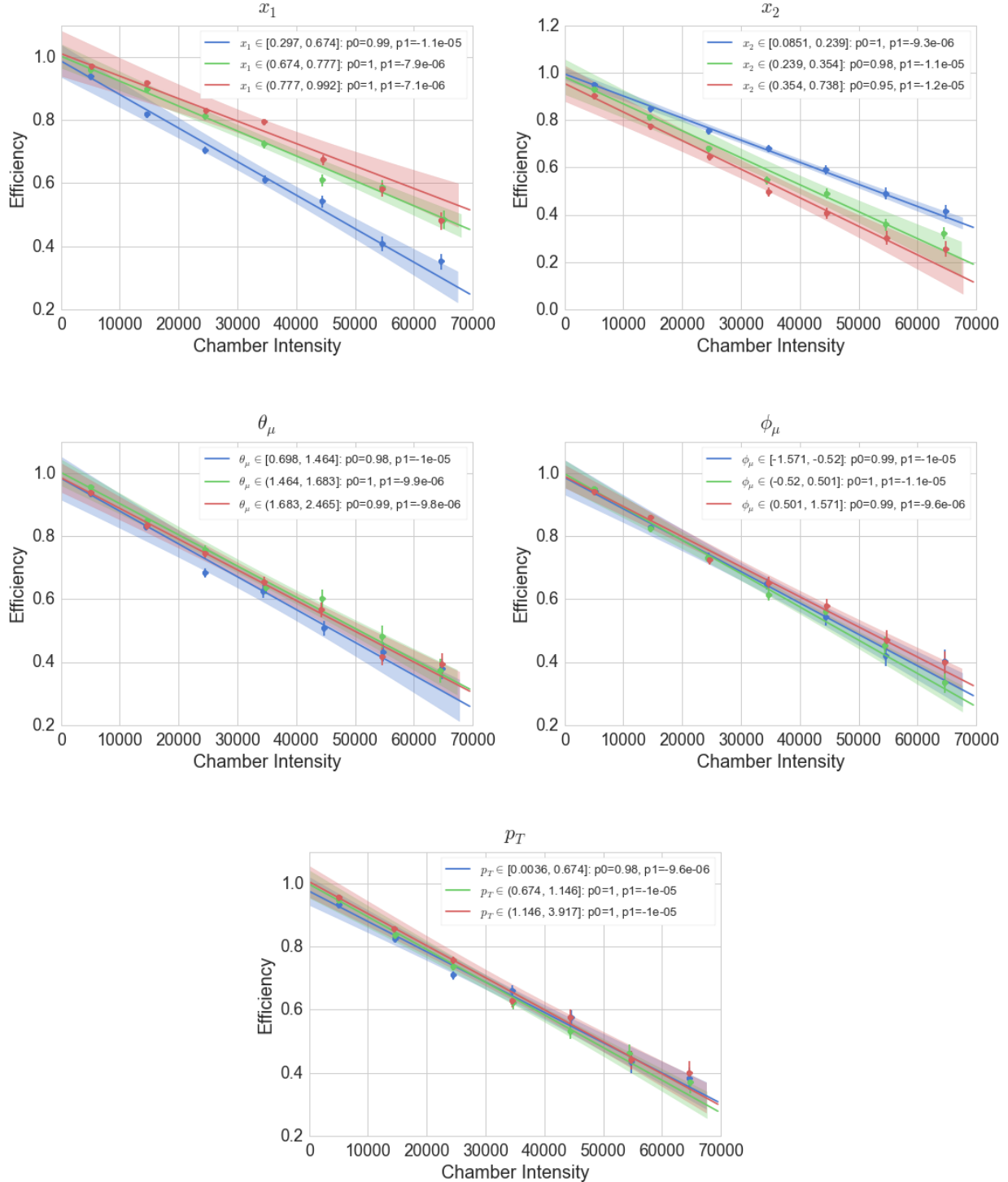


Figure 5.3: Tracking efficiency with the data broken into three statistically equivalent bins in the five primary kinematics,  $(x_1, x_2, \theta_\mu, \phi_\mu, p_T)$ . There appears to be a significant kinematic dependence on  $x_1$  and  $x_2$ .

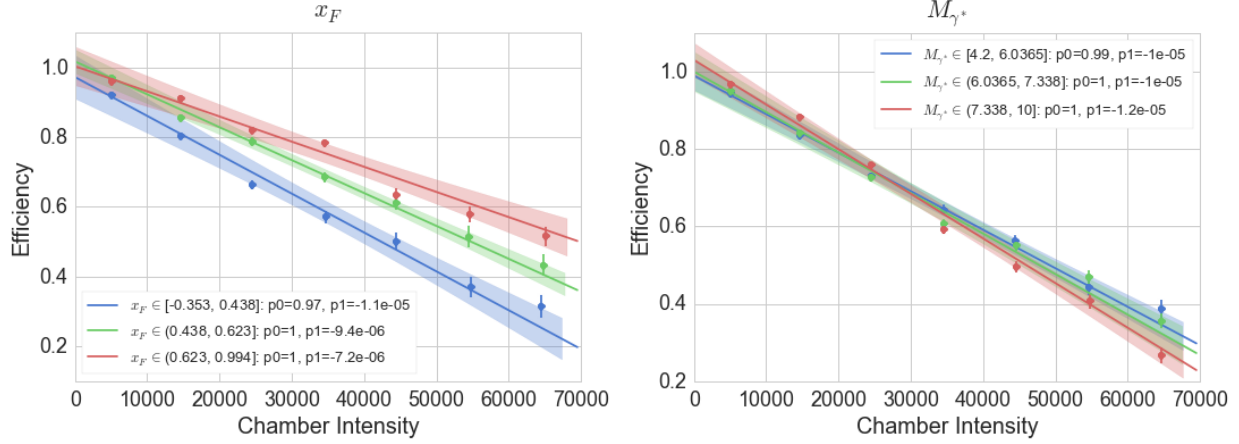


Figure 5.4: The kinematics  $x_F$  and  $M_{\gamma^*}$  are investigated. A clear kinematic dependence exists in  $x_F$  while  $M_{\gamma^*}$  is largely consistent.

and each of  $x_1$  and  $x_2$  depend on both  $x_F$  and  $M_{\gamma^*}$ . As such, if only one and not the other shows to influence the tracking efficiency curves, then only that one would be needed for the tracking efficiency correction. We see the behavior of the efficiency curves as a function of  $x_F$  and  $M_{\gamma^*}$  in Figure 5.4. It can be concluded that since there is no substantial mass dependence observed, the tracking efficiency has a kinematic dependence solely on  $x_F$ .

Another consideration is with respect to whether or not there is a target dependence to factor into the correction. For all of the above “kEfficiency” plots, only deuterium data is used. The kEfficiency curves for deuterium, hydrogen, carbon, iron, and tungsten can be found on Figure 5.5. It can be concluded that there is enough of a difference between deuterium, iron, and the rest to justify calculating and applying this correction on a target-by-target basis.

Also, as a sanity check, there should be no time-dependence of this function. A quick check comparing different sets of data from two different roadsets quickly confirm that there is no such time dependence (Fig. 5.5).

As a result, the final calculation of an tracking efficiency for a given dimuon event should depend on (1) target, (2)  $x_F$ , and (3) intensity. In order to apply this as a weight, we first define  $kEff_{t,\bar{x}}(I)$ , a set of linear fit functions: one for each target ( $t$ ) and for each kinematic bin ( $\bar{x}$ ), which may be binned in any number of kinematic dimensions. In the case of this analysis, the kinematic binning will only be in  $x_F$ . The procedure in weighting each dimuon will then be to take each dimuon event  $i$  and its chamber intensity  $I_i$ , originating from target  $t_i$  in  $x_F$  bin  $x_{F_i}$ , create a weight as

$$w_i = \frac{1}{kEff_{t_i,x_{F_i}}(I_i)} \quad (5.7)$$

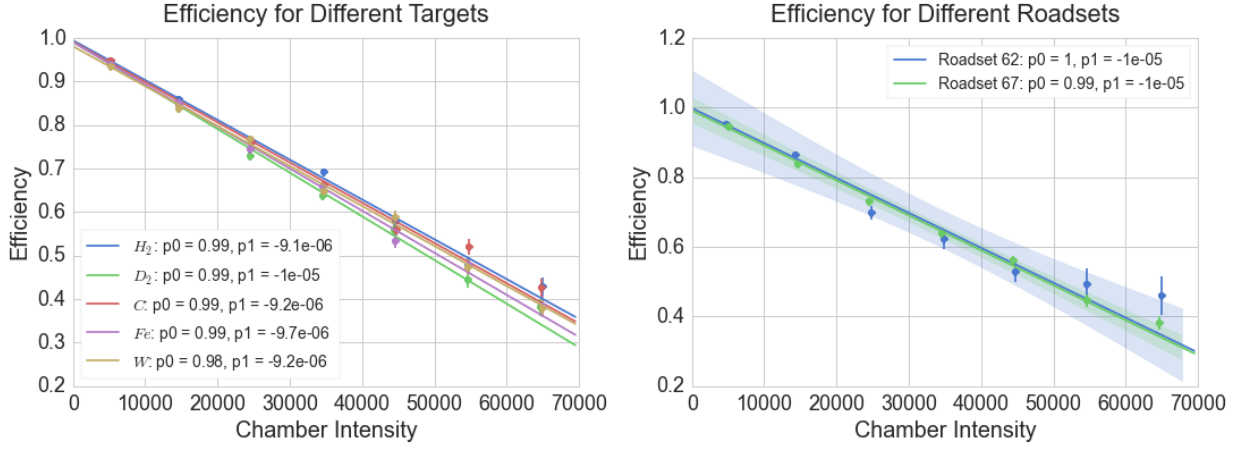


Figure 5.5: Comparing the tracking efficiency curves across (left) the five targets and (right) two temporally different subsets (different roadsets) of data. Confidence bands removed from the target plot for the sake of clarity.

### 5.5.2 The Naive Empty/None Correction

First a few values must be defined. An overall efficiency based on ‘contributions’ from the Empty/None background can be defined as

$$\epsilon_b = 1 - \frac{Y_b/p_b}{Y_t/p_t} = 1 - \left( \frac{p_t}{p_b} \right) \left( \frac{Y_b}{Y_t} \right) \quad (5.8)$$

where  $Y$  is the dimuon *yield* from a given target and  $p$  is the integrated “live proton” count for the same given target. Here,  $b \in \{\text{Empty, None}\}$  and  $t \in \{H, D, C, Fe, W\}$ . It is yet to be conclusively decided by the collaboration whether or not the Empty and None targets are to be combined for these calculations.

The next step is to adjust the yields with the  $kEff_{t,\bar{x}}(I)$ :

$$Y_a \rightarrow Y'_a = \sum_{i:i_t=a} \frac{1}{kEff_{t_i,x_i}(I_i)} \quad (5.9)$$

The yield efficiency when factoring in background then becomes

$$\epsilon'_b = 1 - \left( \frac{p_t}{p_b} \right) \left( \frac{Y'_b}{Y'_t} \right) \quad (5.10)$$

### 5.5.3 The Empty/None vs. Intensity Curve

### 5.5.4 Improved Background Correction

With the Empty/None vs. Intensity Curve  $C(I)$ , we can apply a more sophisticated correction. With  $C(I)$ , we can make an expression for the background contribution to the yields of a given target:

$$p_t \left( \frac{Y'_b}{p_b} \right) = \sum_{i:i_t=t} \frac{D \cdot C(I_i)}{kEff_{t_i,x_i}(I_i)} \quad (5.11)$$

where D is a normalization constant defined in such a way that  $D \cdot C(I)$  is the % chance that a given dimuon from a target actually came from the Empty/None background. D can be calculated as

$$D = \frac{1}{F} Y'_b \left( \frac{p_t}{p_b} \right) \quad (5.12)$$

$$F = \sum_{i:i_t=t} \frac{C(I_i)}{kEff_{t_i,x_i}(I_i)} \quad (5.13)$$

The new intensity-dependent efficiency can now be defined as

$$(\epsilon'_b)_i = 1 - D \cdot C(I_i) \quad (5.14)$$

## 5.6 Combinatorial Background Correction

*Discuss analysis investigating results for the like-sign reconstruction to estimate the combinatorial background. Hopefully it will be intensity-dependent.*

## 5.7 $ld_2$ Contamination Correction

*Discuss contamination backstory, composition breakdown, the fluctuation from bottle-to-bottle, the correction procedure, and the proposed systematic uncertainty in that procedure.*

## 5.8 Isoscalar Corrections for $^{183}W$ and $^{56}Fe$

*Give brief correction in approximating  $n==p$  conversion. Be sure to show results for both iso-corrected and not!*

# Chapter 6

## Results

*CHAPTER STATUS: NOT STARTED*

### 6.1 Dimuon Yield Ratios

*Give EMC ratios, maybe parton energy loss ratios. If there's time, maybe quarkonia ratios. Show for separate roadsets and with/without corrections. Show heavy-to-heavy ratios, too.*

# Chapter 7

## Discussion

*CHAPTER STATUS: NOT STARTED*

# Chapter 8

# Conclusions

*CHAPTER STATUS: NOT STARTED*

We conclude that Bryan Dannowitz likes coffee.

## **Appendix A**

### **Topic A**

## **Appendix B**

### **Topic B**

# References

- [1] Agilent. Agilent 33500 series 30 mhz function / arbitrary waveform generator users guide. <http://cp.literature.agilent.com/litweb/pdf/33520-90001.pdf>. Accessed: 2016-02-03.
- [2] A. Alavi-Harati, T. Alexopoulos, M. Arenton, K. Arisaka, S. Averitte, R. F. Barbosa, A. R. Barker, M. Barrio, L. Bellantoni, A. Bellavance, J. Belz, D. R. Bergman, E. Blucher, G. J. Bock, C. Bown, S. Bright, E. Cheu, S. Childress, R. Coleman, M. D. Corcoran, G. Corti, B. Cox, A. R. Erwin, R. Ford, A. Glazov, A. Golossanov, G. Graham, J. Graham, E. Halkiadakis, J. Hamm, K. Hanagaki, Y. B. Hsiung, V. Jejer, D. A. Jensen, R. Kessler, H. G. E. Kobrak, J. LaDue, A. Lath, A. Ledovskoy, P. L. McBride, P. Mikelsongs, E. Monnier, T. Nakaya, K. S. Nelson, H. Nguyen, V. O'Dell, M. Pang, R. Pordes, V. Prasad, X. R. Qi, B. Quinn, E. J. Ramberg, R. E. Ray, A. Roodman, S. Schnetzer, K. Senyo, P. Shanahan, P. S. Shawhan, J. Shields, W. Slater, N. Solomey, S. V. Somalwar, R. L. Stone, E. C. Swallow, S. A. Taegar, R. J. Tesarek, G. B. Thomson, P. A. Toale, A. Tripathi, R. Tschirhart, S. E. Turner, Y. W. Wah, J. Wang, H. B. White, J. Whitmore, B. Winstein, R. Winston, T. Yamanaka, and E. D. Zimmerman. Measurements of direct CP violation, CPT symmetry, and other parameters in the neutral kaon system. *Phys. Rev. D*, 67:012005, Jan 2003.
- [3] D.M. Alde, H.W. Baer, T.A. Carey, G.T. Garvey, A. Klein, et al. Nuclear dependence of dimuon production at 800-GeV. FNAL-772 experiment. *Phys.Rev.Lett.*, 64:2479–2482, 1990.
- [4] E Ames, C Seshagiri, M Griswold, V Simaitis, J La Due, F Cogswell, S Errede, J Thaler, D Errede, RW Downing, et al. Measurement of 20 hamamatsu r-5900 photomultiplier tubes for atlas tilecal module-0. Technical report, CERN-ATL-TILECAL-98-156, 1998.
- [5] J.J. Aubert et al. The ratio of the nucleon structure functions  $F^2_n$  for iron and deuterium. *Phys.Lett.*, B123:275, 1983.
- [6] D. P. Barber, U. Becker, H. Benda, A. Boehm, J. G. Branson, J. Bron, D. Buikman, J. Burger, C. C. Chang, H. S. Chen, M. Chen, C. P. Cheng, Y. S. Chu, R. Clare, P. Duinker, G. Y. Fang, H. Fesefeldt, D. Fong, M. Fukushima, J. C. Guo, A. Hariri, G. Herten, M. C. Ho, H. K. Hsu, T. T. Hsu, R. W. Kadel, W. Krenz, J. Li, Q. Z. Li, M. Lu, D. Luckey, D. A. Ma, C. M. Ma, G. G. G. Massaro, T. Matsuda, H. Newman, J. Paradiso, F. P. Poschmann, J. P. Revol, M. Rohde, H. Rykaczewski, K. Sinram, H. W. Tang, L. G. Tang, Samuel C. C. Ting, K. L. Tung, F. Vannucci, X. R. Wang, P. S. Wei, M. White, G. H. Wu, T. W. Wu, J. P. Xi, P. C. Yang, X. H. Yu, N. L. Zhang, and R. Y. Zhu. Discovery of three-jet events and a test of quantum chromodynamics at petra. *Phys. Rev. Lett.*, 43:830–833, Sep 1979.
- [7] V. E. Barnes, P. L. Connolly, D. J. Crennell, B. B. Culwick, W. C. Delaney, W. B. Fowler, P. E. Hagerty, E. L. Hart, N. Horwitz, P. V. Hough, J. E. Jensen, J. K. Kopp, K. W. Lai, J. Leitner, J. L. Lloyd, G. W. London, T. W. Morris, Y. Oren, R. B. Palmer, A. G. Prodell, D. Radojičić, D. C. Rahm, C. R. Richardson, N. P. Samios, J. R. Sanford, R. P. Shutt, J. R. Smith, D. L. Stonehill, R. C. Strand, A. M. Thorndike, M. S. Webster, W. J. Willis, and S. S. Yamamoto. Observation of a Hyperon with Strangeness Minus Three. *Physical Review Letters*, 12:204–206, February 1964.
- [8] Siegfried Bethke. Experimental tests of asymptotic freedom. *Prog. Part. Nucl. Phys.*, 58:351–386, 2007.
- [9] CAEN. v1495 general purpose vme board. <http://www.caen.it/csite/CaenProd.jsp?idmod=484&parent=11>. Accessed: 2016-01-26.

- [10] John C. Collins and Davison E. Soper. Angular distribution of dileptons in high-energy hadron collisions. *Phys. Rev. D*, 16:2219–2225, Oct 1977.
- [11] Open Science Grid Consortium. Osg blueprint. <http://osg-docdb.opensciencegrid.org/cgi-bin/RetrieveFile?docid=18&extension=pdf>. Accessed: 2016-02-24.
- [12] S. D. Drell and Tung-Mow Yan. Massive Lepton Pair Production in Hadron-Hadron Collisions at High-Energies. *Phys. Rev. Lett.*, 25:316–320, 1970. [Erratum-ibid.25:902,1970].
- [13] Sidney D. Drell and Tung-Mow Yan. Massive lepton-pair production in hadron-hadron collisions at high energies. *Phys. Rev. Lett.*, 25:316–320, Aug 1970.
- [14] Sayipjamal Dulat, Tie-Jiun Hou, Jun Gao, Marco Guzzi, Joey Huston, Pavel Nadolsky, Jon Pumplin, Carl Schmidt, Daniel Stump, and C. P. Yuan. New parton distribution functions from a global analysis of quantum chromodynamics. *Phys. Rev.*, D93(3):033006, 2016.
- [15] I. Estermann, R. Frisch, and O. Stern. Magnetic Moment of the Proton. *Nature*, 132:169–170, jul 1933.
- [16] H. Eugene Fisk and Frank Sciulli. CHARGED CURRENT NEUTRINO INTERACTIONS. *Ann. Rev. Nucl. Part. Sci.*, 32:499–573, 1982.
- [17] Donald F. Geesaman, K. Saito, and Anthony William Thomas. The nuclear EMC effect. *Ann.Rev.Nucl.Part.Sci.*, 45:337–390, 1995.
- [18] David J. Gross and Chris H. Llewellyn Smith. High-energy neutrino - nucleon scattering, current algebra and partons. *Nucl. Phys.*, B14:337–347, 1969.
- [19] F. Halzen and Alan D. Martin. *QUARKS AND LEPTONS: AN INTRODUCTORY COURSE IN MODERN PARTICLE PHYSICS*. Wiley, 1984. New York, USA ( 1984) 396p.
- [20] Sten Hansen. private communication, 2012.
- [21] E. A. et al. Hawker. Measurement of the light antiquark flavor asymmetry in the nucleon sea. *Phys. Rev. Lett.*, 80:3715–3718, Apr 1998.
- [22] C. R. Kerns. A High Rate Phototube Base. *IEEE Trans. Nucl. Sci.*, 24:353–355, 1977.
- [23] Vardan Khachatryan et al. Measurement of the inclusive 3-jet production differential cross section in protonproton collisions at 7 TeV and determination of the strong coupling constant in the TeV range. *Eur. Phys. J.*, C75(5):186, 2015.
- [24] LeCroy. Lecroy 1440 high voltage power supply manual. [http://ikpe1101.ikp.kfa-juelich.de/manuals/LeCroy\\_1440/operation\\_manual/operation\\_manual.htm](http://ikpe1101.ikp.kfa-juelich.de/manuals/LeCroy_1440/operation_manual/operation_manual.htm). Accessed: 2016-02-03.
- [25] Benno List. Statistical error of efficiency determination from weighted events. Accessed: 2016-03-16.
- [26] G. Moreno, C. N. Brown, W. E. Cooper, D. Finley, Y. B. Hsiung, A. M. Jonckheere, H. Jostlein, D. M. Kaplan, L. M. Lederman, Y. Hemmi, K. Imai, K. Miyake, T. Nakamura, N. Sasao, N. Tamura, T. Yoshida, A. Maki, Y. Sakai, R. Gray, K. B. Luk, J. P. Rutherford, P. B. Straub, R. W. Williams, K. K. Young, M. R. Adams, H. Glass, and D. Jaffe. Dimuon production in proton-copper collisions at  $\sqrt{s} = 38.8$  gev. *Phys. Rev. D*, 43(9):2815–2835, May 1991.
- [27] MVME. Mvme5500 series vmebus single-board computer. <http://www.mvme.com/manuals/MVME5500e-SPEC.pdf>. Accessed: 2016-01-26.
- [28] Brews Ohare. Mosfet structure. [https://commons.wikimedia.org/wiki/File:MOSFET\\_Structure.png](https://commons.wikimedia.org/wiki/File:MOSFET_Structure.png), March 2012. Accessed: 2016-02-01.
- [29] HCZ Photonics. Xp2072: High energy resolution , 10-stage, 39mm (1.5") tube. <http://hzcphotronics.com/products/XP2072.PDF>. Accessed: 2016-01-29.

- [30] C. Quigg. ELEMENTARY PARTICLES AND FORCES. *Sci. Am.*, 252N4:64–75, 1985.
- [31] J. Seely et al. New measurements of the EMC effect in very light nuclei. *Phys. Rev. Lett.*, 103:202301, 2009.
- [32] Shiuan-Hal Shiu, Jinyuan Wu, Randall Evan McClellan, Ting-Hua Chang, Wen-Chen Chang, Yen-Chu Chen, Ron Gilman, Kenichi Nakano, Jen-Chieh Peng, and Su-Yin Wang. FPGA-based trigger system for the Fermilab SeaQuest experiment. *Nucl. Instrum. Meth.*, A802:82–88, 2015.
- [33] Jefferson National Accelerator Laboratory Data Acquisition Support. Coda (cebaf online data acquisition). <https://coda.jlab.org/drupal/>. Accessed: 2016-02-12.
- [34] R. S. Towell et al. Improved measurement of the anti-d/anti-u asymmetry in the nucleon sea. *Phys. Rev.*, D64:052002, 2001.
- [35] P.P. Webb and R.L. Williams. Gamma ray spectroscopy using a germanium lithium-drifted diode. *Nucl. Instr. Methods*, Vol: 22, Apr 1963.
- [36] T. Zimmerman and J. Hoff. The design of a charge integrating, modified floating point ADC chip. *IEEE J. Solid State Circuits*, 39:895–905, 2004.